Photoemission study of the rare earth intermetallic compounds: RNi_2Ge_2 (R = Eu, Gd)

by

Jongik Park

A dissertation submitted to the graduate faculty

in partial fulfillment of the requirements for the degree of

DOCTOR OF PHILOSOPHY

Major: Condensed Matter Physics

Program of Study Committee:
David W. Lynch, Co-major Professor
Joseph Shinar, Co-major Professor
David C. Johnston
R. William McCallum
John G. Lajoie

Iowa State University

Ames, Iowa

2004

Graduate College
Iowa State University

This is to certify that the doctoral dissertation of

Jongik Park

has met the dissertation requirements of Iowa State University

David W Lynch
Co-major Professor

Co-major Professor

For the Major Program

TABLE OF CONTENTS

IS-T 1936

CHAPTER 1. INTRODUCTION

$EuNi_2Ge_2$ and $GdNi_2Ge_2$ are two members of the RT_2X_2 (R = rare earth, T = transition metal and X = Si, Ge) family of intermetallic compounds, which has been studied since the early 1980s. These ternary rare-earth intermetallic compounds with the tetragonal $ThCr_2Si_2$ structure are known for their wide variety of magnetic properties. Extensive studies of the RT_2X_2 series can be found in Refs [1, 2, 3]. The magnetic properties of the rare-earth nickel germanides RNi_2Ge_2 were recently studied in more detail [4].

Their long-range magnetic order can be explained by the indirect Ruderman-Kittel-Kasuya-Yosida (RKKY) exchange interaction between the magnetic rare-earth ions through the conduction electrons [5, 6]. Magnetic measurements have revealed that the Eu ion in $EuNi_2Ge_2$ has an ${}^8S_{7/2}$ ground state with an effective magnetic moment $\mu_{eff} \sim 7.7\ \mu_B$, indicating that Eu is divalent with the $4f^7$ electron configuration in the ground state. $EuNi_2Ge_2$ is antiferromagnetic (AF) below the Néel temperature (T_N) of 30.8 K [4]. Europium ions are usually found to be either divalent or trivalent in metallic compounds, as in insulators, or in a mixed-valence state in some compounds. Especially the application of pressure to $EuNi_2Ge_2$ indicates an almost complete valence change from divalent (0 GPa) to trivalent (10 GPa) at room temperature via a complex mixed-valent region around 5 GPa. The pressure- and temperature-induced valence transitions of the Eu ion in $EuNi_2Ge_2$ were studied by ^{151}Eu-Mössbauer spectroscopy, X-ray absorption, and electrical resistivity [7, 8, 9]. The temperature-dependent magnetic susceptibility of $GdNi_2Ge_2$ [10] shows its effective magnetic moment $\mu_{eff} \sim 8.0\ \mu_B$, close to the theoretical value of 7.9 μ_B for the Gd^{3+} free ion, having the same stable $4f^7$ ($^8S_{7/2}$) ground state as Eu in $EuNi_2Ge_2$, with a transition to an AF state at a T_N of 27.1 K [4]. From Mössbauer spectra [10] the easy axis of magnetization is at an angle of 44°, and close to 75°, from the c-axis for $EuNi_2Ge_2$ and $GdNi_2Ge_2$ polycrystalline samples, respectively, below T_N. Both materials have second transition temperatures below T_N. In $EuNi_2Ge_2$ a second transition (T_t) occurs at a temperature of 13.4 K and T_t is 16.8 K in $GdNi_2Ge_2$. It is suggested for both single crystals that the ordered magnetic moments below T_N are in the basal plane (a-b plane), and in the case of $GdNi_2Ge_2$, between T_t and T_N there is an ordered component of the moment along the c axis from temperature dependent magnetic susceptibility measurements [11].

The AF Néel transition is reported to be driven by strong Fermi-surface nesting from the x-ray resonant exchange scattering (XRES) technique [11]. These nestings in $EuNi_2Ge_2$ and $GdNi_2Ge_2$ are responsible for the modulations of magnetic moments of $\mathbf{q}_{\mathrm{nest}} = (0,0, q_z)$ with $q_z = 1$ and 0.79 respectively. A generalized susceptibility calculation using the tight-binding linear-muffin-tin-orbital (TB-LMTO) method [12, 13, 14] with the atomic-sphere approximation (ASA) with the von Barth-Hedin exchange correlation-potential [15] showed that Fermi-surface nesting is responsible for the magnetic and electronic structure. In the calculation, the Eu $4f$ and Gd $4f$ unfilled shells were treated as core electrons, since the $4f$ shells in rare earth metals are spatially deeply buried, although they energetically lie in the valence band, and are assumed to be treated as localized electrons. $EuNi_2Ge_2$ is isostructural to $GdNi_2Ge_2$, in which Gd has a valence of 3+ with one more conduction electron than Eu in $EuNi_2Ge_2$. Therefore those compounds, which give the same Hund's rule ground state ($^8S_{7/2}$), are suitable systems for the quantitative study of band filling effects on the electronic structure. This is due to the fact that the band structure and total density of states (DOS) in

$EuNi_2Ge_2$ and $GdNi_2G_2$ are so similar qualitatively and the Fermi energy (E_F) of $GdNi_2Ge_2$ is higher due to increased band filling [11], which suggests that a rigid-band model is adequate as a first-order approximation in the electronic structure.

The purpose of this dissertation is to investigate the electronic structure (both valence band and shallow core levels) of single crystals of $EuNi_2Ge_2$ and $GdNi_2Ge_2$ and to check the assumptions that the *f* electrons are non-interacting and, consequently, the rigid-band model for these crystals would work [11], using synchrotron radiation because, to the best of our knowledge, no photoemission measurements on those have been reported. Photoemission spectroscopy has been widely used to study the detailed electronic structure of metals and alloys, and especially angle-resolved photoemission spectroscopy (ARPES) has proven to be a powerful technique for investigating Fermi surfaces (FSs) of single-crystal compounds.

First, resonance photoemission spectroscopy (RPES) will be used to distinguish the particular resonant features, and the partial spectral weight (PSW) distributions of Eu 4*f* and Ni 3*d* electrons will be determined from electron distribution curves (EDCs) on and off resonance for Eu 4*f* and Ni 3*d* levels in $EuNi_2Ge_2$ and $GdNi_2Ge_2$. Therefore we will determine the shape and features of the PSW of Ni 3*d* from the Ni $3p \rightarrow 3d$ RPES measurements and compare them to calculated Ni 3*d* partial density of states (PDOS) for both materials. Resonance measurements of the Eu and Gd $4d \rightarrow 4f$ excitations in $EuNi_2Ge_2$ and $GdNi_2Ge_2$ respectively will be done to reveal where Eu 4*f* and Gd 4*f* states are localized below E_F. We will study a well-known resonant enhancement of the Ni 3*d* satellite in $EuNi_2Ge_2$ and find where it appear in the valence band. Constant-final-state (CFS) partial yield spectra will be taken to determine the valence of Eu and Gd ions in $EuNi_2Ge_2$ and $GdNi_2Ge_2$ respectively at ambient pressure. Constant-initial-state (CIS) spectra for several initial-state energies throughout the valence band will also be taken to investigate the contribution of electron states possessing Ni 3*d* character to the valence band of $EuNi_2Ge_2$.

Second, the electronic band structure of $EuNi_2Ge_2$ and $GdNi_2Ge_2$ along the Γ–Z [001] direction in the bulk Brillouin zone (BZ) will be determined by taking normal-emission photoelectron spectra of the valence band for increasing photon energies, from 14 eV to 44 eV (to 54 eV in the case of $EuNi_2Ge_2$) using synchrotron radiation and compare the experimental results to the theoretical ones. Especially the inner potentials, V_0 for $EuNi_2Ge_2$ and $GdNi_2Ge_2$ can be determined by adjusting the Γ and Z symmetry points of the BZ with the observed band dispersions. In the following, we will study quantitatively the effects of band filling on the electronic structures by observing a rigid-band shift of E_F corresponding simply to an increase of one electron (1e/formula unit) upon going from $EuNi_2Ge_2$ to $GdNi_2Ge_2$.

Lastly, we will examine the Fermi surfaces (FSs) of both materials in the ΓXPZ plane of the BZ. Segments of the FSs will be mapped by obtaining angle-resolved photoelectron spectra in the ΓXPZ plane of single-crystal $EuNi_2Ge_2$ and $GdNi_2Ge_2$, which are in good agreement with band calculations. Specifically we will study how this FS segment changes when one electron (1e/formula unit) is added to $EuNi_2Ge_2$, corresponding to $GdNi_2Ge_2$, based on the rigid-band approximation. We will also take a high-resolution scan of the Fermi edge of $EuNi_2Ge_2$ in an attempt to find evidence of the spin density wave [16] (SDW - referring to the periodic modulation of the spin density with period, $\lambda_0 = \pi/k_F$ determined by the Fermi wave vector k_F) as well. That is due to the fact that SDW gaps remove a portion of the paramagnetic FS. Therefore in transforming from the paramagnetic to the AF, new energy band gaps occur around E_F.

CHAPTER 2. PHOTOEMISSION SPECTROSCOPY

The three-step model of photoemission

The photoelectric effect was first observed by Hertz in 1887. It is well known that the photoelectric effect was first correctly interpreted by Einstein as a quantum phenomenon for light [17]. The basis of the technique is that a photon of classical electromagnetic frequency ν carries an energy $h\nu$. If a sample is placed in vacuum and irradiated with monochromatic photons of sufficient energy to excite electrons into unbound states, photons are absorbed by electrons, thereby resulting in the emission of photoejected electrons (photoelectrons) into vacuum, carrying information about the state they came from (or about the state left behind). This information can be extracted by investigating the properties of the outgoing electron such as kinetic energy distribution, angle of emission, and polarization.

As shown in Fig. 2.1 the measured kinetic energy of the photoelectron is expressed relative to a reference level, the Fermi energy (E_F) from the following fundamental equation (conservation of energy):

$$E_{kin} = h\nu - E_{B,Fermi} - \Phi, \tag{2.1}$$

where E_{kin} is the kinetic energy of the photoejected electron, $E_{B,Fermi}$ is the binding energy of an electron, referred to E_F, of the electron which is ejected, and Φ is the work function of the sample, the energy needed to surmount the potential barrier at the surface.

It's apparent that photoelectrons can be produced only if $h\nu \geq (E_{B,Fermi} + \Phi)$. If the empty level is above the vacuum level, the electron will be ejected with kinetic energy equal to the photon energy minus the work function minus the binding energy.

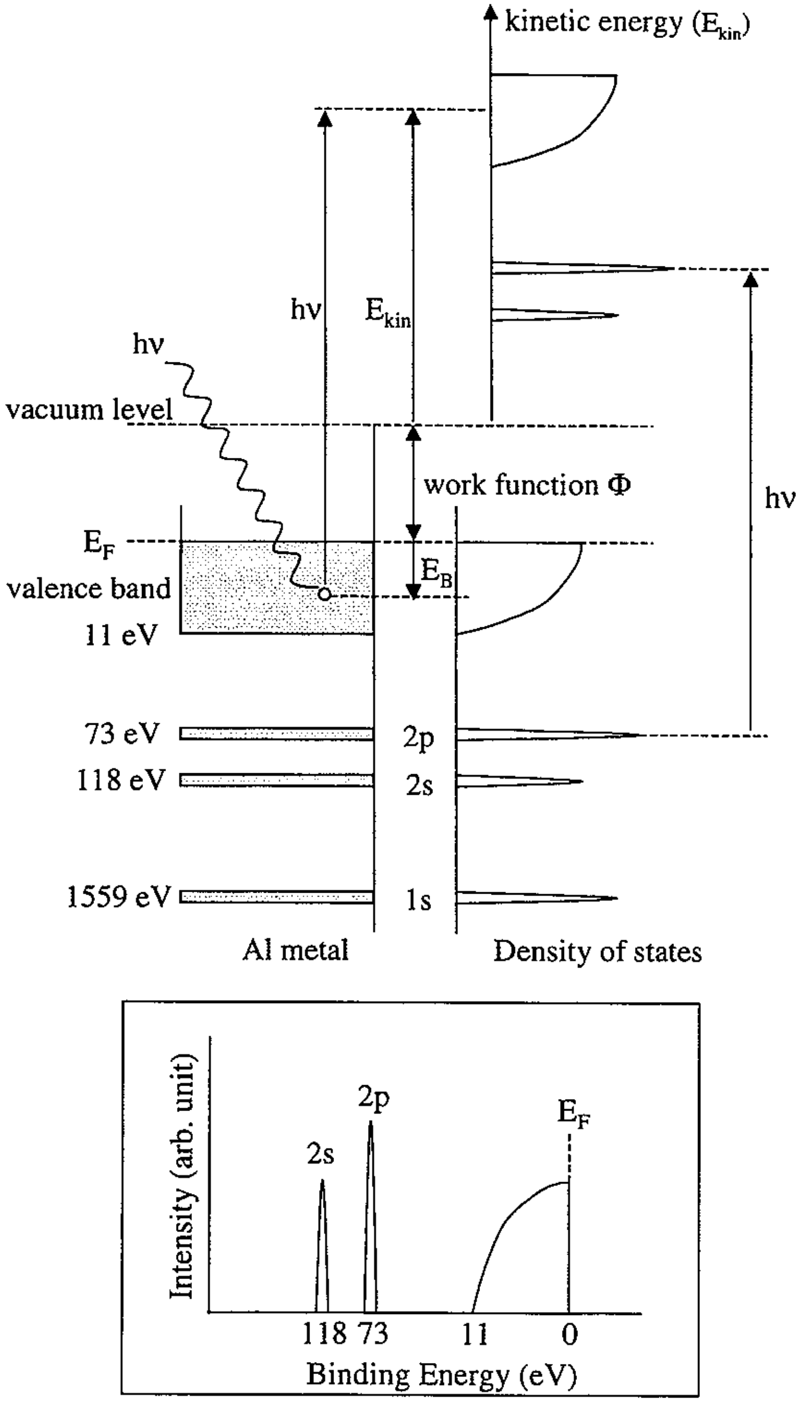

FIG. 2.1 Relationship between the energy levels and the photoemission spectrum produced by photons of energy $h\nu$. The electronic structure of Al is shown as an example. A measured EDC of Al metal is also shown in the lower diagram.

A plot of the intensity of photoelectrons as a function of kinetic energy is called an energy distribution curve (EDC). The highest electron kinetic energy electrons correspond to electrons emitted from near E_F, showing a large step in the EDC whilst the lower electron kinetic energy electrons correspond to electrons emitted from deeper energy levels in the solid. One can then measure the binding energy by knowing the work function, or alternatively, in a metal, one can simply measure the energy of a peak relative to the highest occupied level, E_F. Consequently, since the energy $h\nu$ of the exciting photons is kept fixed, the binding energy E_B of the electronic states relative to E_F can be determined by measuring the kinetic energy E_{kin} distribution of the photoelectrons. Therefore, the energy distribution of photoelectrons corresponds approximately to the energy distribution of electronic states in the solid. Figure 2.1 also illustrates the fact that the electronic density of states of a solid is reflected in the photoemission spectrum. In addition, photoemission spectroscopy is the only method allowing the determination of absolute binding energies of electrons in solids.

The underlying assumption of Eq. (2-1) is that when an electron is removed from an N-electron system, the remaining N-1 electron system is in its ground state - both the energies and wavefunctions - without relaxing (frozen-orbital approximation). As a result, the photoelectron will have a distribution of energies the same as that of Koopmans' theorem [18]. Accordingly, the Koopman energies are very close to the negative Hartree-Fock eigenvalues in the independent-electron picture in which electron-electron correlations among electrons of opposite spin are neglected. Koopmans' binding energy – energy needed to extract the orbital electron to infinity so long as there is no readjustment of the other electrons - does correspond to the energy averaged over all possible final electronic states, including the ground and various excited states, according to the sudden approximation [19].

This is particularly true if the initial single-electron state is spatially extended, but the photoelectron will give rise to more than one final state or an electron in a given state may go into an excited state (shake-up satellite) during photoexcitation, since the photoemission spectra reflect the final states rather than the initial state. It means that the photoemitted electron energy can change due to the response of the system, which may be in the form of relaxation or screening. In terms of energy eigenstates, the shake-up satellite corresponds to an excited state of the remaining *N*-1 electron system. Putting it another way, final state processes such as plasmon excitation (excitation of a collective oscillation in the conduction band), electron excitation, and electron correlation complicate the simple interpretation of the photoelectron results further. Nevertheless, one-electron eigenvalues are useful as a first-order approximation to observed electron binding energies, providing an adequate ground-state description although it may not give the correct picture of the photoemission spectrum.

The three-step model [20] is the one most commonly used in the interpretation of photoemission data qualitatively. Photoemission theories are discussed for example in the books of Hüfner [21], and Lynch and Olson [22], and the review article of Plummer and Eberhardt [23]. The three-step model divides the photoemission process into three sequential processes of (1) the optical excitation of the electron by an incident photon, (2) the transport of the photoexcited electron through the solid to the surface of a sample, and (3) the escape of the electron from the surface into the vacuum. A schematic diagram illustrating the three-step model for the photoemission process is shown in Fig. 2.2 [24]. In Fig. 2.2, a hypothetical photoexcited electron distribution changes as the electrons approach the surface, and again upon escaping into the vacuum, as indicated. According to this model, the spectral intensity is expressed by

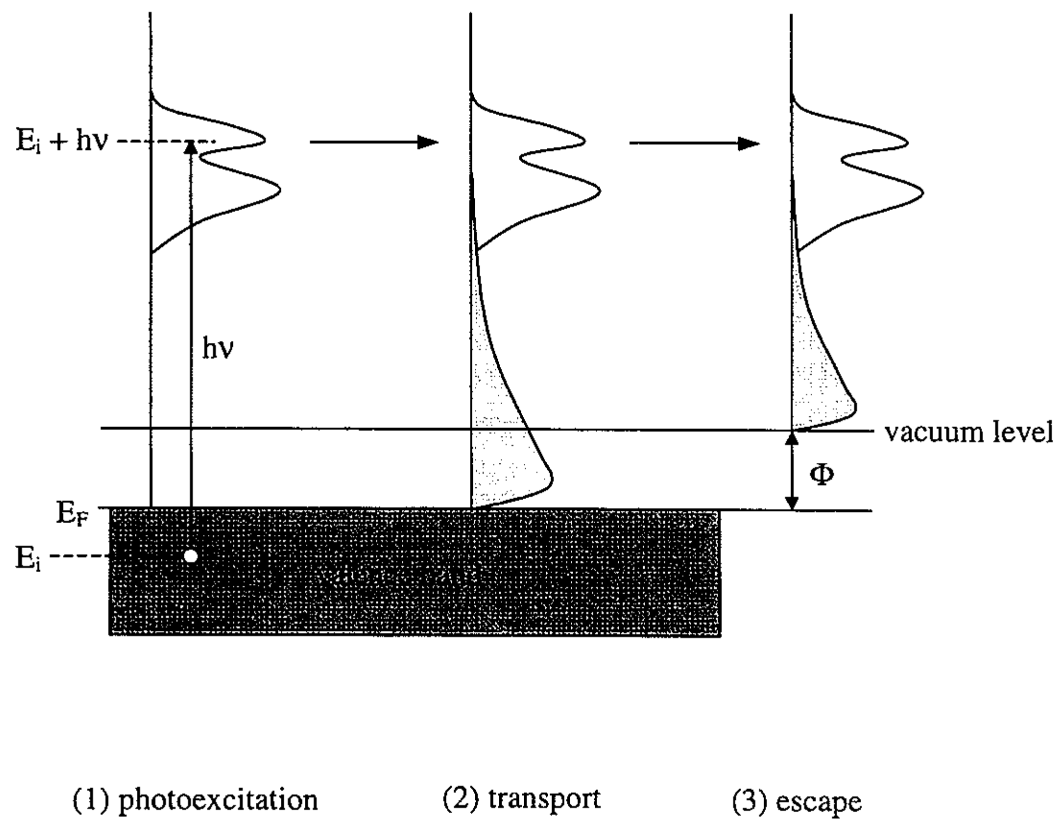

FIG. 2.2 A schematic diagram illustrating the three-step model for the photoemission process (after [20]).

$$I(E, h\nu) = P(E, h\nu) \bullet T(E) \bullet D(E), \tag{2.2}$$

where $P(E, h\nu)$ is the excitation probability, $T(E)$ is a transport function, and $D(E)$ is an escape function.

In the first step, the photoexcitation results from the interaction of electrons with the photon. The Hamiltonian H of an electron (charge $-e$) in the presence of an electromagnetic field is described in terms of the vector potential **A** of the incident light (collinear with the electric vector) and the scalar potential ϕ

$$H = (\mathbf{p} + e\mathbf{A}/c)^2/(2m) + V(\mathbf{r}) - e\phi, \tag{2.3}$$

where **p** is the momentum operator of the electron.

By choosing the gauge such that the scalar potential is zero, Eq. (2.3) becomes

$$H = p^2/2m + V(\mathbf{r}) + e(\mathbf{p}\bullet\mathbf{A} + \mathbf{A}\bullet\mathbf{p})/2mc + e^2A^2/2mc^2 . \tag{2.4}$$

By ignoring A^2 in the linear optical regime and if we use the commutation relation $[\mathbf{p}, \mathbf{A}] = -i\hbar\nabla\bullet\mathbf{A}$, we have

$$H = p^2/2m + V(\mathbf{r}) + e\mathbf{A}\bullet\mathbf{p}/mc + e[\mathbf{p}, \mathbf{A}]/2mc \tag{2.5}$$

$$= p^2/2m + V(\mathbf{r}) + e\mathbf{A}\bullet\mathbf{p}/mc - ie\hbar\nabla\bullet\mathbf{A}/(2mc). \tag{2.6}$$

If we neglect the local field and surface effects, we can choose the Coulomb gauge

$$\nabla\bullet\mathbf{A} = 0 \tag{2.7}$$

so that **p** commutes with **A**.

Finally, Eq. (2.6) can be simplified

$$H = p^2/2m + V(\mathbf{r}) + e\mathbf{A}\bullet\mathbf{p}/mc. \tag{2.8}$$

Therefore, the solid in its ground state may be described by a Hamiltonian H and the incident photon will introduce a small perturbation

$$H' = e(\mathbf{A}\bullet\mathbf{p})/mc. \tag{2.9}$$

Time-dependent perturbation theory gives the transition probability in Fermi's golden-rule form

$$P(E, h\nu) \sim |\langle f|\mathbf{A}\bullet\mathbf{p}|i\rangle|^2\, \delta(E_f(k)-E_i(k)-h\nu)\delta(E - [E_f(k)-\Phi]), \tag{2.10}$$

where all energies (except $h\nu$) are referred to the vacuum level, and $|i\rangle$ and $|f\rangle$ are the occupied initial state and the unoccupied final state, respectively. The first term ($|\langle f|\mathbf{A}\bullet\mathbf{p}|i\rangle|$) represents the strength of the interaction between the incident photon and the electron in a solid. The first delta function ensures energy conservation and the second delta function ensures that the kinetic energy measured outside the solid equals the final state energy inside minus the workfunction of the solid.

From conservation of energy and momentum:

$$E_f(k_f) - E_i(k_i) = h\nu \tag{2.11}$$

and

$$k_f - k_i = k_{photon} \tag{2.12}$$

Within the photon energy range considered (~100 eV), it is easily seen that k_{photon} is negligible compared with electron momenta. Therefore $k_f \sim k_i$, which is usually called a direct optical transition which appears vertical in a reduced Brillouin zone.

The next step for the photoelectron is to travel to the vacuum level. But not all of them can reach the surface. In the process, the photoexcited electrons may scatter with other electrons, plasmons, phonons, and consequently lose part of their energy and change their momentum. One of the consequences of such scattering is the secondary inelastic background intensity. The background, contributed by the inelastically scattered electrons, becomes dominant at low kinetic energies due principally to electron-electron scattering. If an excited electron is scattered many times, it may not have enough energy to be able to escape at all and finally it falls back to the occupied state. A mean free path λ is defined to describe the transport process. It is assumed that on average a photoelectron can travel over a mean free path before being scattered. The measured electron inelastic mean free paths λ for various materials have been compiled by Seah and Dench [25]. Figure 2.3 shows that λ follows a "universal" curve as a function of the electron kinetic energy. The general behavior of the mean free path is first a sharp decrease with increasing electron kinetic energy and a fairly flat minimum of 2-10 Å at energies between 20 and 200 eV, and finally an increase with increasing electron energy.

The transport function can be written as

$$T(E) = [\lambda(E)/\lambda_{ph}(h\nu)]/[1+\lambda(E)/\lambda_{ph}(h\nu)], \tag{2.13}$$

where $\lambda_{ph}(h\nu)$ is related to the photoabsorption coefficient of a solid at frequency ν. Typically, over the energy scale of a photoemission spectrum, $T(E)$ is a slowly varying function of the electron energy. To summarize, scattering can cause broadening in structure and changes in the relative intensities of peaks of solid but there is a close one-to-one relationship between the measured EDCs and the electronic structure in solid as a first approximation [24].

The last step in the photoemission process is the escape of the photoelectron from the solid. When the electron escapes the solid, it must overcome a surface potential barrier $E_F + \Phi$, where Φ is the work function of the solid. The primary effect here is to cut off the low-energy part of the EDCs. The escape from the solid finally is possible only for those

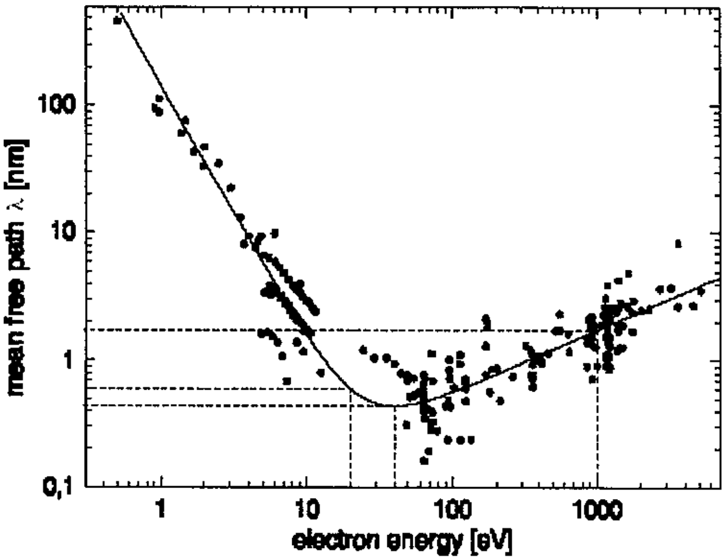

FIG. 2.3 The "universal" mean free path curve, electron mean free path for motion without inelastic scattering vs. electron energy (after [25]).

electrons with a kinetic energy component normal to the surface that is sufficient to surmount the potential barrier. Using a free-electron-like model for the excited photoelectron, the escape function becomes:

$$D(E) = \tfrac{1}{2}\,\{1-[(E_F + \Phi)/E]^{1/2}\} \quad \text{for } E > E_F + \Phi \tag{2.14}$$

$$= 0 \qquad \text{elsewhere.} \tag{2.15}$$

All electrons with $E > E_F + \Phi$ are assumed to escape if their velocities lie within a cone of half angle theta with axis normal to the surface, and $\cos\theta = [(E_F + \Phi)/E]^{1/2}$. It is noticed that both the transport function $T(E)$ and the escape function $D(E)$ are smooth, slowly varying functions of the photoelectron energy E and will not give rise to any extra features in the spectrum [26]. So we can say that any structure in the EDC is due to the optical excitation process. The resulting spectrum intensity $I(E)$ is called an energy distribution curve (EDC). The distribution in kinetic energy of photoelectrons outside the solid is scanned for a fixed photon energy, giving output intensity vs. electron kinetic energy.

There are other modes of spectra other than EDCs that one can take. The most important are the constant-final-state (CFS) mode and the constant-initial-state (CIS) mode, first applied by Lapeyre and co-workers [27]. In the CFS mode one can fix the electron kinetic energy and scan the photon energy, instead of fixing the photon energy and scanning the electron energy. In other words the mode is implemented by scanning the photon energy $h\nu$ while keeping constant E_{kin}, thereby scanning an initial state only. Therefore the spectral shape in CFS is related to the density of initial states modulated by dipole matrix elements. In the CIS mode both photon energy and electron kinetic energy are scanned synchronously so that $E_{kin}-h\nu$ is kept constant. As the photon energy is increased, the final state energy is increased by an equal amount, thereby keeping the initial state fixed. This mode provides the density of final states modulated by dipole matrix elements in the conduction-band region above the vacuum level. In the CIS mode, it is also possible to monitor the photoexcitation-cross-section of a particular initial state as a function of $h\nu$. Both these scans are illustrated in Fig. 2.4 along with an EDC [28].

There is a special case of the CFS scan that is sometimes used for the study of core levels. If the electron energy is set to a low kinetic energy, the electrons collected are almost all secondary electrons, most of which have been scattered inelastically. As a good approximation, a CFS spectrum taken at low kinetic energy represents the absorption coefficient as a function of photon energy. This technique also is called partial yield spectroscopy and it can often be used to probe $4f$ occupancy in rare-earth metals and their compounds, for the absorption spectrum or the $4d \rightarrow 4f$ excitation spectrum in this case, is very sensitive to the number of $4f$ electrons due to a large $4d \rightarrow 4f$ exchange and Coulomb interaction.

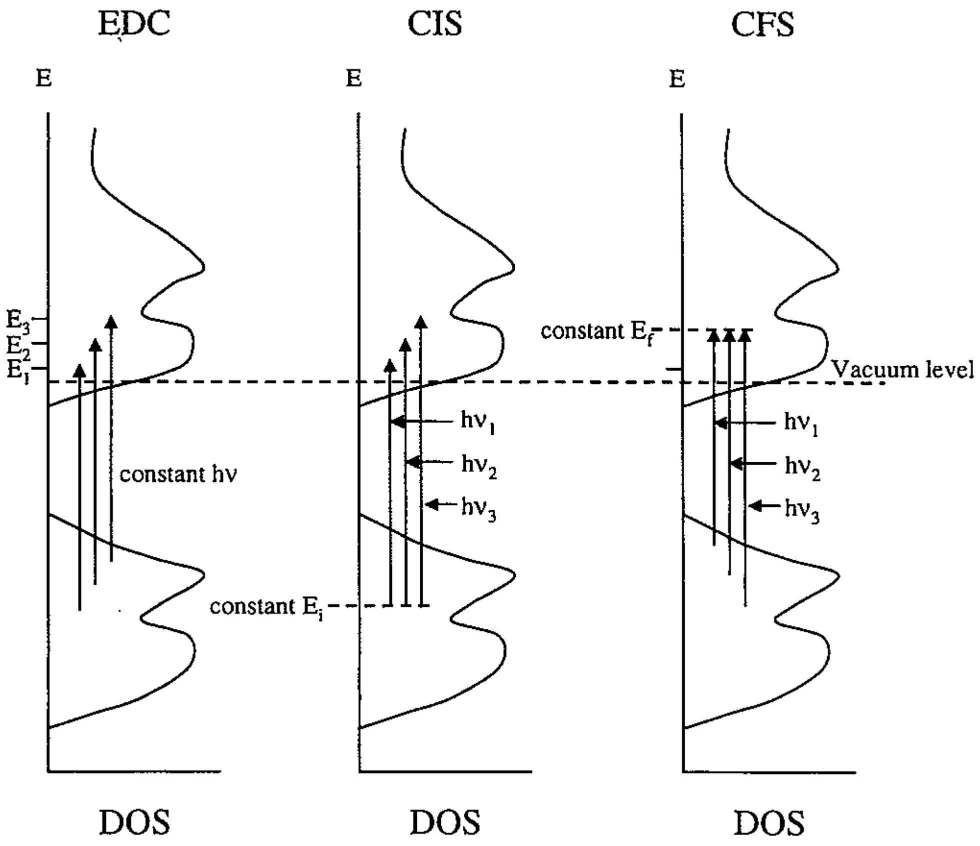

FIG. 2.4 Photoexcitation process in the three types of photoelectron spectra (after [28]).

Angle-resolved photoemission

In the photoemission process an electron below the Fermi energy (E_F) initially has energy E_i ("negative binding energy"), and after excitation due to the photon of frequency ν it has an energy $E_i + h\nu$. If the electron was excited to just above E_F it would not escape from the solid. There is a potential step, or work function Φ, that must be overcome before the electron can escape. Hence the experimentally measured photoelectron kinetic energy (E_{kin} : referenced to the vacuum level) outside is related by $E_{kin} = h\nu + E_i - \Phi$. The kinetic energy and the momentum of the emitted electron are determined by the angle-resolved analyzer, selecting only a small solid angle of photoelectrons leaving the sample:

$$E_{kin} = (\hbar^2/2m)\,(k_{\parallel}^2 + k_{\perp}^2), \tag{2.16}$$

where $k_{\parallel}$ and $k_{\perp}$ are the components of momentum in the vacuum, parallel and perpendicular the surface. Knowing the momentum and energy outside, we would like to determine the momentum and energy of the photoexcited electron inside the crystal and then E_i and k_i of the initial state from which the electron was excited. Gobeli *et al.* [29] showed that a sizable fraction of the electrons created by direct optical transitions can escape without scattering by phonons or imperfections, either in the volume or at the surface, by showing that the directional photoemissive yield from a crystal surface is strongly sensitive to the photon polarization angle for light at normal incidence. The assumption of direct, **k**-conserving transitions has been the correct model for the excitation process since early photoemission spectroscopy [29, 30, 31]. In this direct transition model, it is assumed that the momentum of an electron excited from one band to another is unchanged (since the photon momentum is negligible in comparison). Thus with energy conservation and momentum conservation (direct transition)

$$E_f = E_i + h\nu \tag{2.17}$$

$$k_f = k_i , \tag{2.18}$$

where E_f and E_i are the final-and initial-state energies of the electron in the solid, $h\nu$ is the photon energy, and k_f and k_i are the final- and initial-state wave vector, respectively. The objective of an angle-resolved photoemission spectroscopy (ARPES) experiment is to map $E_i(k_i)$ by measuring $E(k)$ in vacuum, which is to determine the energy and momentum of the initial state from the energy and momentum of the emitted electron (i.e. the kinetic energy and direction of the photoelectron in vacuum) [32]. In the photoemission process, the component of electron momentum parallel to the crystal surface ($k_{\|}$) is conserved upon escaping from the solid from the continuity of wave function and its normal derivative at the boundary [30, 31, 33]. So for a collection angle θ we have

$$k_{\|}(\text{inside}) = k_{\|}(\text{outside}) \text{ or } |\mathbf{k}_{\|}| = (2mE_{kin}/\hbar)^{1/2}\sin\theta. \tag{2.19}$$

But the perpendicular component $k_{\perp}$ is not conserved at the surface. The simplest approximation for the final state (E_f, k_f) is a parabolic free-electron-like band in a constant inner potential V_0. The external measured kinetic energy and the internal final state energy are related by

$$E_{kin} = \hbar^2 k_f^2/2m - V_0 \quad (V_0 > 0), \tag{2.20}$$

where m is the mass of the electron and V_0 is a constant positive inner potential referenced to E_F which defines the zero of the free-electron final-state band. This model was first applied by J. Stöhr [34] and has been employed widely. It has proven extremely successful, and has been shown to be a good approximation. The inner potential is related not only to the loss of kinetic energy but also to the altering the photoelectron path as described below. If an electron of kinetic energy E_{kin} (relative to the vacuum level) with a fixed θ from the surface normal is detected, Eq. (2.20) restricts the location of k_f and k_i to a certain circle in k space given by

$$k_{f\parallel} = \hbar^{-1}[2mE_{kin}]^{1/2}\sin\theta = 0.512(\text{Å}^{-1})[E_{kin}/\text{eV}]^{1/2}\sin\theta \qquad (2.21)$$

$$k_{f\perp} = \hbar^{-1}[2m(E_{kin} + V_0) - h^2k_{\parallel}^2]^{1/2} = 0.512(\text{Å}^{-1})[(E_{kin}+V_0)/\text{eV} - 3.84\text{Å}^2k_{f\parallel}^2]^{1/2}, \qquad (2.22)$$

where E_{kin} and V_0 are in eV. Eq. (2.22) essentially describes the refraction of the outgoing photoelectron when it crosses the potential step V_0 at the surface. Straight lines would be obtained if refraction at the surface were neglected. By combining the escape angle and the photon energy properly, one can reach the whole Brillouin zone [35]. Therefore, when performing an ARPES experiment at constant photon energy we actually follow a circular path in k space rather than a straight line [36]. The radius of this circle is determined by the equation

$$(k_{\parallel}^2 + k_{\perp}^2)^{1/2} = [2m/\hbar^2(E_{kin} + V_0)]^{1/2} = [2m/\hbar^2(h\nu - E_B - \Phi + V_0)]^{1/2}. \qquad (2.23)$$

Figure 2.5 shows a schematic of the external geometry of an angle-resolved photoemission measurement we performed and the Brillouin zone (BZ) of the body-centered tetragonal structure with labeled symmetry points. One slice through the BZ for this structure, the ΓXPZ plane on which we performed ARPES is also shown. The emission plane of the outgoing photoelectrons in the BZ is indicated as the hatched ΓXPZ plane with photoelectron emission angle θ. Our samples are oriented in order that the $k_{\parallel}$ component of the photoelectron is along the [110] direction, as shown in Fig. 2.5. Figure 2.6 shows that cir-

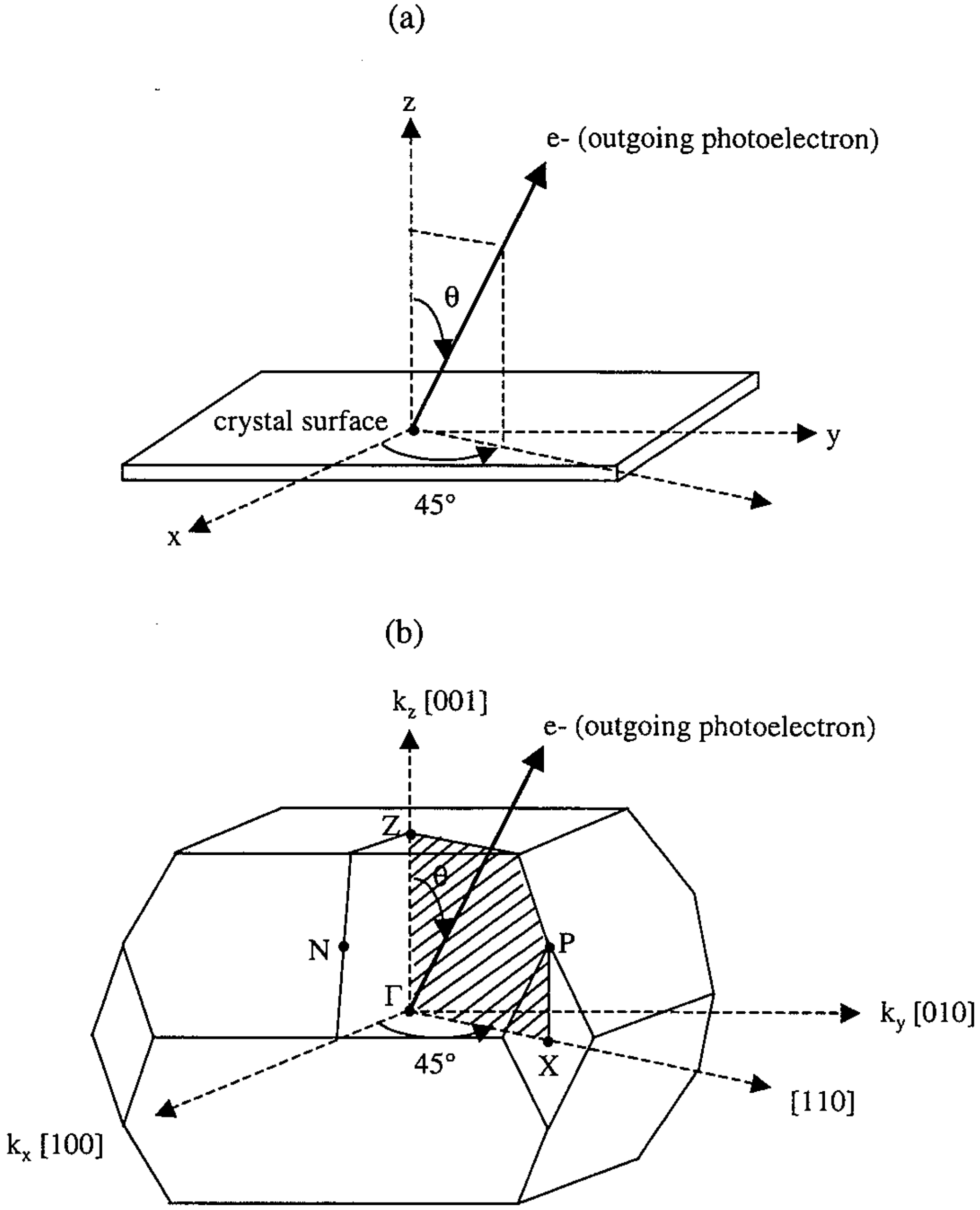

FIG. 2.5 (a) Illustration of an angle-resolved photoemission geometry. Z axis is parallel to the surface normal. (b) Brillouin zone (BZ) for a body centered tetragonal structure. The high-symmetry ΓXPZ plane used in our ARPES measurement is indicated as the hatched one.

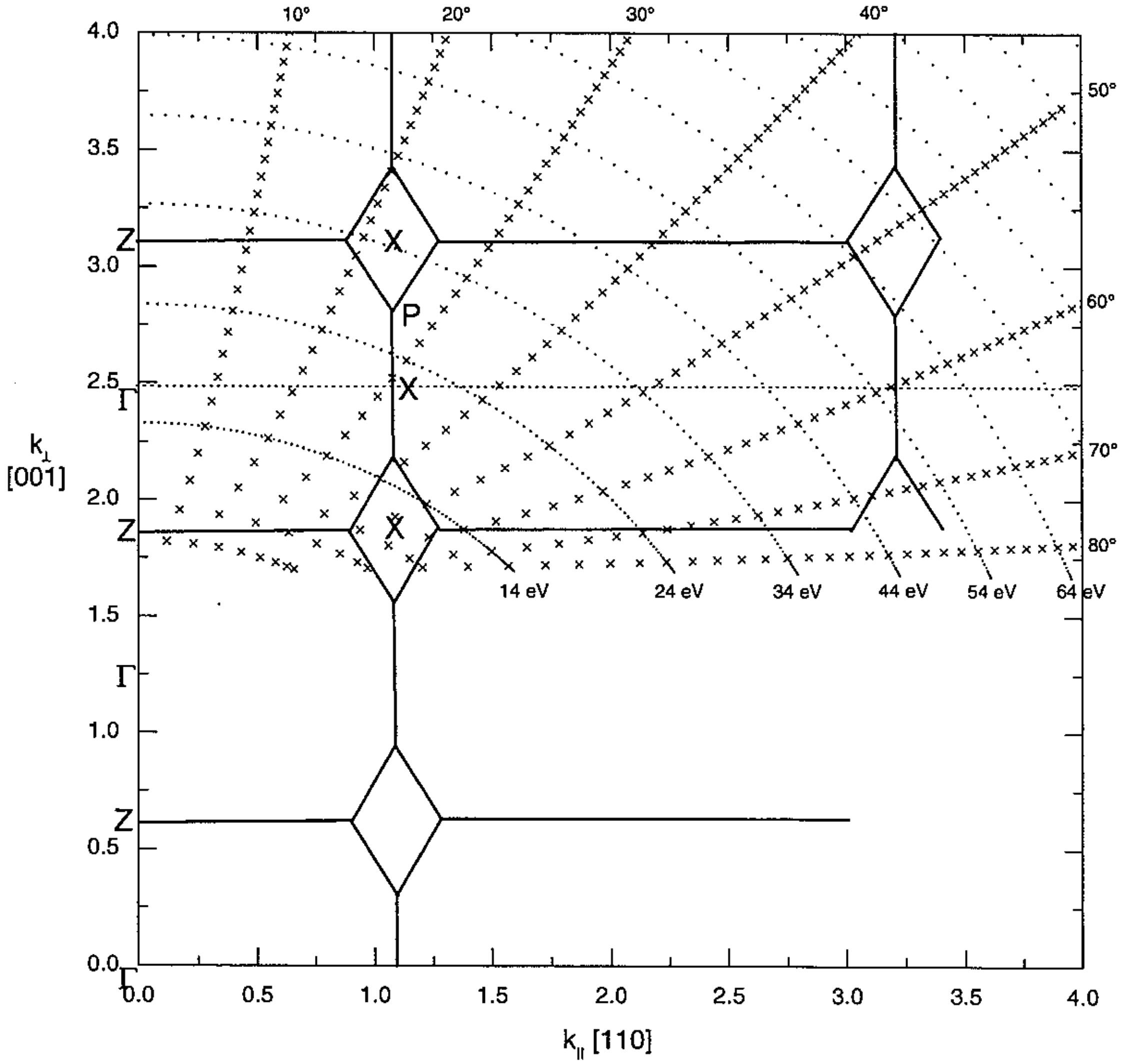

FIG. 2.6 Cuts through the extended Brillouin zone (BZ) of $EuNi_2Ge_2$. The vertical axis is $k_\perp$ relative to the (001) surface. The horizontal axis ($k_\parallel$) is the momentum parallel to the [110] direction. Circular paths through the BZ are various constant photon energies for states near E_F. BZ in the ΓXPZ plane was also drawn. The 'x' marks show the k location for the observed transition for a fixed collection angle.

cular paths composed of dots through the BZ of $EuNi_2Ge_2$ in the ΓXPZ plane for an inner potential $V_0 = 11.0$ eV with respect to E_F are contours of various constant photon energies for states near E_F, assuming a free-electron final state. Photoemission data can be taken using constant photon energy with a circular path and angle given by this Fig. 2.6 [23, 32]. In other words, as the electron detector angles are varied for fixed photon energy, a circular *k*-space surface is traversed. A series of energy distributions can be recorded for photon energies and electron collection angles. The photon energy will be tuned to change the radius of the circular path in order to access the two-dimensional BZ.

Energy band mapping [35, 37, 38]

The electronic states in the solid are described by energy bands. In the single-electron picture, electronic states in a solid are represented by plotting their energy versus wavevector, commonly referred to as the band structure. In this scheme, the photoexcitation process can be drawn as a transition from states in an occupied band into states in an unoccupied band. Energy band mapping is to determine the relation $E(\mathbf{k})$ experimentally. Such energy band dispersions $E(\mathbf{k})$ are energy eigenvalues for delocalized electrons in a periodic (i.e. crystalline) medium according to Bloch's theorem. Many of the important, fundamental physical properties of a solid can be determined, such as electrical and magnetic properties, optical properties, lattice constant, and elastic properties. It's possible to calculate these properties from $E(\mathbf{k})$ band dispersions and $\psi(\mathbf{r})$ wavefunctions [39]. It is often said that photoemission spectroscopy is the most powerful experimental tool in determining electronic band structure. This is done by measuring the angle of emitted photoelectrons as well as their kinetic energies. For comparison, in optical spectroscopy only the energy-band separations at various optical critical points in k space (i.e. energy difference between initial and final state) are determined but photoemission spectroscopy provides information about the absolute location of energy bands at different values of $\mathbf{k}$ relative to the Fermi energy (E_F).

A schematic diagram for optical transitions between two bands and corresponding photoelectron spectra are shown in Fig. 2.7. A plot of photoelectron intensity as a function of kinetic energy E_{kin} (or binding energy) will show peaks whenever optical transitions between bands are allowed. The tails at higher binding energies (slow electrons) are electrons that have lost energy on escaping from the sample by inelastic scattering.

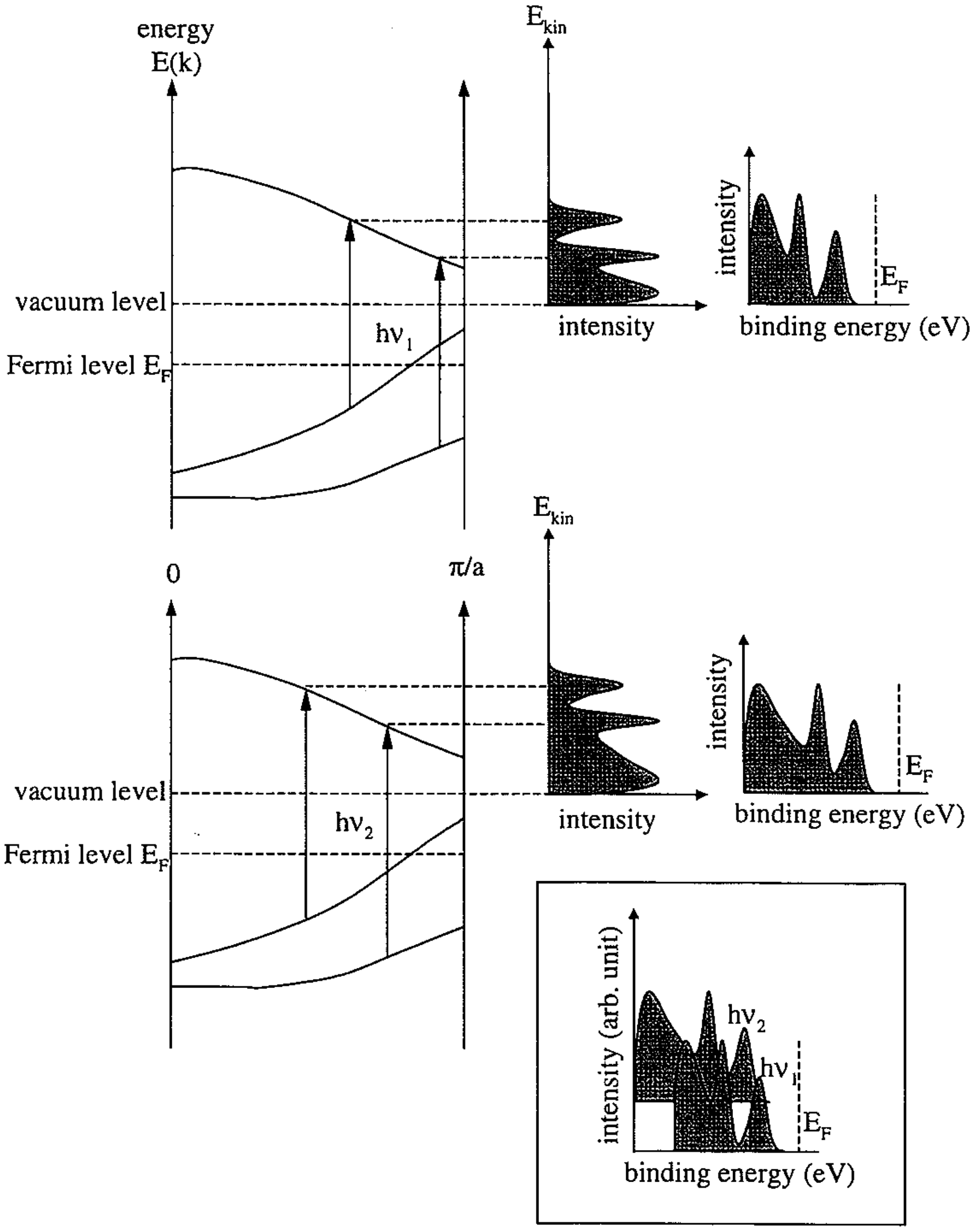

FIG. 2.7 Optical transitions between two bands and photoelectron intensity in the vacuum as a function of kinetic energy or binding energy. The two spectra are shown together in the inset ($h\nu_2 > h\nu_1$)

The free-electron band structure of Al along the ΓX direction in the reduced zone scheme is given in Fig. 2.8. Transitions along ΓX occur in the experimental situation where one has a (001) crystal plane with the detector parallel to the surface normal ($k_{||} = 0$ for every detected electron). In the photoemission experiment energy and wave vector are conserved: $E_f - E_i = h\nu$ and $\mathbf{k}_f = \mathbf{k}_i + \mathbf{G}$, where $\mathbf{k}_i$ and $\mathbf{k}_f$ are the wavevector of the electron in the initial and final state. The crystal provides the momentum in the photoexcitation process by adding the bulk reciprocal lattice vector **G**. The momentum conservation equation corresponds to the situation in an extended zone scheme.

In the reduced zone scheme, as shown in Fig. 2.8, the wave vector of the final state is folded back into the first BZ, since in a periodic potential all points that can be connected with a vector of the reciprocal lattice are equivalent. By this construction each band of the reduced zone scheme corresponds to a different **G**. The only allowed transition for $h\nu = 52$ eV is shown in Fig. 2.8-(a). The requirement that $k_i = k_f$ means that one is performing a vertical transition in a reduced zone scheme, and since the initial state has to be occupied, the final band must have the same reduced momentum and be separated in energy from the initial state by the photon energy. If the photon energy is increased from 52 eV the value of k will increase causing the initial state to move nearer to the X point and the initial-state energy will increase. If the photon energy is decreased the value of k will decrease and the initial-state energy will move closer to Γ. At hν ~ 37 eV the center of the BZ, Γ, is reached, and if the photon energy is reduced further, the initial states energy will increase again. A similar behavior will occur around $h\nu = 84$ eV, where the X-point is reached. Generally speaking, such extrema in the observed binding energies correspond to transitions occurring at points

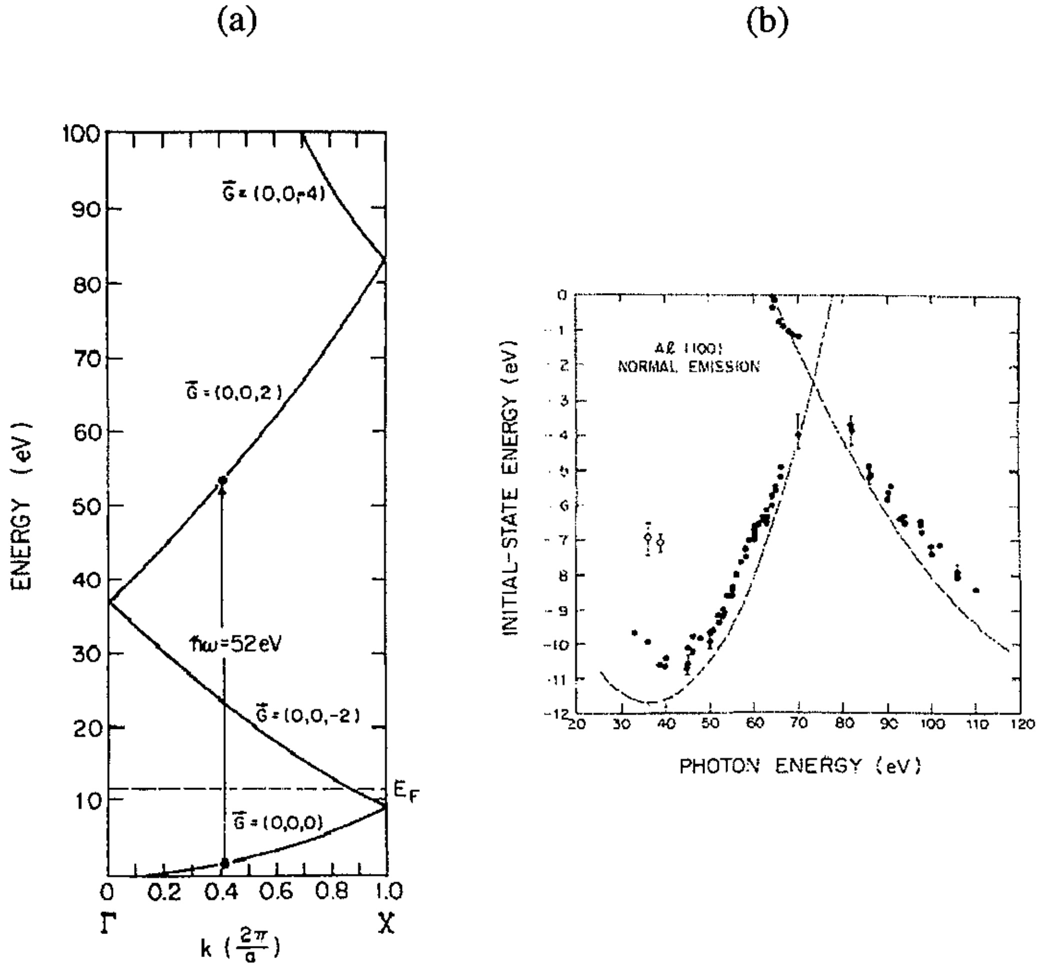

FIG. 2.8 (a) Free-electron band structure of Al along the ΓX direction in the reduced zone scheme and (b) normal emission peak energies of a photoemission measurement on Al as a function of the photon energy $h\nu$. The G values and a radiative transition with $h\nu$ = 52 eV are shown. The dashed lines are the prediction from the free-electron band (after [37]).

of high symmetry in the BZ. The actual data for the initial states along the ΓX direction are shown in Fig 2.8-(b). The strong relationship between photoemission spectra and electronic band structures has been studied extensively for almost four decades [21, 22, 40].

Resonance Photoemission

Resonance photoemission gives rise to a better understanding of the electronic structure of solids and provides a useful tool for distinguishing the particular resonant features from others because of its special emphasis on only some features. Resonance photoemission is also a powerful technique in which the photon energy dependence of photoionization cross sections is utilized to enhance and suppress emission from electronic states of different character. A comprehensive review in this field has been published by Allen [41].

This resonant enhancement occurs whenever the photon energy $h\nu$ is just large enough to excite a core electron into an unoccupied state, since a photon can be absorbed into a resonant state without ionization if the photon energy matches the energy difference between the ground state and an excited state below threshold for photoemission. For a rare earth, for example, the $4d \rightarrow 4f$ resonance has been used to isolate the $4f$-derived features from the spectra. The resonance photoemission arises from the interference between the following two processes. In a simplified single-electron picture, one is an Auger decay process (relaxing a highly excited atom by filling a core-level vacancy with an electron from an outer level) following photoabsorption of a $4d$ electron to an unoccupied, localized $4f$ state, and a Super-

Coster-Kronig decay (the two final holes are in the same shell as the initial state hole) of the intermediate state can be written as

$$h\nu + 4d^{10}4f^{n}(5d6s)^3 \rightarrow 4d^{9}4f^{n+1}(5d6s)^3 \rightarrow 4d^{10}4f^{n-1}(5d6s)^3 + e^-, \qquad (2.18)$$

where n is the number of electrons in the f orbitals and e^- is the continuum final state of the ejected electron. The other process leading to the same final state is excitation by the direct photoemission process,

$$h\nu + 4d^{10}4f^{n}(5d6s)^3 \rightarrow 4d^{10}4f^{n-1}(5d6s)^3 + e^-. \qquad (2.19)$$

The electron energy carried away by the direct photoemission process is the difference between initial and final electronic states, which is indistinguishable from the process shown in Eq. (2.18). Quantum-mechanical-interference occurs between these two types of processes involving the same initial and final states, thereby enhancing the electron emission as $h\nu$ is through such a resonance. The resulting photon-energy-dependent intensity profile can be described by the Fano interference formalism [42]. In the present study of $EuNi_2Ge_2$ and $GdNi_2Ge_2$, it was found that the $4f$ contribution can be highlighted by comparing spectra taken at 141/149 eV (on resonance) and 131/135 eV (off resonance).

CHAPTER 3. EXPERIMENTAL DETAILS

Synchrotron radiation source and beamline

Synchrotron radiation is generated by highly relativistic electrons moving on circular orbits. The present photoemission study was carried out at the Aladdin electron storage ring at the SRC (Synchrotron Radiation Center) in Stoughton, Wisconsin. The electron beam in the storage ring is kept at an operational energy of 800 MeV or 1 GeV, which produces intense, highly collimated and polarized photons in a wide spectrum from ultraviolet to soft-X-ray energy range. Comprehensive studies of synchrotron radiation sources, facilities, and instrumentation can be found in Refs [43, 44, 45, 46, 47, 48, 49].

At Aladdin, the electrons travel along a path with a circumference of 88.9 m shown in Fig. 3.1. After the 108 MeV microtron injects the electrons into the storage ring, the radio-frequency cavity (rf cavity) quickly increases the energy to 800 MeV-1 GeV. The electrons are grouped in 15 bunches around the ring. The electrons are kept moving along the direction of their motion with an oscillating electric field in the rf cavity which periodically acts on the circulating electrons, replenishing the energy they lose due to the emission of synchrotron radiation. The rf cavity operates at 50.582 MHz.

Magnetic fields are used to bend the trajectory of the electrons and force their path into the shape of the storage ring. Since a change of direction of velocity is an acceleration, electromagnetic radiation, i.e., synchrotron radiation, is emitted at each bending magnet in the storage ring. There are twelve bending magnets around the ring, each one bending the

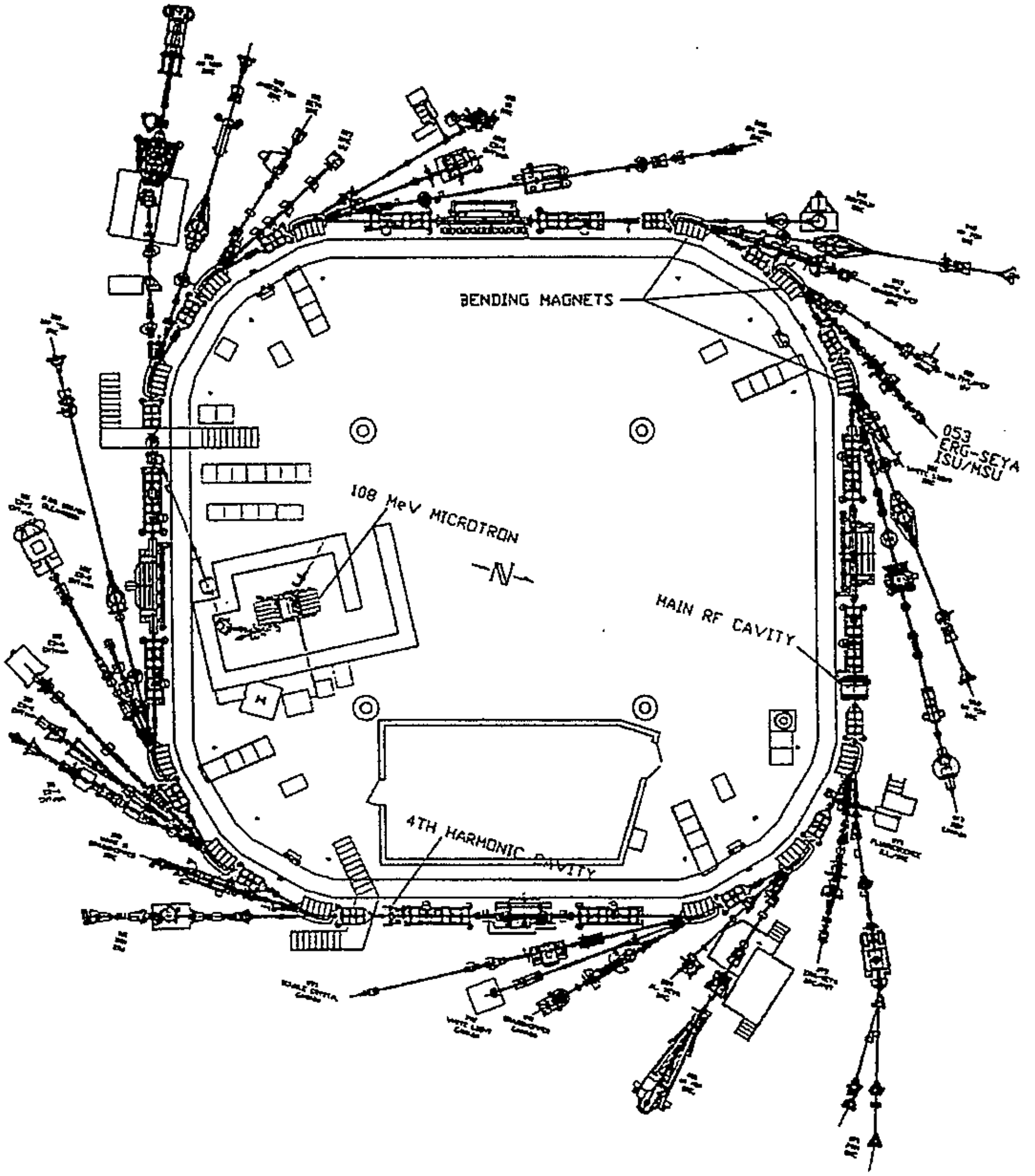

FIG. 3.1 Top view of the Aladdin electron storage ring at the Synchrotron Radiation Center in Stoughton, WI. Beam line #053 in the Iowa State/Montana State ERG/Seya combined monochromator beamline where we performed our experiment.

beam with a magnetic radius of 2.083 m. The bending magnets produced synchrotron radiation for our experiments.

For photoemission spectroscopy the "white light" has to be monochromatized and focused. With two types of monochromator combined together (ERG and Seya), the beamline accesses a very wide range of photon energy (5-1000 eV), so that both core and valence electrons can be studied on the same sample. The Extended-Range Grasshopper (ERG) and the Seya beamline was built by Dr. C. G. Olson [50]. The schematic layout of the two monochromators is shown in Fig. 3.2. The ERG is a grazing-incidence monochromator which provides excellent resolution in a very broad spectral range and is an advanced popular version of the Grasshopper monochromators in which components are moved individually by computer controls rather than mechanical linkages between components to accomplish the coordinated motion of the optical components to keep them on the Rowland circle. The Seya is a near normal-incidence monochromator which uses a spherical grating at an angle of incidence of about 35°. In general the Seya is for low and the ERG is for high photon energies. The Seya has four rotating selectable gratings with different ruling densities as shown in the upper part in Fig.3.2. All of the gratings are concave spherical. The two monochromators were configured so that they share a common refocusing mirror. This means that only the movement of a single plane mirror is required to select the monochromator illuminating the sample. Their spectral output characteristics are shown in Fig. 3.3. The Seya 1800 l/mm grating with a slit width of 200 μm was used in the photon energy range of 14 – 38 eV. The lower part in Fig. 3.2 is the ERG. Two spherical gratings, 2m and 5m in radius, cover the photon energy range from 38 eV to about 1000 eV. The photons used in the present work, from 40 eV to 168 eV, are provided by the 2-m ERG

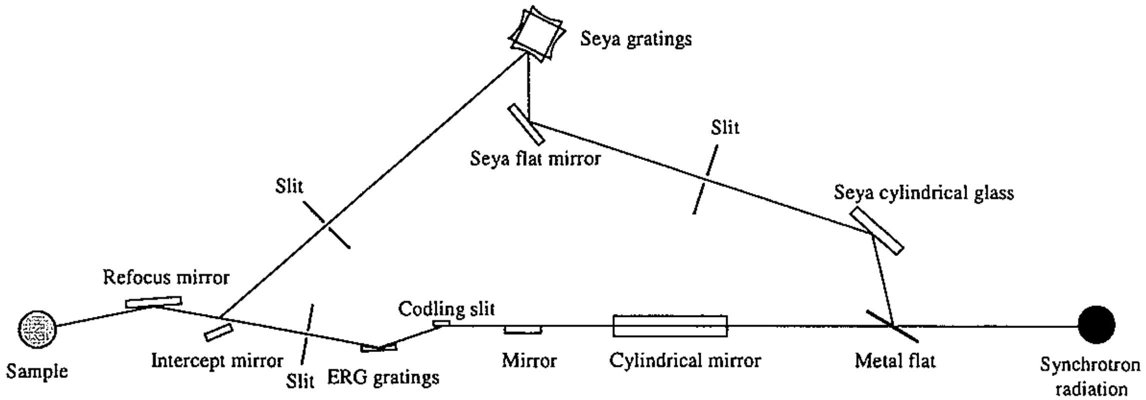

FIG. 3.2 Schematic layout of the Ames/ Montana ERG /Seya combinned monochromator beamline (after [50]).

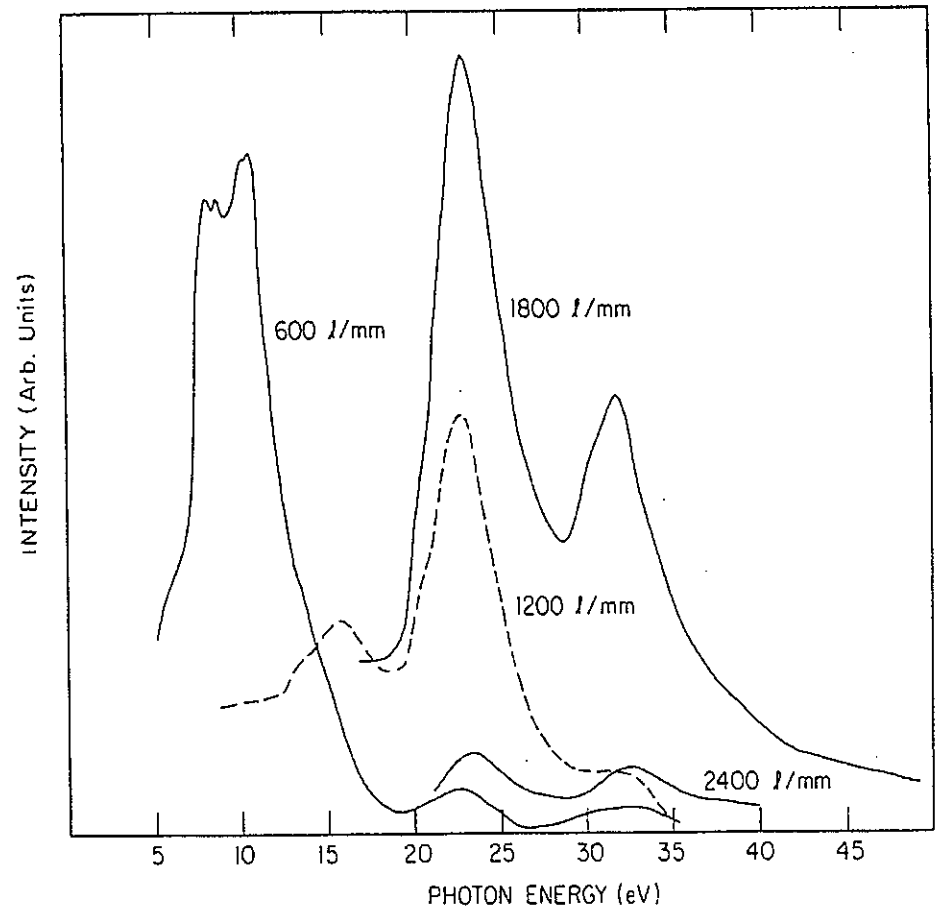

FIG. 3.3 Spectral output of the Seya (after [50]).

grating. The range and dispersion of all the beamline gratings is shown in Fig. 3.4. The beam line is kept under ultra-high-vacuum so that it reduces the absorption of the light and the contamination of the equipment and samples.

Electron Energy Analyzer

In our experiment, a VSW (Vacuum Science Workshop) concentric hemispherical electron energy analyzer [51] was used for collecting and analyzing the emitted photoelectrons. A schematic representation of the analyzer is shown in Fig. 3.5. The analyzer is composed of a 1:1 retarding lens in front of the entrance aperture, which focuses electrons onto the entrance aperture, two concentric hemispherical deflectors to disperse the electrons according to their energies, and the a channel electron multiplier which amplifies the signal at the exit of the deflectors.

The selected electron pass energy (E_p) is determined by the potential difference (ΔV) across the two hemispheres and their radii R_1 and R_2:

$$E_p = e\Delta V/[(R_2/R_1) - (R_1/R_2)], \tag{3.1}$$

where e is the charge of an electron, R_1 is the radius of the inner sphere, and R_2 is the radius of the outer sphere.

In fact there are two modes we can operate with this analyzer [52]. Increasing ΔV causes the pass energy (E_p) to increase but the resolution will decrease as one scans. The other type of scan is to keep ΔV and E_p constant, scanning by retarding or accelerating the in-coming

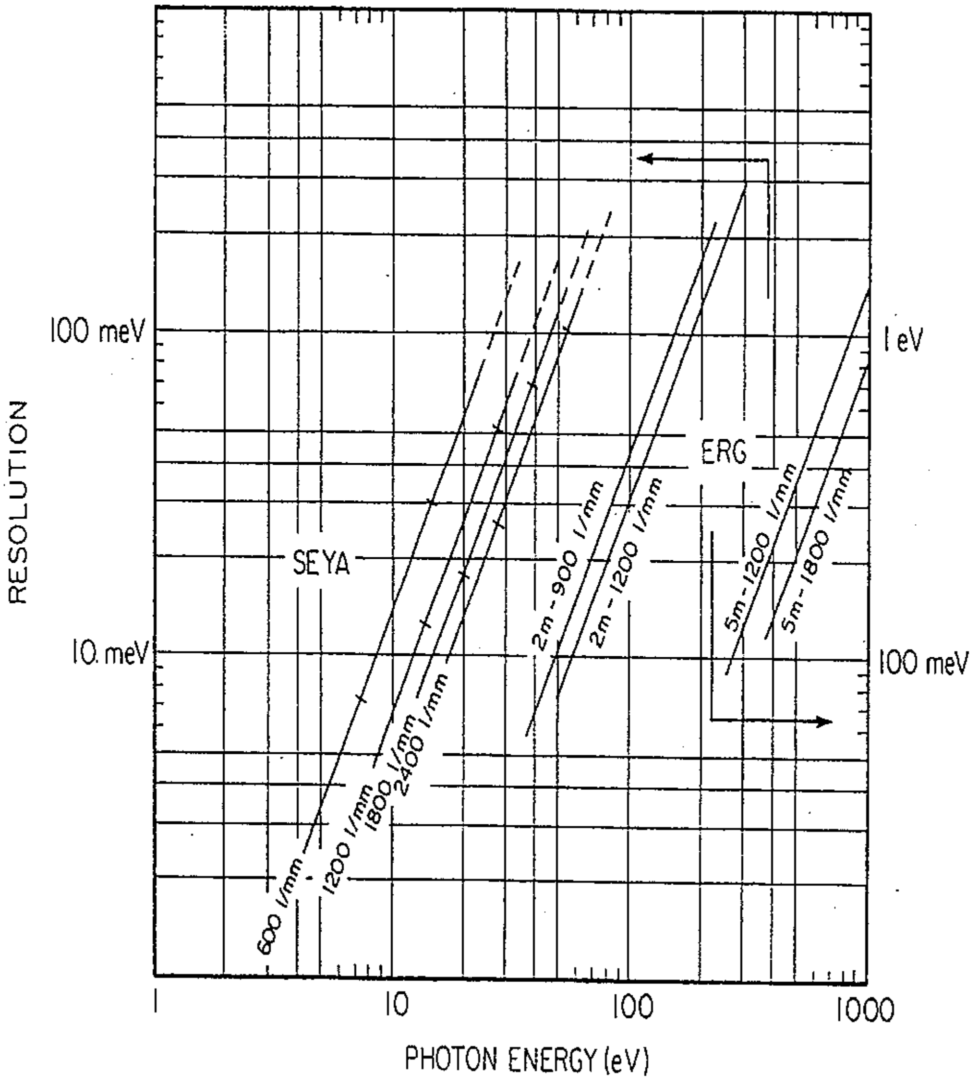

FIG. 3.4 The range and dispersion of all the beamline gratings (after [50]).

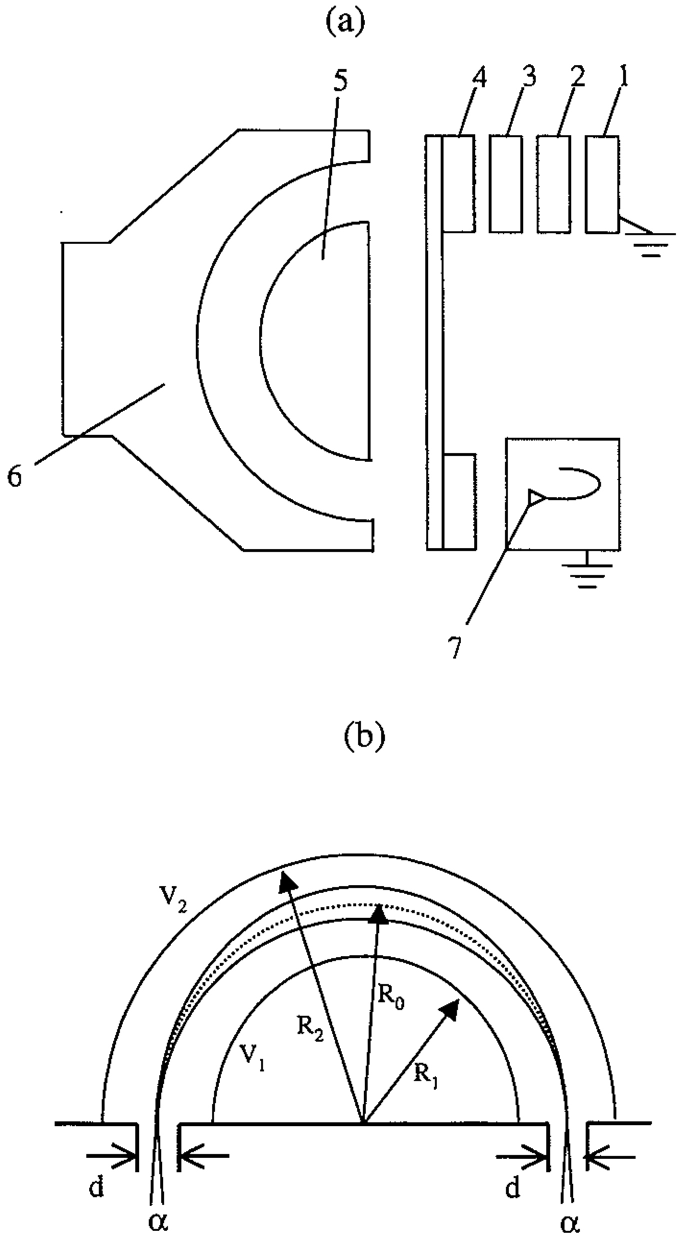

FIG. 3.5 (a) Schematic diagram of the hemispherical electron energy analyzer.
1-4: input lens; 5.6: hemisphere deflectors; 7: channeltron.
(b) A detailed view of a cross section through the hemisphere deflector.
V_1 and V_2 are the voltages on the inner and outer hemispheres respectively

electrons. In this mode, an input lens could usually be used to retard incoming electrons so that E_p is always relatively small (1-10 eV) and high constant resolution can be achieved.

The analyzer has an angular acceptance of 2° which corresponds to a k resolution of 0.075 Å^{-1}. The energy resolution of the analyzer is determined approximately by

$$\Delta E = E_p\,[(d/2R) + (\alpha^2/4)], \tag{3.2}$$

where E_p is the pass energy, d is the slit width, R is the mean radius of the hemispheres, and α is the full angle of electrons entering the analyzer at the entrance slit.

Usually, α is only a few degrees, and the second term can be neglected. For our analyzer, $d = 1$ mm, $R = 50$ mm. Therefore, the energy resolution of our VSW analyzer is about 1% of the pass energy [53].

Experimental procedures

$EuNi_2Ge_2$ and $GdNi_2Ge_2$ crystallize in the $ThCr_2Si_2$ structure having a body-centered tetragonal (bct) lattice with space group I4/*mmm*. The corresponding simple tetragonal unit cell is shown in Fig. 3.6. The experimental lattice parameters are $c = 10.10$ Å and $a = 4.14$ Å for $EuNi_2Ge_2$, and $c = 9.783$ Å and $a = 4.063$ Å for $GdNi_2Ge_2$ [54]. Single crystals of $EuNi_2Ge_2$ and $GdNi_2Ge_2$ were provided by Dr. Paul Canfield of the Ames Laboratory (DOE). These crystals were grown using a high-temperature-solution-growth technique [55]. All photoemission experiments were carried out at the Ames/Montana ERG/Seya beam-line [50] at the Synchrotron Radiation Center, in Stoughton, Wisconsin. Before mounting the crystals

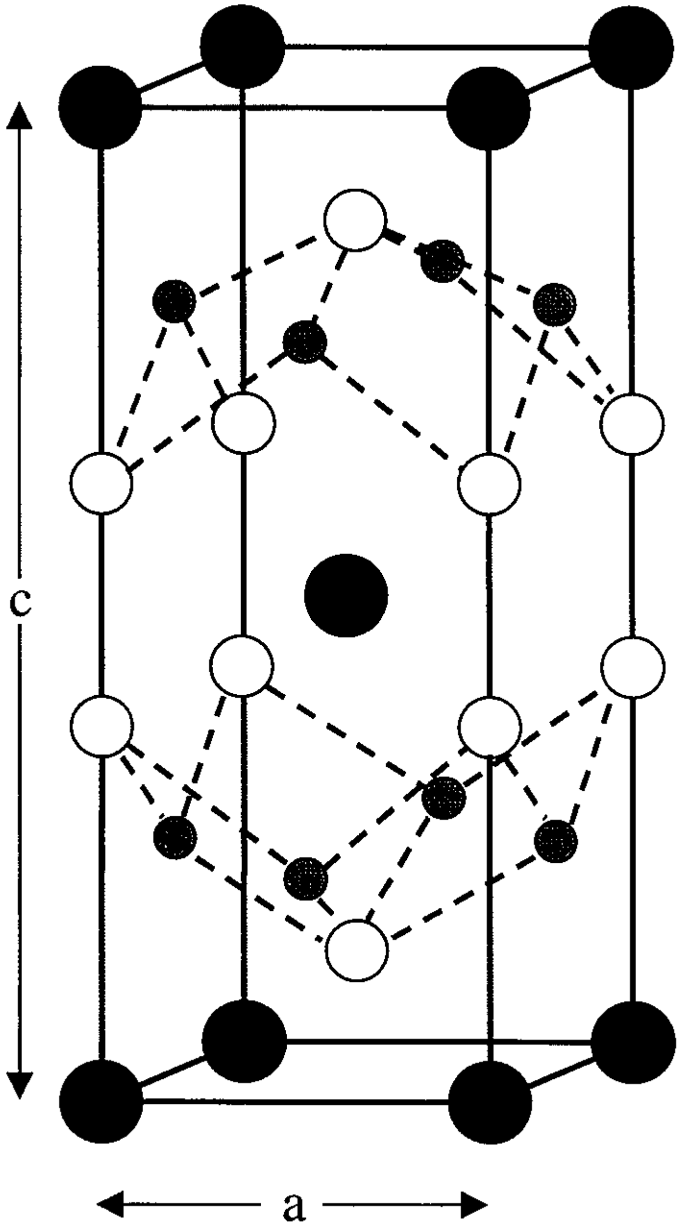

FIG. 3.6 Crystal structure of $EuNi_2Ge_2$ and $GdNi_2Ge_2$. Eu or Gd, Ni, and Ge atoms are represented in large filled circles, small shaded circles, and the white circles respectively.

in the stainless-steel vacuum chamber, Laue X-ray diffraction patterns were taken to determine the crystals' orientation, indicating that the [001] direction (*c*-axis) is the surface normal. Inside the vacuum chamber, there is a double layer of μ-metal for shielding the earth's magnetic field. A chamber with a very low field is important for high-resolution valence band studies, since a pass energy of the electron energy analyzer as low as possible is desired. The chamber is equipped with an ion-sputtering gun which was used for cleaning the Pt foil for the Fermi-energy (E_F) reference.

The single crystals of $EuNi_2Ge_2$ and $GdNi_2Ge_2$ had typical dimensions of ~5 mm × 5 mm × 2.0 mm. Both samples were oriented by Laue X-ray diffraction and mounted on aluminum posts with Torr-seal epoxy. These posts were then attached to the end of the copper cold finger of a closed-cycle helium refrigerator. Electrical contact was made by applying a thin layer of Aqua-Dag over the Torr-Seal Epoxy. A second Al rod was then mounted on top of the samples. Pumping was by an ion pump and two titanium sublimation pumps. A base pressure of 3×10^{-11} Torr was achieved following a 100-125°C bakeout for 24 hours to reach minimum pressures. The samples were cleaved by prying on the top Al rod in the sample chamber under a pressure of lower than 3×10^{-11} Torr, and temperature below 20 K. The clean surfaces were (001) planes. The temperature of the samples was measured with a Chromel-CuFe thermocouple and adjusted via a resistor imbedded in the cold finger. The photoelectrons were collected and energy analyzed by a 50 mm radius hemispherical analyzer [51] which was movable with two degrees of rotational freedom. The analyzer has a Gaussian instrument function with a FWHM of 20 meV at a pass energy of 2 eV, and 50 meV at a pass energy of 5 eV. The overall energy resolution of the experiment (monochromator plus electron energy analyzer), determined from the Fermi edge of a sputtered Pt foil, (FWHM, full width at half maximum) was about 49 meV at hν~22 eV and 145 meV at hν~70 eV. The analyzer input lens had an angular acceptance of 2°, about 6 % of the distance from Γ to X in the Brillouin zone. The Fermi energy (E_F) of the system was calibrated from the valence-band spectrum of a freshly sputtered Pt foil in electrical and thermal contact with the samples. All the spectra were normalized to the Au mesh current. The angle of incidence of the *p*-polarized photons was ~ 40° with respect to the sample surface normal. The sample alignment was determined *in situ* by using the symmetry of the dispersion of spectral features at high-symmetry points. During the experiment, the temperature was kept under 20 K. At this temperature all of the samples are antiferromagnetic.

CHAPTER 4. RESULTS AND DISCUSSION

Resonance photoemission of $EuNi_2Ge_2$ and $GdNi_2Ge_2$

To look for Ni 3*d* character in $EuNi_2Ge_2$ and $GdNi_2Ge_2$ we use resonance photoemission spectroscopy. All spectra were taken on single-crystal $EuNi_2Ge_2$ and $GdNi_2Ge_2$ (001) surfaces. Figure 4.1 is an EDC of $EuNi_2Ge_2$ taken at a photon energy above the Ni $3p \rightarrow 3d$ core absorption threshold, while Fig. 4.2 was taken at a photon energy below threshold (metallic Ni 3*p* has a binding energy of ~ 67 eV). Since the photoionization cross-sections for the *s* and *p* states are comparatively low [56], the spectrum in Fig. 4.1 will be dominated by transitions from the Eu 4*f* and Ni 3*d* states. The difference in shape of the two spectra can be seen quite clearly, with states in the top half of the band exhibiting a much stronger resonant enhancement, a well-defined peak at a binding energy of 1.4 eV for 72 eV photon excitation, showing that there is a great deal of Ni 3*d* in character at a binding energy (BE) of 1.4 eV. In Fig. 4.1 we can also see a resonant enhancement at a binding energy of 7.4 eV, which is a Ni 3*d* satellite [57] which is often produced on the higher binding energy side of the main peak if the screening of the core hole is poor. The Ni 3*d* satellite related to this material will be explained in detail later. Resonance photoemission is the effect in which photoemission from *d*-electron states is enhanced when the energy of the incident photons exceeds a threshold value related to the interband transition energy between a low-lying 3*p* core level and empty valence-band states near E_F. This resonant enhancement occurs whenever the photon energy is tuned to excite a *p* to *d* transition. The process can be described in an atomic picture as follows. Two possible paths lead to the same final state.

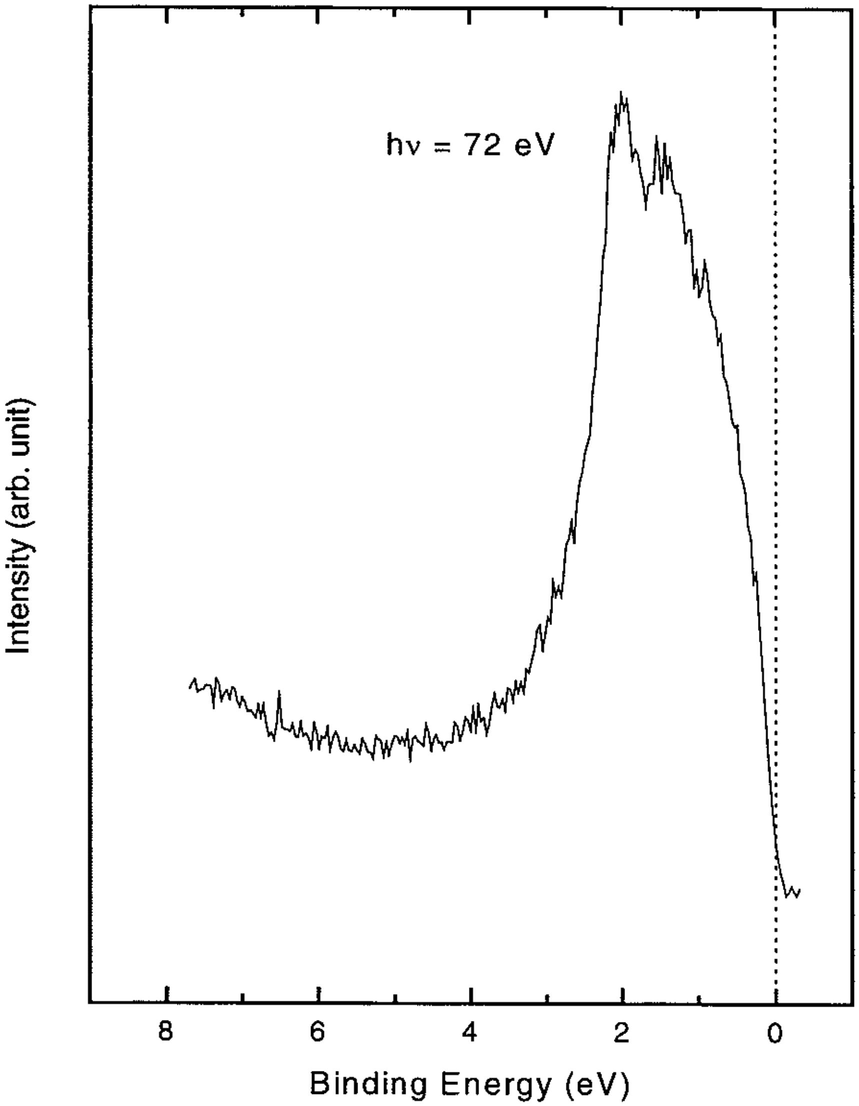

FIG. 4.1 A 9 eV wide EDC of the valence band of $EuNi_2Ge_2$ taken with a photon energy of $h\nu = 72$ eV, which is above the Ni $3p \rightarrow 3d$ core absorption threshold.

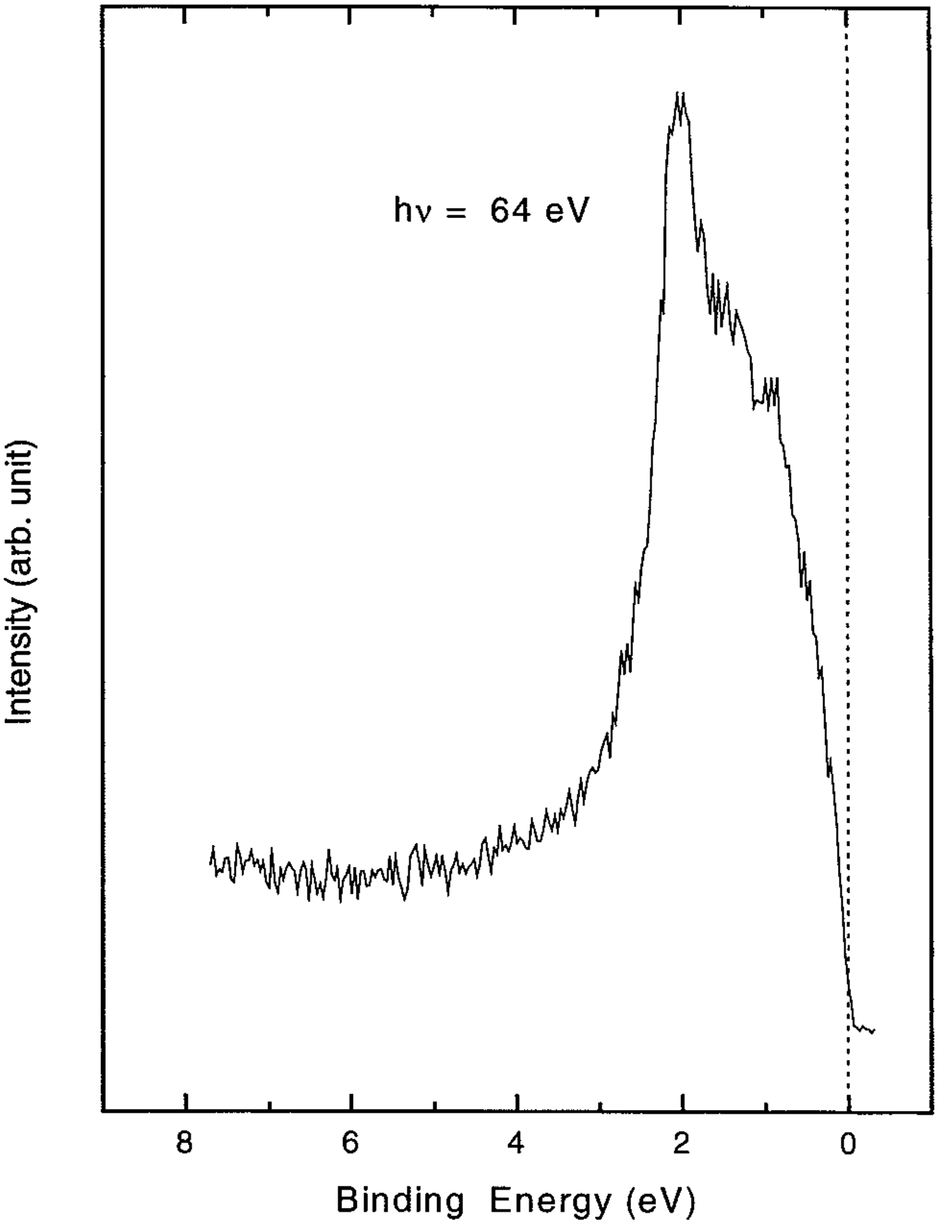

FIG. 4.2 An EDC of $EuNi_2Ge_2$ taken at a photon energy of 64 eV, which is below the Ni $3p \rightarrow 3d$ core absorption threshold.

$$3p^6 3d^9 + h\nu \rightarrow 3p^6 3d^8 + e^- \qquad (4.1)$$

$$3p^6 3d^9 + h\nu \rightarrow [3p^5 3d^{10}]^* \rightarrow 3p^6 3d^8 + e^- \qquad (4.2)$$

A photon of energy $h\nu$ ionizes the neutral atom and ejects a $3d$ electron with kinetic energy in path Eq. (4.1) which corresponds to direct photoemission from a $3d$ state. If the photon energy is equal to, or slightly greater than, the $3p \rightarrow 3d$ interband separation, we can get optical absorption via path Eq. (4.2) which corresponds to excitation of a $3p$ electron to an unoccupied d state, where the asterisk indicates an atom or ion in an excited state. This state can decay by direct recombination, the one that is responsible for the resonance. The excited state transfers all of its energy to the emitted electron in an Auger-type decay which fills the $3p$ hole and ejects a continuum electron from the $3d$ portion of the valence bands. The two processes overlap coherently at the threshold energy. Their amplitudes add, and upon taking the absolute square to get the cross section, interference may occur, giving rise to the resonant enhancement.

Figure 4.3 shows a 12 eV wide EDC of the valence band with photon energies varying through the Ni $3p \rightarrow 3d$ core absorption threshold (hν ~ 66 eV). We can see a resonant enhancement of the Ni $3d$ satellite, about 7.4 eV, indicating the Ni $3d$ character around the Fermi edge. The so-called 6 eV valence band satellite is a well-known feature in EDCs from Ni, which was first observed by Hüfner and Wertheim [58] in X-ray photoelectron spectra and Guillot *et al.* in ultraviolet photoemission [57]. At this photon energy direct photoemission from the valence band (assuming screening by a $4s$ electron) may be described by

$$3p^6 3d^9 + h\nu \rightarrow 3p^6 3d^8[4s] + e\text{-} \quad [E_{kin} = h\nu(3p^5 3d^{10}) - E_{sat}(3p^6 3d^8)], \qquad (4.3)$$

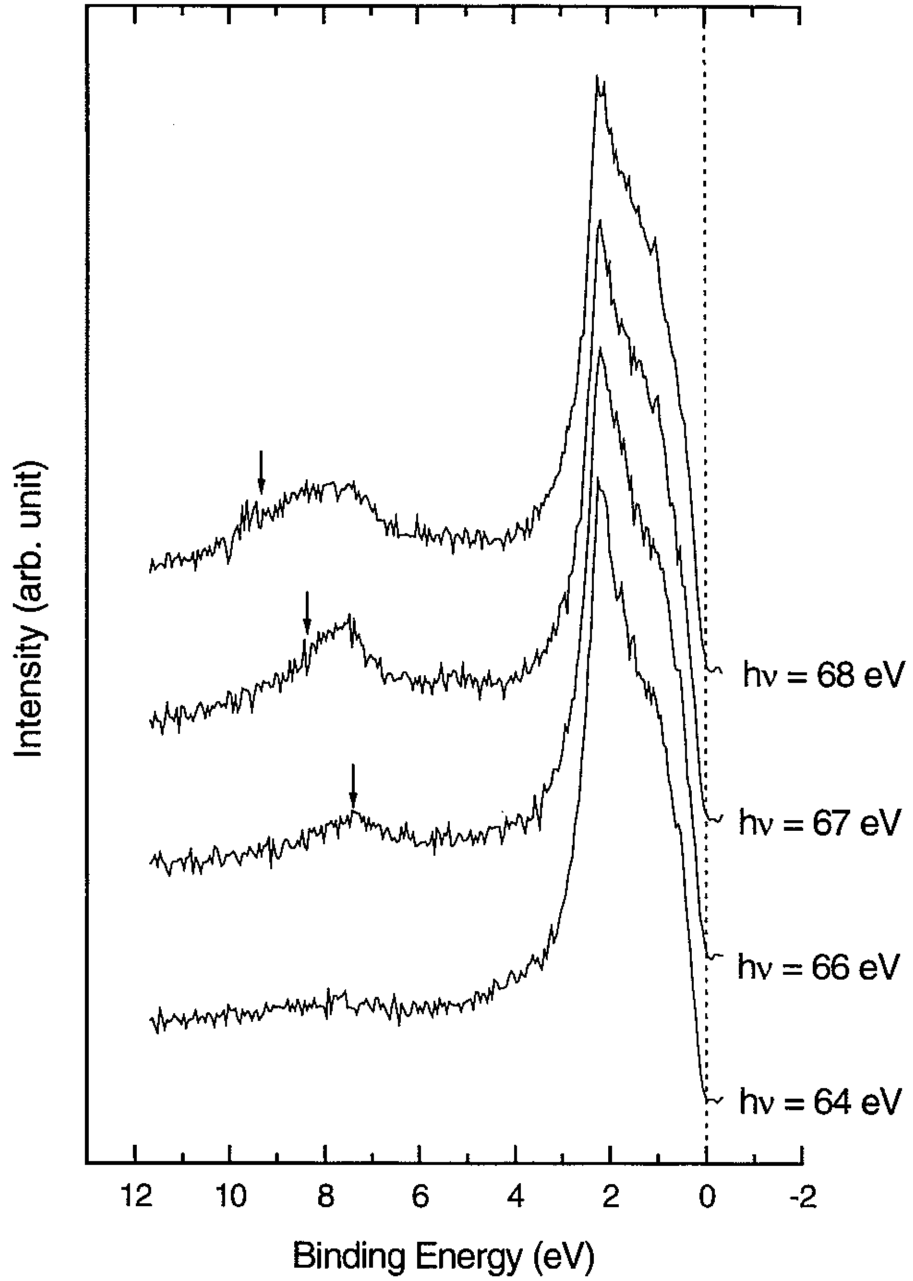

FIG. 4.3 EDCs of $EuNi_2Ge_2$ taken at varying photon energies (around the Ni 3*p* core level binding energy) in an attempt to observe resonance of the Ni 3*d* satellite. The Ni 3*p*→3*d* core-absorption threshold is ~ 66 eV. The vertical arrows indicate the expected location of the $M_{23}VV$ Auger peak as it moves through the valence band.

([4*s*] is a 4*s* screening electron) which is the Ni 6 eV satellite. In addition, the photon energy at the 3*p* resonance can excite an electron out of the 3*p* shell into the 3*d* hole just above E_F. The excited state resulting from this process can decay by an Auger process. This leads to the same final state (3*d*[4*s*]) and gives electrons with the same kinetic energy as direct photoemission leading to the satellite's final state

$$3p^6 3d^9 + h\nu \rightarrow 3p^5 3d^{10} \rightarrow 3p^6 3d^8[4s] + e\text{-} \quad [E_{kin} = E(3d^5 3d^{10}) - E_{sat}(3p^6 3d^8)]. \qquad (4.4)$$

The two processes overlap coherently at the threshold energy, giving rise to the resonant enhancement of the satellite [59]. Similarly as in Ni metal, the main peak around 1.4 eV binding energy (BE) and the satellite peak around 7.4 eV (6 eV below the main peak) in the hν ~ 66 eV spectrum can be roughly assigned to the $3d^9 4s$ and $3d^8 4s^2$ final states in atomic notation, respectively, by assuming an initial-state configuration of $3d^9 4s$, where 4*s* denotes a conduction electron [60, 61]. Due to a high density of states at E_F in Ni, the emission of a photoelectron can cause the excitation of a second electron into these unoccupied states at E_F, leaving a two-hole final state behind [62]. This two-hole configuration is not the ground state. A hole created in the photoemission from the Ni 3*d* band interacts with the holes that are present in this partially filled band. It is an excited state and the excitation energy is roughly 6 eV, in agreement with the experimental results. Because of the near–atomic character of the *d* states, the intra-atomic Coulomb repulsion between two *d* electrons (or holes) is large. Therefore, if the created hole and the hole that is already present in the ground state are located at the same lattice site, the solid is in a state of higher energy than if these *d* holes were on different sites. The Coulomb repulsive energy of the two holes raises the system energy, thereby lowering the photoelectron kinetic energy, giving a peak in the EDC below the bottom of the Ni 3*d* band, since the overall energy is conserved in the photoemission process [63, 64]. In summary, it can be said that the main line near E_F is from the "well-screened" final state with the 3*d* hole filled by a valence electron, and the satellite line is from the "poorly screened" final state, with valence electron (4*s*) partially screening the hole.

This assignment of the satellite is based on the observation that the Ni 3*d* satellite emission is resonantly enhanced at $h\nu = 66$ eV in Ni $3p \rightarrow 3d$ RPES. The satellite structure associated with the Ni 3*d* bands is not explained by one-electron band theory. Its importance increases with the size of intra-atomic correlation between the valence electrons, which reflects the non-negligible on-site Coulomb interaction between the Ni 3*d* electrons in $EuNi_2Ge_2$. The vertical arrows in Fig. 4.3 indicate the expected location of the $M_{23}VV$ Auger peak due to ejection of a valence electron into the vacuum and simultaneous de-excitation of a valence electron to the M_{23} atomic shell (an Auger transition is commonly expressed a spectroscopic notation including three terms, describing the subshell of the initial core hole and the two subshells of the holes in the doubly ionized final state. When valence bands are participating, the symbol V is used) as it moves through the valence band. At higher photon energy the $M_{23}VV$ Auger electrons move away from the satellite because they appear with fixed kinetic energy [$E_{3p} - E_{sat}$ (valence)] while the kinetic energy of the photoelectrons increases with $h\nu$.

To investigate more the contribution of electron states possessing significant Ni 3*d* character to the valence band of $EuNi_2Ge_2$, CIS spectra were recorded at selected initial-state binding energies across the excitation energy range of the Ni 3*p* threshold. In constant initial state (CIS) the photon energy and electron kinetic energy vary synchronously such that $h\nu -$

E_{kin} remains constant. This allows the photon-energy-dependent photoemission intensity of initial states to be investigated. Figure 4.4 shows constant initial-state spectra through the valence band with the photon energy passing through the Ni $3p \rightarrow 3d$ threshold and the corresponding initial-state binding energies are indicated alongside each curve and the inset. The scans at 0.19 eV, 0.69 eV, and 1.44 eV indicate the expected line shape of the anti-resonance (a weak dip in the intensity), occurring in the Ni $3d$ main line due to a reduction in the number of photons available for the direct photoemission (an appreciable number of them are absorbed at resonance by the $3p \rightarrow 3d$ excitation) [59]. We can also see clearly intensity enhancement in the satellite near 7.19 eV binding energy (BE). The scans indicate a resonance due to Ni $3p \rightarrow 3d$ transitions, thus showing that Ni $3d$ character is present in the valence band. The relative size of the enhancement at 0.19 eV BE suggests that there is much less Ni $3d$ character here than elsewhere in the valence band. We thus conclude that there is apparent strong Ni d character throughout the valence band.

Figure 4.5 presents a 37 eV wide EDC both on (a) and off (b) resonance for the Eu $4f$ levels in $EuNi_2Ge_2$. The scans were taken with photon energies of (a) 140 eV, and (b) 131 eV, with the Eu $4d \rightarrow 4f$ core-absorption threshold at $h\nu = 140$ eV. The intense Eu $4f$ states are located about 2 eV below E_F. Therefore we can immediately notice the strong enhancement of the Eu $4f$ peak at a BE of 2 eV. The ground-state term of Eu $4f^7$ is ${}^8S_{7/2}$. The $4f$ states are strongly localized and therefore very sharp in energy. The reason that they appear about 1 eV wide is that the $4f^6$ state left behind is of the type ${}^7F_J$ with $J = 0, 1, 2, 3, 4, 5, 6$ covering an energy range of about 1 eV [65, 66]. The separation of these levels is not large enough to be resolved in the spectra. The measured Eu $4f$ state was identical to those of calculated [67] and

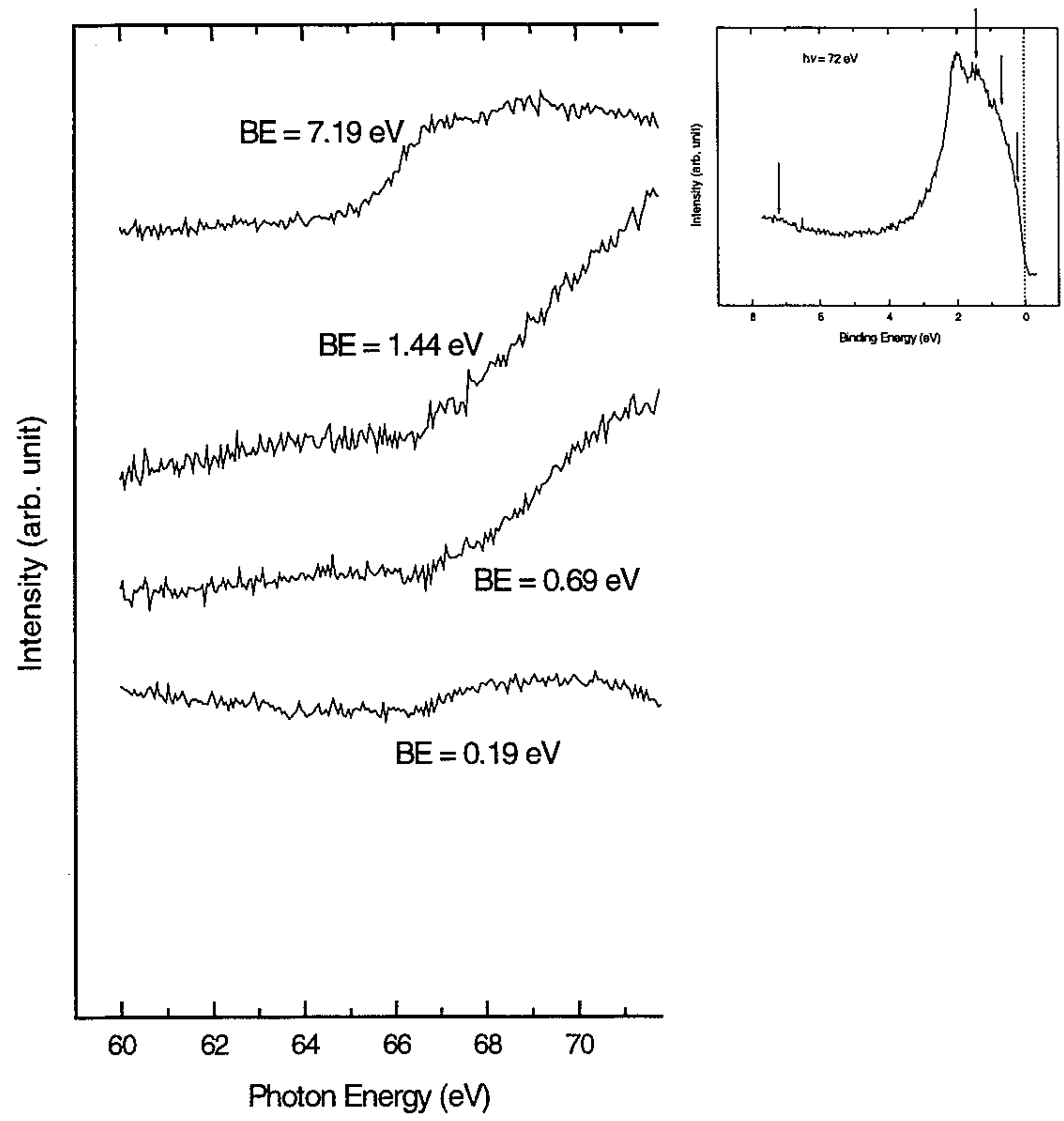

FIG. 4.4 Constant initial energy (CIS) spectra of $EuNi_2Ge_2$ taken at different binding energies throughout the valence band and the corresponding initial-state binding energies are indicated alongside each curve.
Inset: initial-state binding energies where CIS spectra are taken.

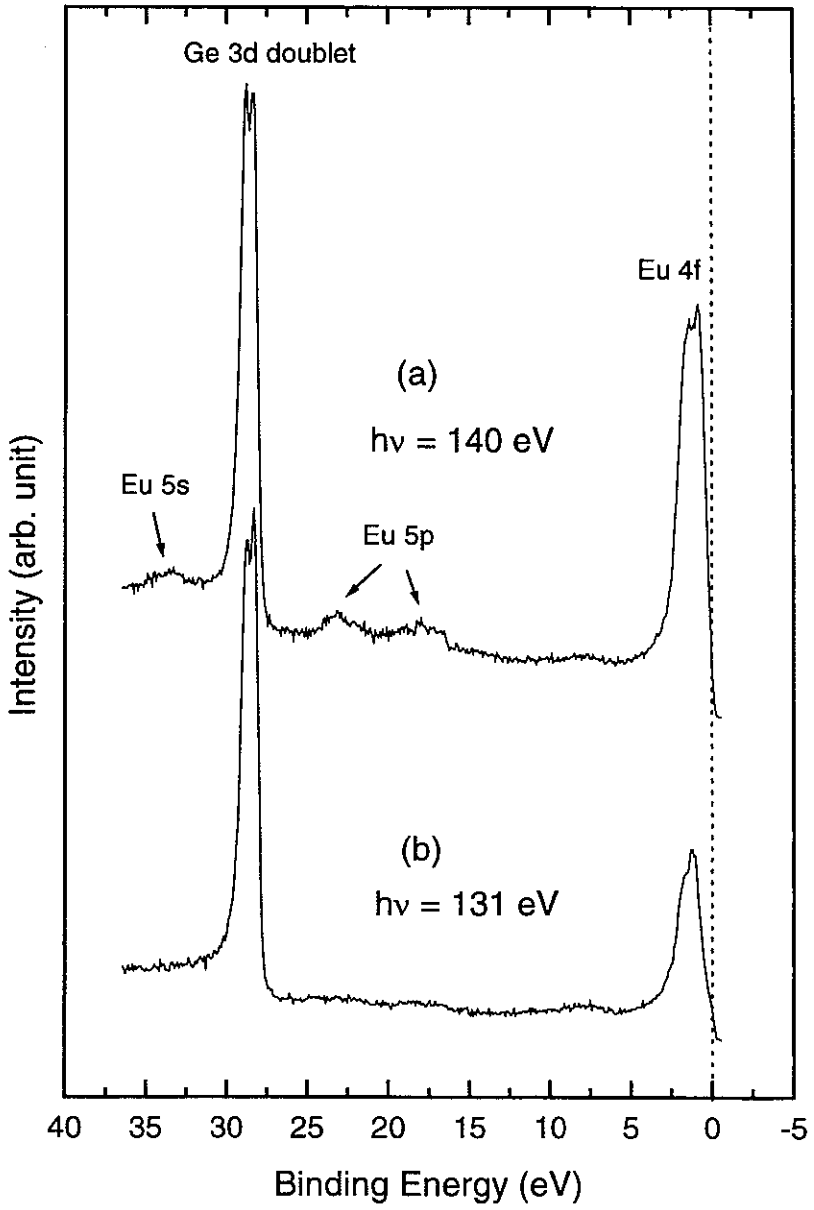

FIG. 4.5 A 37 eV wide EDC both on (a) and off (b) resonance for the Eu 4*f* levels in $EuNi_2Ge_2$. The scans were taken with photon energies of a) 140 eV, and b) 131 eV, with the Eu 4*d*→4*f* core-absorption threshold at *hν* = 140 eV. The arrows in (a) also indicate the enhancement of the Eu 5*p* and Eu 5*s* orbitals.

measured [68] photoemission spectra of Eu metal. The absolute position of the 4*f* levels in the photoemission spectrum or, more conveniently, the energy separation of the 4*f* state from E_F, called the 4*f* promotion energy, can be directly deduced from Fig. 4.5. In other words, it is the energy required to promote a 4*f* electron into a *d*-state at E_F [69]. We note it is almost identical to the calculated 4*f* promotion energy for Eu metal (1.9 eV) [70]. One can also see that the peak is not isolated from the valence band but located quite close to E_F, due to the fact that europium acquires a half-filled 4*f* shell through transfer of its 5*d* electron into the 4*f* shell [71]. The resonance effect shown in Fig. 4.5 is strong enough that we can see other enhancements as well (marked by arrows). The broad Eu 5*p* levels which are caused by spin-orbit interaction and the coupling of the open 5*p* and 4*f* shells can be seen at BE = 18.1 eV and 23.1 eV. Also enhanced is the Eu 5*s* band at a BE of 33.5 eV [72, 73]. Calculations [11] corroborate this observation, as the bands near this energy are of Eu 5*s* character. Lastly noted in Fig. 4.5 are the split Ge 3*d* core levels. This splitting arises from the spin-orbit coupling effect in the final state, with spin-up and spin-down as possible as spin directions ($J = L \pm 1/2$ in LS-coupling). The inner 3*d* core levels are completely full but the removal of an electron by a photon leads to a $3d^9$ configuration in the final state, causing coupling between the unpaired spin and orbital angular momenta. The $3d_{3/2}$ and $3d_{5/2}$ peaks are located at BEs of 28.9 eV and 28.3 eV respectively. Therefore the dominating spectral weight around 2 eV in $EuNi_2Ge_2$ reflects the substantial hybridization between Eu 4*f* and Ni 3*d* orbitals. It is known for Eu compounds that the $4f^7 \rightarrow 4f^6$ spectral weight (divalent contribution) exists in the energy region 0-2 eV below E_F, and the $4f^6 \rightarrow 4f^5$ spectral weight (trivalent contribution) exists at 3-12 eV below E_F [74]. It can be explained as follows: The higher valence state has one fewer 4*f* electron and the screening of the nuclear charge is consequently weaker, and the core-level binding energies increase [70]. We note in Fig. 4.5 that for $EuNi_2Ge_2$ only multiplets from the divalent f^6 electron configuration (0-2 eV) appear, which confirms a valence of 2+ for Eu ions in $EuNi_2Ge_2$. Resonance enhancement is usually described as a direct recombination of the excited state resulting from a process such as

$$4d^{10}5s^25p^64f^7\mathrm{V} \rightarrow 4d^95s^25p^64f^8\mathrm{V} \rightarrow 4d^{10}5s^25p^64f^6\mathrm{V} + e^-, \tag{4.5}$$

where V stands for the valence band 5*d*- and 6*s* electrons. Electron excitation to $4d^94f^8$ states given above interferes with direct photoemission from the 4*f* shell. Apart from this process the energy from the direct recombination may be transferred to electrons from the outer shells resulting in various single hole final states according to the scheme

$$4d^95s^25p^64f^8\mathrm{V} \rightarrow 4d^{10}5s5p^64f^7\mathrm{V} + e^- \tag{4.6}$$

$$\rightarrow 4d^{10}5s^25p^54f^7\mathrm{V} + e^-. \tag{4.7}$$

The two final states are, respectively, 5*s* and 5*p* photoemission, and these processes are related to the resonant enhancement of the 5*s* and 5*p* [67, 75].

Figure 4.6 represents a 40 eV wide EDC both on (a) and (b) off resonance for the Gd 4*f* levels in $GdNi_2Ge_2$. The scans were taken with photon energies of (a) 149 eV and (b) 135 eV, with the Gd 4*d*→4*f* core-absorption threshold at $h\nu = 149$ eV. The intense Gd 4*f* states are located about 8.4 eV below E_F which shows the strong enhancement of the Gd 4*f* peak with a resonance photon energy of 149 eV. It shows that the Gd 4*f* levels of $GdNi_2Ge_2$ are more tightly bound by 6.4 eV than the Eu 4*f* levels of $EuNi_2Ge_2$, indicating that the Gd 4*f* shell in $GdNi_2Ge_2$ is more stable, although Eu and Gd have isoelectronic 4*f* shells [76]. The

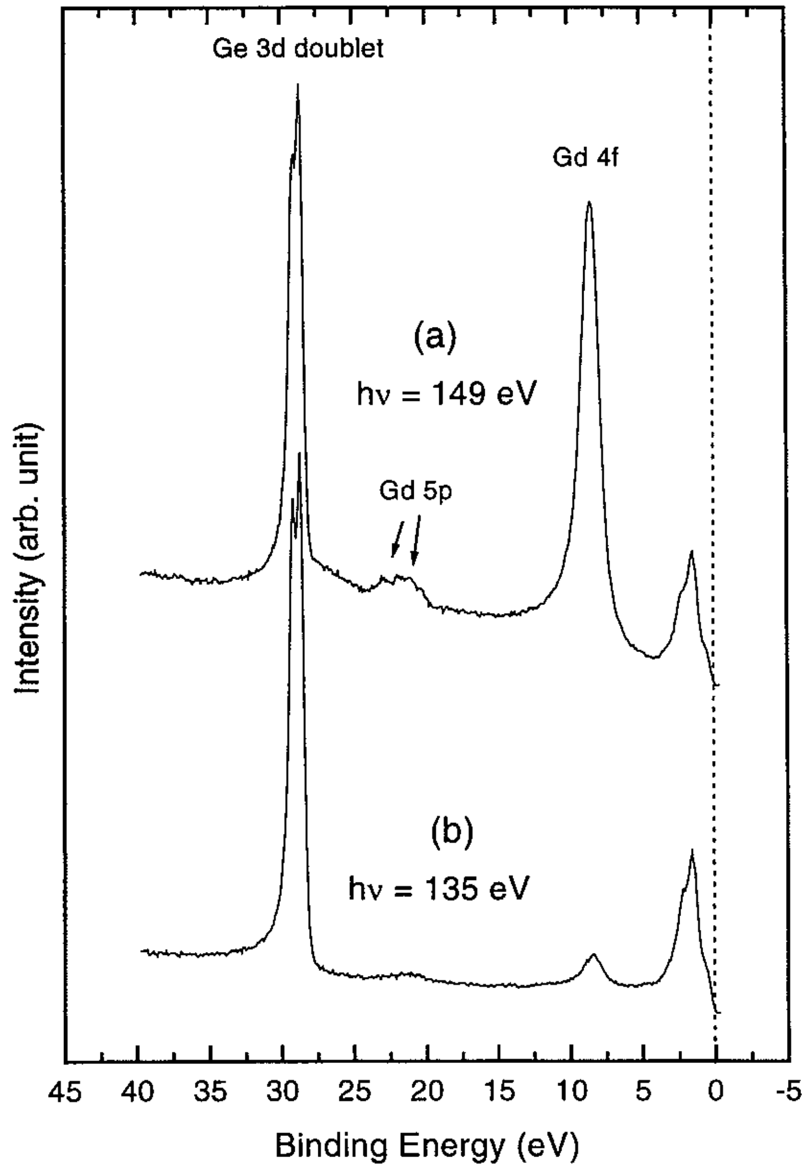

FIG. 4.6 A 40 eV wide EDC both on (a) and (b) off resonance for the Gd 4*f* levels in $GdNi_2Ge_2$. The scans were taken with photon energies of a) 135 eV and b) 149 eV, with the Gd $4d \rightarrow 4f$ core-absorption threshold at $h\nu = 149$ eV. The arrows in (a) also indicate the enhancement of the Gd 5*p*.

Ge 3*d* doublet is also seen around 29 eV BE. The broad Gd 5*p* levels can be seen at BE = 20 eV ~ 25.0 eV as well [72, 77]. Figure 4.7 represents the subtraction procedure for the Eu 4*d*→4*f* off-resonance spectrum (middle) from the on-resonance spectrum (top) and the difference curve (bottom). The enhanced features at $h\nu = 141$ eV, as compared to $h\nu = 131$ eV, are clearly observed in the difference curve, which is considered to represent the extracted Eu 4*f* partial spectral weight (PSW). In the extraction of the Eu 4*f* PSW distribution, we have ignored the $h\nu$ dependence of the emission from non-4*f* valence band electrons (Ni 3*d*). The Eu 4*f* PSW shows a pronounced peak around 0.8 eV and a shoulder around 1.4 eV. Resonance photoemission has been extensively utilized for extracting the partial density of states, such as the 3*d* state in transition-metal compounds and the 4*f* and 5*f* states in lanthanide and actinide compounds. This resonant enhancement is caused by an indirect process, which has the same initial and final states as a direct photoemission process, associated with the Coster-Kronig or the super Coster-Kronig decay of the intermediate state reached by the photoabsorption. For instance, the 4*f* photoemission is resonantly enhanced at the 4*d*→4*f* photoexcitation due to the indirect process associated with the super Coster-Kronig decay

$$4d^{10}4f^{7} + h\nu \rightarrow 4d^{9}4f^{8} \rightarrow 4d^{10}4f^{6} + e^{-}, \tag{4.8}$$

where $h\nu$ and e^{-} stand for an incident photon and ejected photoelectron, respectively. The 4*f* partial density of states can be obtained by subtracting an off-resonance spectrum from an on-resonance spectrum.

Eu has the $4f^{7}$ initial configuration and the final states for the excited $4f^{6}$ configuration are ${}^{7}F_{J}$ ($J = 0,1,\ldots 6$) i.e. seven possible states. The solid curve in the EDC-spectrum is the result

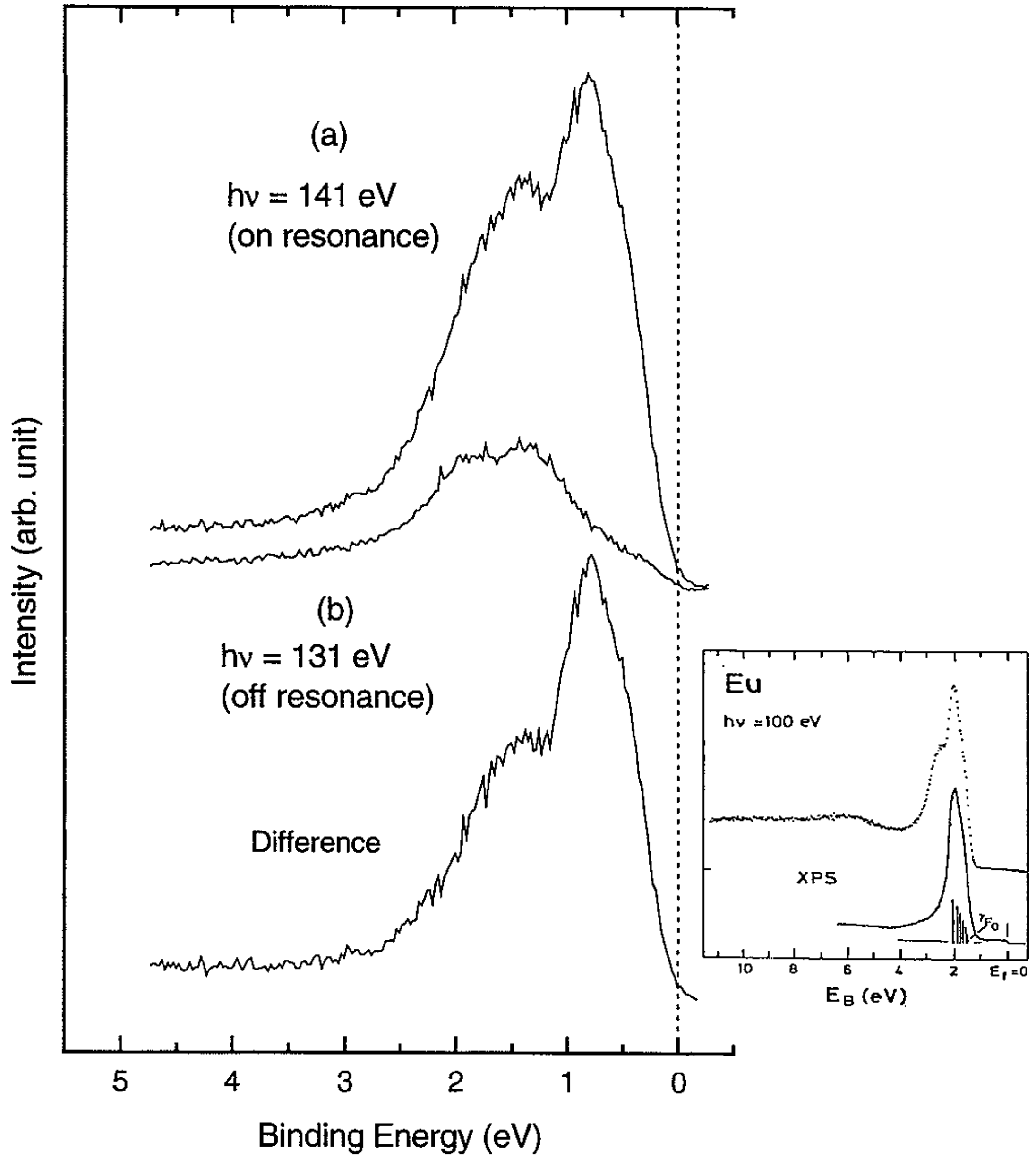

FIG. 4.7 EDCs both on(a) and (b) off resonance for the Eu $4f$ levels in $EuNi_2Ge_2$ and the difference curve (bottom). The scans were taken with photon energies of a) 141 eV and b) 131 eV, with the Eu $4d \rightarrow 4f$ core-absorption threshold around $h\nu = 140$ eV. Inset : Comparison between XPS-spectra (Al K_α, 1486.6 eV) and 100 eV photon energy spectra for the $4f$ emission region of Eu (after [79]).

of adding these seven 4*f* lines, each of which has been convoluted with a Doniach-Sunjic line shape to account for core-level lifetimes and screening by conduction electrons [78] and the sum has been resolution broadened. In the XPS-spectrum (Al K_α, 1486.6 eV) in Ref [79] there was only one peak at 2 eV binding energy, but in the 100 eV spectrum there is an extra shoulder on the high binding energy side which originates from the 4*f* electrons of the surface atoms. That is due to the fact that at the higher photon energy, the mean free path is increased and the surface contribution is correspondingly reduced. Likewise the shoulder around 1.4 eV in $EuNi_2Ge_2$ may be attributed to the intrinsic surface state. It is well known that surface atoms may undergo structural and/or electronic changes due to the missing neighbor atoms on the vacuum side [80, 81]. Due to lower coordination at the surface, a band narrowing and smaller valence-electron density is experienced. The surface contribution can be recognized by comparing data taken with two different photon energies. At the higher photon energy, the escape depth is increased and the surface contribution is correspondingly reduced. The surface core level shift for Eu 4*f* was 0.63 eV, by fitting the spectrum with two sets of ^7F_J states i.e. 14 states with the multiplet line intensities given within each set. Surprisingly the surface binding energy shift value of 0.63 eV in $EuNi_2Ge_2$ is almost same as that of the 4*f* state in Eu metal, which confirms again that the shoulder at 1.4 eV is from the surface state [82, 83].

Figure 4.8 illustrates resonant effects observed in $EuNi_2Ge_2$, in which the comparison between photoemission spectra for $EuNi_2Ge_2$ taken at photon energies of 70 eV (Ni 3*p* on resonance), and prior to the resonance at 65 eV near the Ni 3*p* core edge, is shown. Throughout the energy range employed here, the structure in the photoemission spectra is representative of the Ni contributions in the electronic structure. Intensity due to (Ge, Eu 6*s*

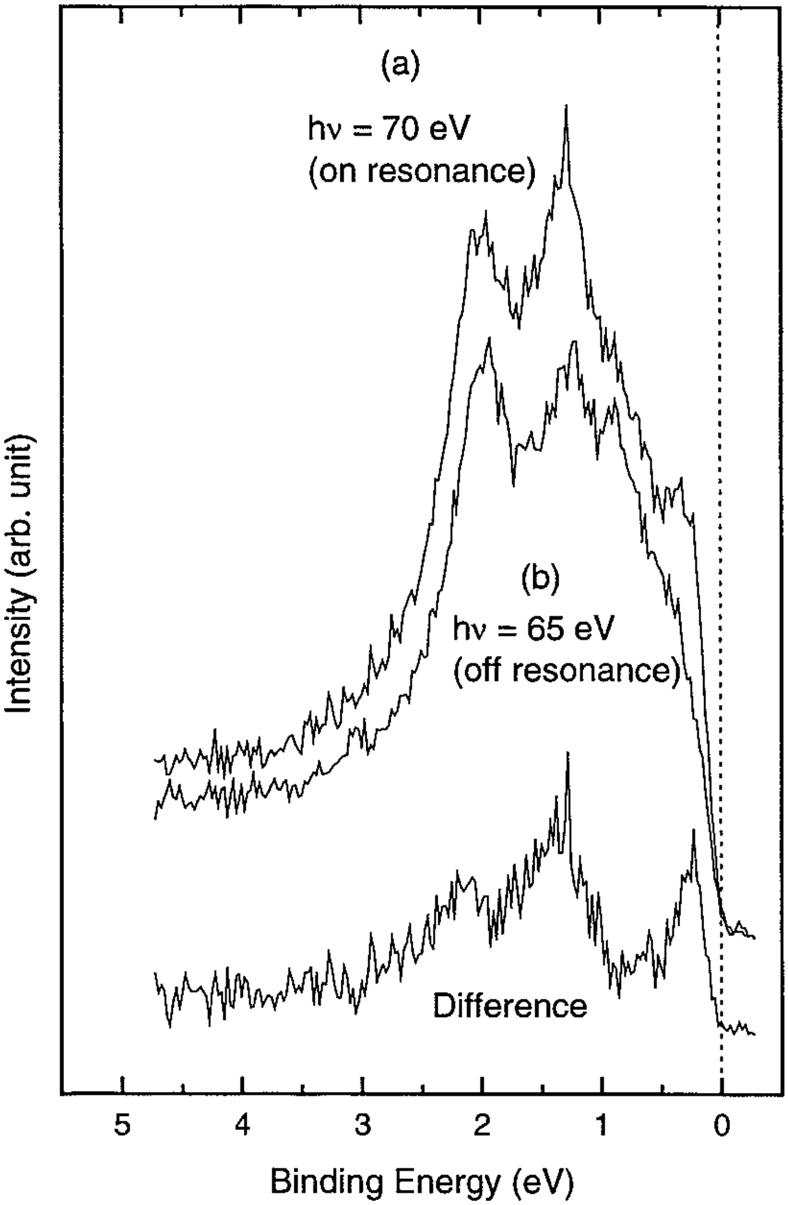

FIG. 4.8 The EDCs for $EuNi_2Ge_2$ with photon energies of (a) 70 eV (on resonance) and (b) 65 eV (off resonance) for the Ni 3*d* levels and the difference curve (bottom).

etc.) is at least one order of magnitude lower, due to decreased cross section and lower density of states. The enhanced features at 0.2 eV, 1.4 eV, and 2.2 eV are clearly observed from the difference curve which is considered to represent the Ni 3*d* partial spectral weight distribution. The binding energy (BE) 1.4 eV peak was also observed, exhibiting stronger resonant enhancement for 72 eV photon excitation in Fig. 4.1. The splitting between the two main features in the difference spectrum arises due to crystal-field splitting, so that the peak at approximately 1.4 eV is predominantly of e_g character. The peak closer E_F is produced by Ni 3*d* states that are predominantly t_{2g} character.

To compare with the experimental PSW below E_F, the calculated partial density of states (DOS) is included in Fig. 4.9 from the tight-binding linear muffin-tin-orbital (TB-LMTO) calculations developed by the group of Refs [12, 13, 14]. A good review of the energy band structure and magnetic ordering of rare earth metals can be found in Ref [84]. Our measurement compares very well with the calculation. Most of the Ni 3*d* DOS is located from E_F to 4 eV BE. The calculated Ni 3*d* DOS [85] exhibits four sharp, well-separated peaks, which correspond the experimental Ni 3*d* strong peaks at 2.2 eV, 1.4 eV, and 0.2 eV BEs quite well. But we note that a direct comparison of intensities is not possible, as the PSW does not represent the DOS, since we scan only in the normal direction, sampling a small part of the BZ. A little more discrepancy between experiment and theory may be partially due to the effects of photoionization matrix element, Coulomb correlation energy, a finite lifetime broadening of electron and hole state, relaxation and screening in photoemission process, and self energy of hole (except near E_F) which are not included in the theoretical calculations.

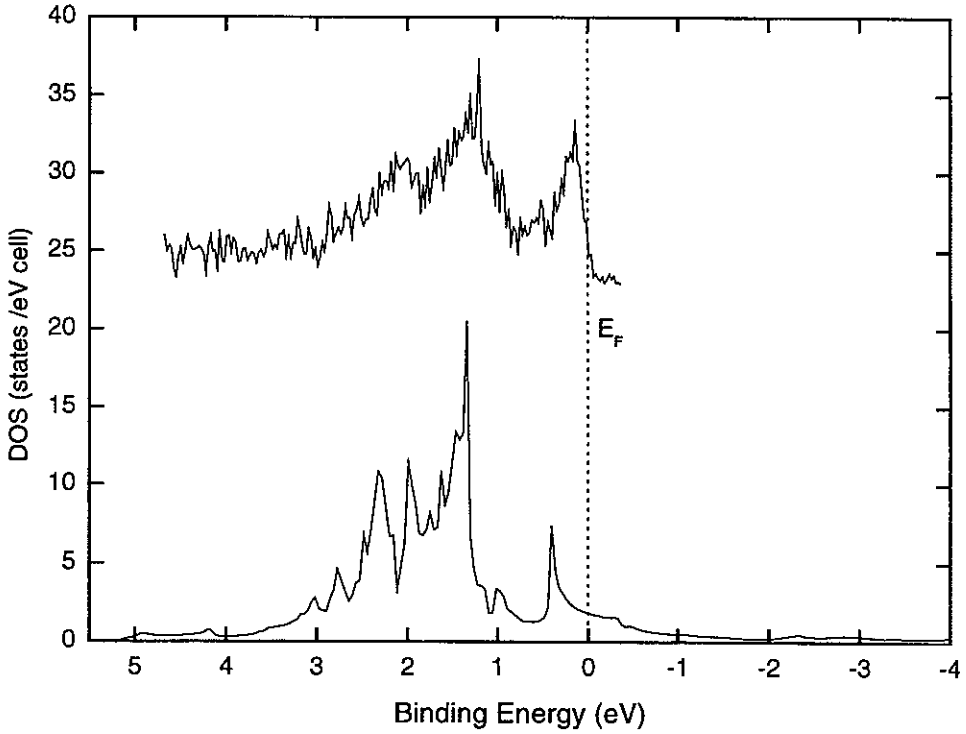

FIG. 4.9 Comparison of the Ni 3*d* partial spectral weight (top) with the calculated Ni 3*d* partial density of states (bottom) in $EuNi_2Ge_2$ from Ref [85].

Figure 4.10 shows the EDCs for $GdNi_2Ge_2$ with photon energies of 70 eV and 65 eV, corresponding to the on-and off-resonance energies due to the Ni $3p \rightarrow 3d$ absorption, respectively. The difference curve represents the Ni 3*d* partial spectral weight (PSW) distribution which has enhanced features at 0.3 eV, 1.4 eV, and 2.3 eV. This Ni 3*d* PSW is compared with the calculated Ni 3*d* density of states (DOS) [85] in Fig. 4.11 which exhibits five sharp, well-separated peaks in the Ni 3d DOS, three of which correspond quite well to the observed Ni 3*d* strong peaks at 0.3 eV, 1.4 eV, and 2.3 eV BEs.

Figure 4.12 shows a constant-final-state (CFS) scan for $EuNi_2Ge_2$ taken at the Eu 4*f* peak with a kinetic energy E_{kin} of 3 eV, with the inset showing the photoabsorption cross section of Eu metal around the $4d \rightarrow 4f$ resonance obtained by measuring the yield of secondaries or inelastic photoelectrons (CFS spectrum at 5 eV kinetic energy) [86] which have experienced at least one inelastic collision before leaving the solid. We have also measured CFS spectra, where the electron analyzer is fixed at a constant final energy E_{kin} while the photon energy is varied. The CFS spectra, when taken of low kinetic energy photoelectrons (in our case 3 eV), where the secondary emission dominates the spectrum, correspond to the measured optical absorption spectrum [87, 88, 89].

The dominant contribution to the absorption spectrum in the energy range of the $4d \rightarrow 4f$ giant resonance comes from the Eu 4*f* states. What photoemission experiments probe is, by their very nature, not the initial-state energy, but the spectrum of the energy difference between the ground state and the numerous final, ionized states. If an ion has an incomplete outer shell, the hole created through photoionization can couple to the spin and orbital angular momentum of the incomplete shell and thereby produce a structure not necessarily present in the initial state. The multiplet splittings are largest when all of the interacting states

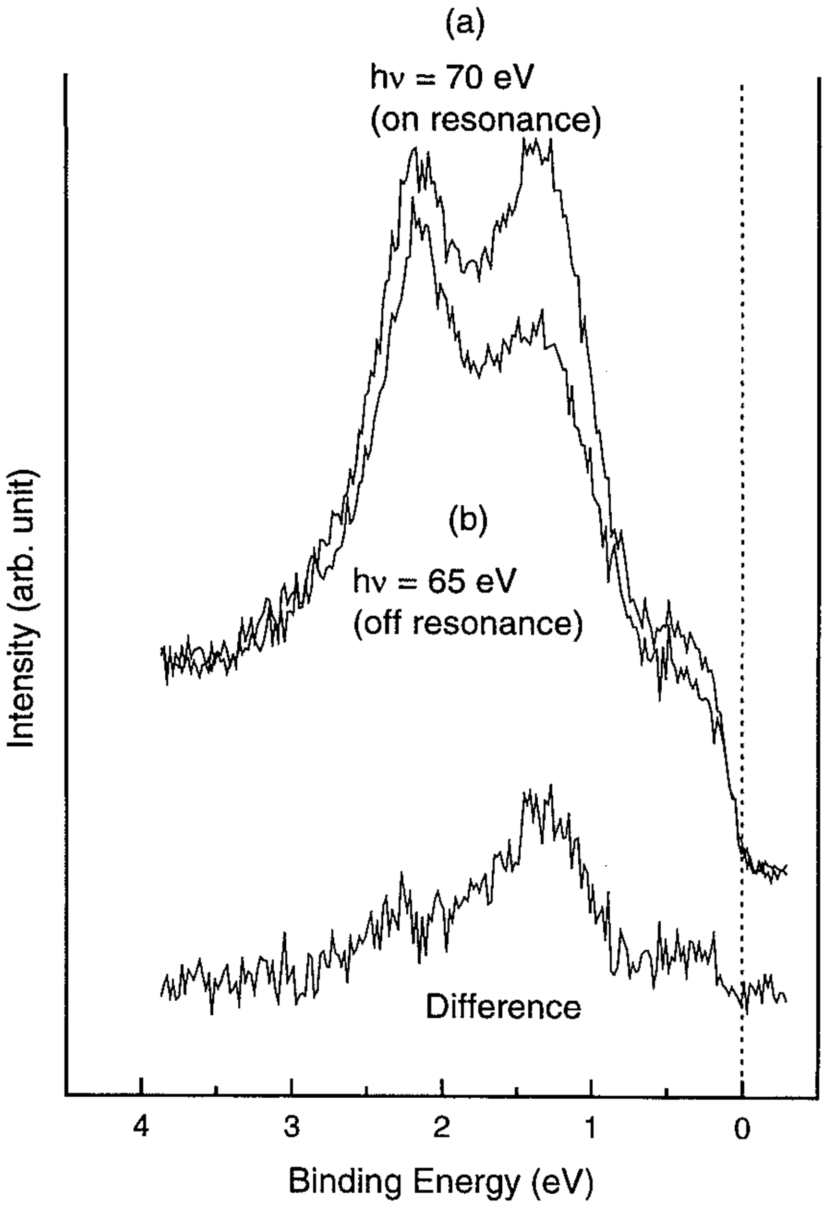

FIG. 4.10 The EDCs for $GdNi_2Ge_2$ with photon energies of (a) 70 eV (on resonance) and (b) 65 eV (off resonance) for the Ni 3*d* levels and the difference curve (bottom).

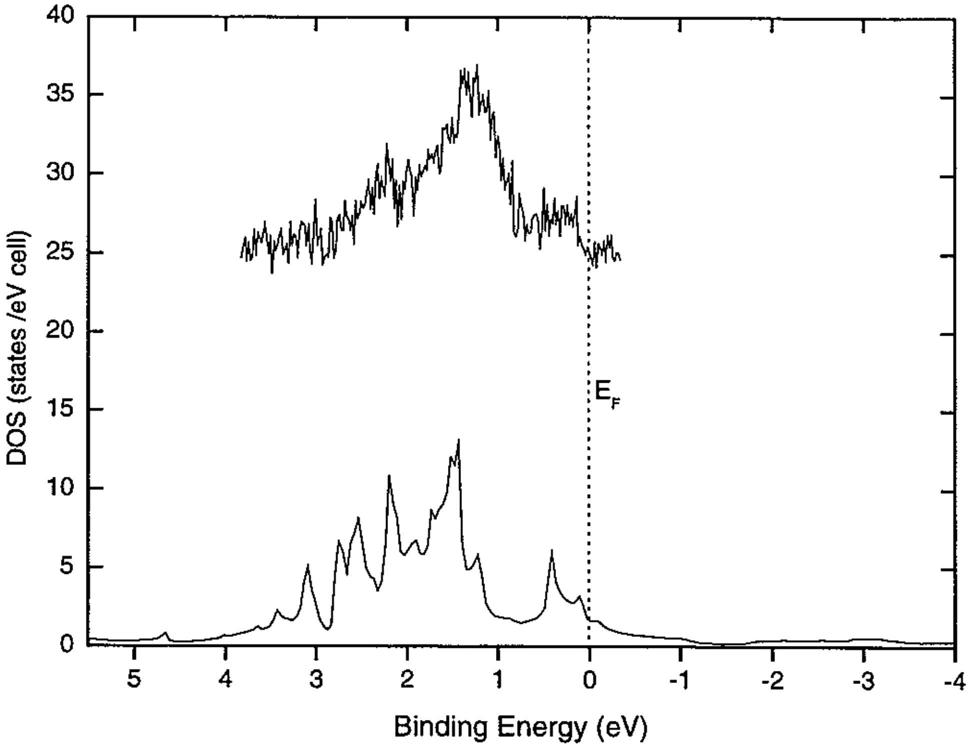

FIG. 4.11 Comparison of the Ni 3*d* partial spectral weight (top) with the calculated Ni 3*d* partial density of states (bottom) in $GdNi_2Ge_2$ from Ref [85].

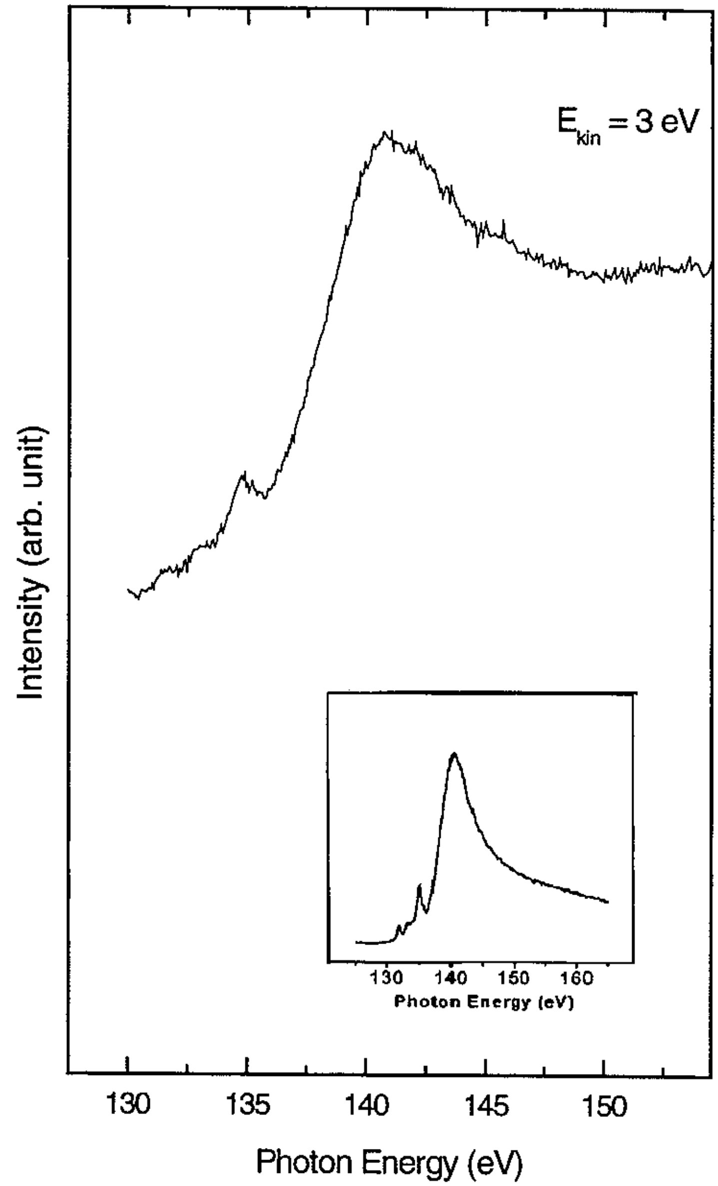

FIG. 4.12 The 130-160 eV region for $EuNi_2Ge_2$ was scanned in the partial yield mode to give an absorption spectrum. The 4*d*→4*f* excitation spectrum is characteristic of the number of 4*f* electrons because of large multiplet fine structure in the prethreshold region. The inset shows the photoabsorption cross section of Eu metal around the 4*d*→4*f* resonance (after [86]).

are within a shell with a given principal quantum number, because the Coulomb and exchange integrals are then largest. This condition also leads to the most complex spectra, because all of the different configurations with same symmetry, which can be obtained by rearranging the available number of electrons within the shell, must be considered [90]. The CFS partial yield spectrum was taken with a kinetic energy E_{kin} of 3 eV, corresponding to an electron escape depth of order of a few tens of Å. Thus the spectral features in the partial-yield spectra can be regarded as representing the intrinsic bulk spectrum of the material [91]. The CFS yield spectrum of $EuNi_2Ge_2$ exhibits fine structure below the absorption threshold around 131 – 137 eV and broad giant resonance above the absorption threshold around 140 – 150 eV. At a photon energy of $h\nu = 140$ eV, which is near the $4d^{10}4f^7 \rightarrow 4d^9 4f^8$ optical transition energy, this gives rise to the giant $4f^7 \rightarrow 4f^6$ resonance due to the well- known process

$$4d^{10}4f^7 + h\nu \rightarrow 4d^9 4f^8 \rightarrow 4d^{10}4f^6 + e^- \qquad (4.9)$$

where the ground state configuration $4d^{10}4f^7$ of the Eu ion consists of a filled $4d$ core level and 7 electrons occupying the spin-orbit and multiplet split $4f$ level.

Both the fine structure and the giant resonance in the 4d→4f absorption can be regarded as consisting of transitions from the ground level of a $4d^{10}4f^7$ configuration to the final-state multiplet structures with the numerous levels of the $4d^9 4f^8$ configuration due to the strong Coulomb and exchange interaction between $4d$ hole and unfilled $4f^8$ shell [92, 93, 94] which splits the $4d^9 4f^8$ levels by ~20 eV (spread over a very broad range), pushing some levels well above threshold. The energy separations and relative strengths among the fine structures in the optical absorption spectra of rare-earth compounds represent the valence state of the rare-earth ions [89, 95, 96]. The exchange splitting of the excited $4d^9 4f^8$ states is large because the $4d$ and $4f$ radial wave functions overlap well, resulting in rich multiplet features in the region of the $4d$ core energy. The number of multiplet structures and their relative energies are particularly sensitive to changes in either the $4f$ number or the $4f$ radial wave functions [88]. Therefore the $4d \rightarrow 4f$ excitation spectrum is characteristic of the number of $4f$ electrons because of this large multiplet structure. The $4d \rightarrow 4f$ excitation spectrum is very sensitive to the number of $4f$ electrons due to a large $4d \rightarrow 4f$ exchange and Coulomb interaction.

We compare the fine structures of $EuNi_2Ge_2$ to that of Eu metal in the inset [86] in Fig. 4.12. Here Eu metal is chosen because it is a well-known divalent metal, with the $4f^7$ electron configuration in the ground state [97]. The $4f$ shells in rare earth metals are spatially deeply buried although they energetically lie in the valence band and are assumed to have no appreciable itinerancy (very small overlap with orbitals on adjacent atoms). Therefore, the magnetic moment related to them is highly localized. As free atoms are condensed into a rare earth metal, only their outer electrons ($5d$ and $6s$ electrons) are promoted into the conduction band. Unlike most of the rare earth metals, in the metallic state Eu becomes divalent with a $4f^7$, rather than trivalent with $4f^6$, because of the high stability of the half-filled $4f$ shell. Here we note excellent agreement with the CFS spectra for Eu metal, having the main absorption maximum around 140 eV, and smaller absorption maxima at 131.5 eV, 132.9 eV, and 134.7 eV photon energies [98, 99], which are similar to calculated ones [100]. This comparison clearly shows that the CFS fine structures of $EuNi_2Ge_2$ are very similar to those of Eu metal, indicating that we can interpret the Eu in $EuNi_2Ge_2$ to be essentially divalent. The corresponding spectrum from our $EuNi_2Ge_2$ samples was also very similar to the spectrum of

Gd metal (valence of 3+) and $GdNi_2Ge_2$, as shown in Fig. 4.13 where the Gd atom in the bulk metal is the same trivalent $4f^7$ as the free Gd atom, confirming again that the $EuNi_2Ge_2$ and $GdNi_2Ge_2$ had $4f^7$ initial configurations. In fact, the CFS of Eu and Gd metals are very similar to each other and to the calculated $3d^{10}4f^7 \rightarrow 3d^9 4f^8$ spectra because Eu and Gd are both distinguished by the stable $4f^7$ ($^8S_{7/2}$) state of the $4f$ shell except for the fact that the increased nuclear charge of Gd shifts all spectra towards higher photon energies [72, 99].

Divalent ($4f^7$) Eu occurs in some compounds, e.g., EuO and $EuMn_2Ge_2$ [101] and trivalent ($4f^6$) Eu compounds are Eu_2O_3, $EuCl_3$ [102], $EuPd_3$ [74], $EuAg_5$ [103], and $EuNi_2Si_2$ [7]. In the case of EuT_2X_2 (T = Transition metal, X = Ge, Si) the valence is probably determined by the nature of the first and second nearest neighbors, their spatial distribution, and distances from Eu ions [10, 104]. Especially divalent Eu ions are associated with the extraordinary large volume available for Eu atoms in the unit cell compared with the neighboring elements in the periodic table. Europium is primarily divalent at small atomic distance, while it becomes trivalent state with increasing atomic distance. In addition, $EuCu_2Si_2$ [105] has a mixed valent state interpreted by strong hybridization behavior and rapid fluctuation ($\tau < 3.5 \times 10^{-11}$ sec) of an electron between the localized $4f$ level and the conduction band, causing fluctuations between the divalent and trivalent Eu states.

To further investigate whether there is really any Eu $4f$ character in the valence band we took constant-initial-state (CIS) scans of the Eu $4f$ peak as shown in Fig. 4.14. The CIS spectrum represents the resonance-photoemission-cross-section line shape, determined by initial and final states [41]. The large resonance near the onset of the Eu $4d \rightarrow 4f$ absorption at

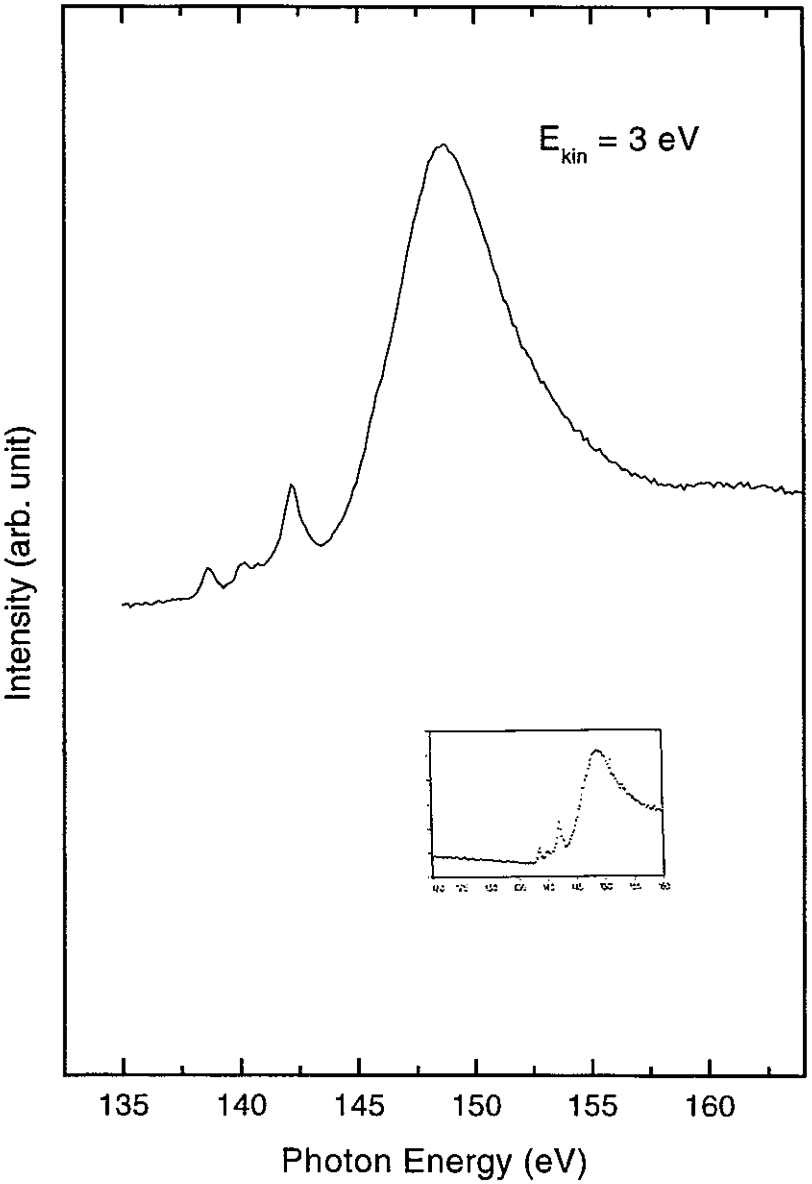

FIG. 4.13 The 135-168 eV region for $GdNi_2Ge_2$ was scanned in the partial yield mode to give an absorption spectrum. The $4d \rightarrow 4f$ excitation spectrum is characteristic of the number of $4f$ electrons because of large multiplet fine structure in the prethreshold region. The inset shows the photoabsorption cross section of Gd metal around the $4d \rightarrow 4f$ resonance (after [99]).

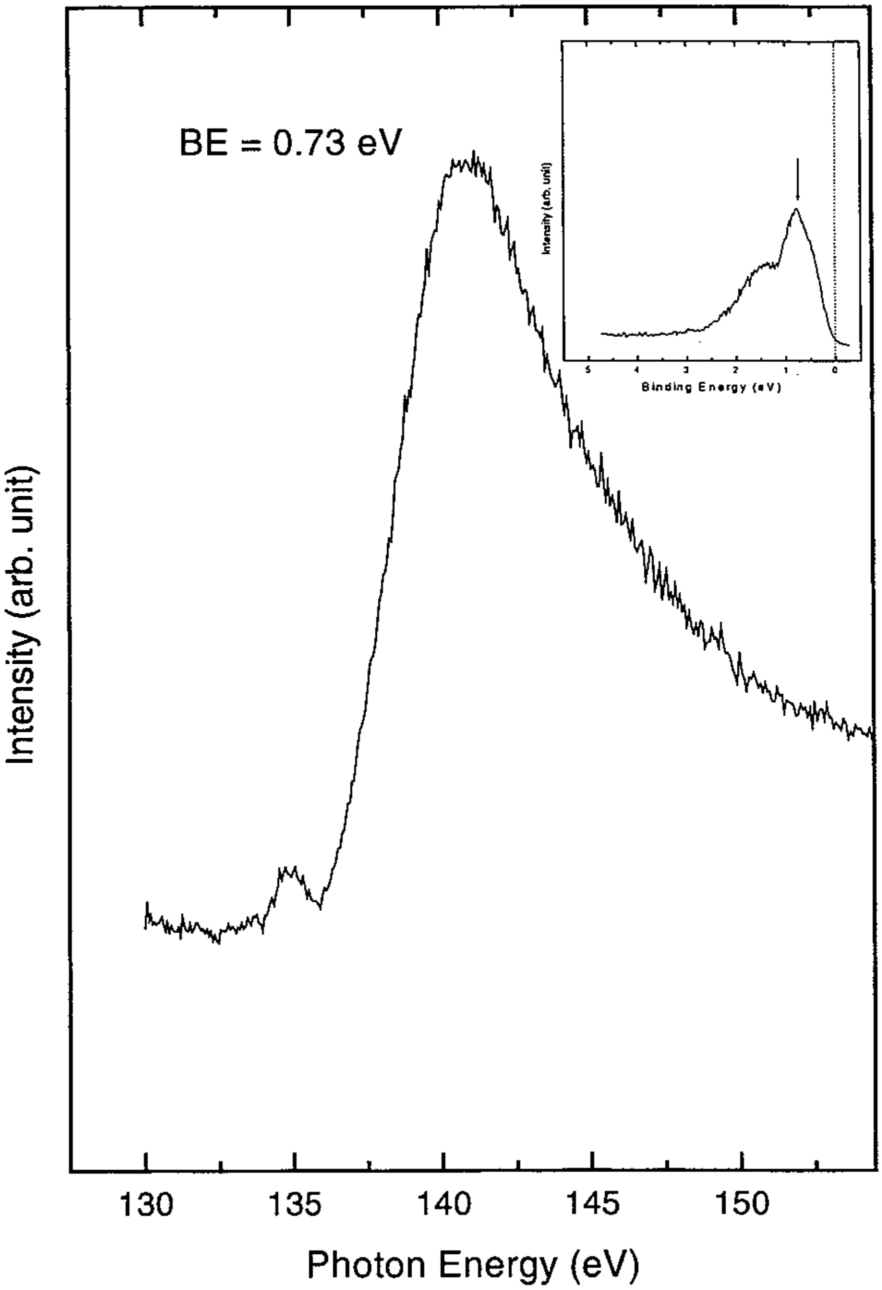

FIG. 4.14 CIS spectrum of $EuNi_2Ge_2$ near Eu 4*f* resonance at a binding energy of 0.73 eV. Inset: Eu 4*f* partial spectral weight obtained in Fig. 7 and initial-state binding energies where the CIS scan is taken.

a BE = 0.73 eV shows dominant Eu 4*f* character at a BE = 0.73 eV, which is consistent with the Eu 4*f* PSW in Fig. 4.7. A large enhancement around 140 eV represents the Eu 4*f* resonance via the Eu 4*d*→4*f* excitation and the following Auger process with the Coulomb matrix element. The CIS fine structure of $EuNi_2Ge_2$, just like the CFS partial yield spectrum in Fig. 4.12, exhibits fine structure below the absorption threshold around 131 – 137 eV and a broad giant resonance above the absorption threshold around 140 – 150 eV.

Energy band mapping of $EuNi_2Ge_2$ and $GdNi_2Ge_2$

In this study, we investigate the electronic band structure of $EuNi_2Ge_2$ and $GdNi_2Ge_2$ single crystals along the Γ to Z [001] direction in the bulk Brillouin zone (BZ) by taking normal-emission photoelectron spectra. The spectra in Fig. 4.15 are recorded with an angle-resolved analyzer positioned to collect the electrons emitted normal to the (001) surface of $EuNi_2Ge_2$. The intensity is recorded as a function of the energy of the emitted electrons for a wide range of photon energies ($h\nu$s), 14 eV $\leq h\nu \leq$ 58 eV, and the curves are then plotted as a function of binding energy measured from the Fermi energy (E_F).

There are several dispersive features in the valence band. In this geometry a shift in the binding energy (BE) of a peak as a function of photon energy represents dispersion with wave vector along the direction normal to the surface, the *a*-*b* plane. The four dispersing features are a feature around 1 eV (A), a weak feature around 1.5 eV (B), another feature around 2 eV (C), and a feature around 2.5 eV (D). The enhancements at smaller photon energies are manifestations of strong-selection-rule effects. Feature A exhibits significant energy dispersion with changing $h\nu$, which is consistent with the direct-transition model. It disperses over an energy range of nearly 0.38 eV, from its deepest value of 1.28 eV BE at $h\nu$ = 48 eV to its smallest value of 0.90 eV at $h\nu$ = 33 eV. One set of peaks, labeled C, appears at an almost fixed BE of around 2 eV, independent of the incident photon energy, which shows that any dispersion is small. This is expected from *d*-character bands, which dominate this region of the valence band. Feature D disperses as the photon energy is changed from 14 eV to 26 eV, clearly showing a BE shift between 2.6 and 2.8 eV.

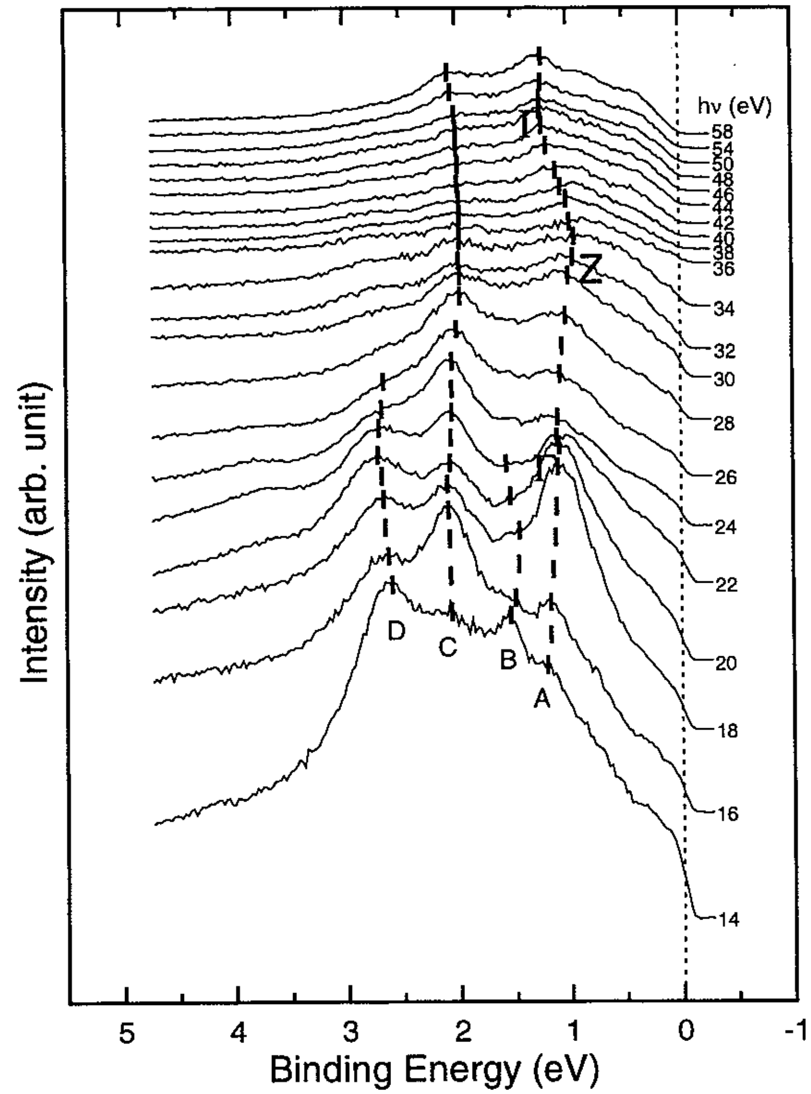

FIG. 4.15 EDCs for $EuNi_2Ge_2$ at normal emission from the (001) surface (Γ-Z direction) taken with increasing photon energy. Binding energies (BEs) are referenced to the Fermi level (E_F) and the spectra have been arbitrarily displaced along the ordinate for clarity. The vertical bars are a guide to the eye which qualitatively follow the major features of the scans.

At higher photon energies ($h\nu$ > 30 eV), we could find small dispersion for features B and D although the peak intensity is low. Dispersion might be masked by the very strong intensity modulations due to matrix element effects if the features are composite in nature.

Figure 4.16 presents the valence-band EDCs for $GdNi_2Ge_2$ at normal emission from the (001) surface (Γ-Z direction) in the photon energy range of 14 eV $\leq h\nu \leq$ 44 eV. There are three features which correspond to those of $EuNi_2Ge_2$, at around 1.2 eV (A), a feature around 2.2 eV (C), and another around 2.8eV (D) although feature B was not observed. It is notable that all features for $GdNi_2Ge_2$ are at about 0.25 eV lower BE than those of $EuNi_2Ge_2$. Feature A disperses from its deepest value of 1.30 eV at $h\nu = 22$ eV to its smallest value of 1.25 eV at $h\nu = 32$ eV. Feature D disperses as the photon energy is changed from 14 eV to 22 eV.

It is interesting to note the large intensity variations of each feature at low photon energies ($h\nu \leq 30$ eV). That's because the observed features are due to optical excitations from the valence band to low-lying conduction band states and a photon energy change requires another initial and final state, resulting in a dipole matrix-element change. But at high photon energies, nearly free electron states can be assumed for the final states and the dipole matrix element can be approximated by the atomic cross section of the levels.

Looking again at feature A in both materials, we can clearly see that it disperses over almost all photon energies. The vertical bars in the figures trace out the general movement of the peaks. There is some symmetry as they curve towards and away from E_F. Taking the symmetry to indicate the crossing of a Brillouin zone (BZ) boundary, we can calculate the inner potentials, V_0, of $EuNi_2Ge_2$ and $GdNi_2Ge_2$. The symmetric behavior of the dispersion of

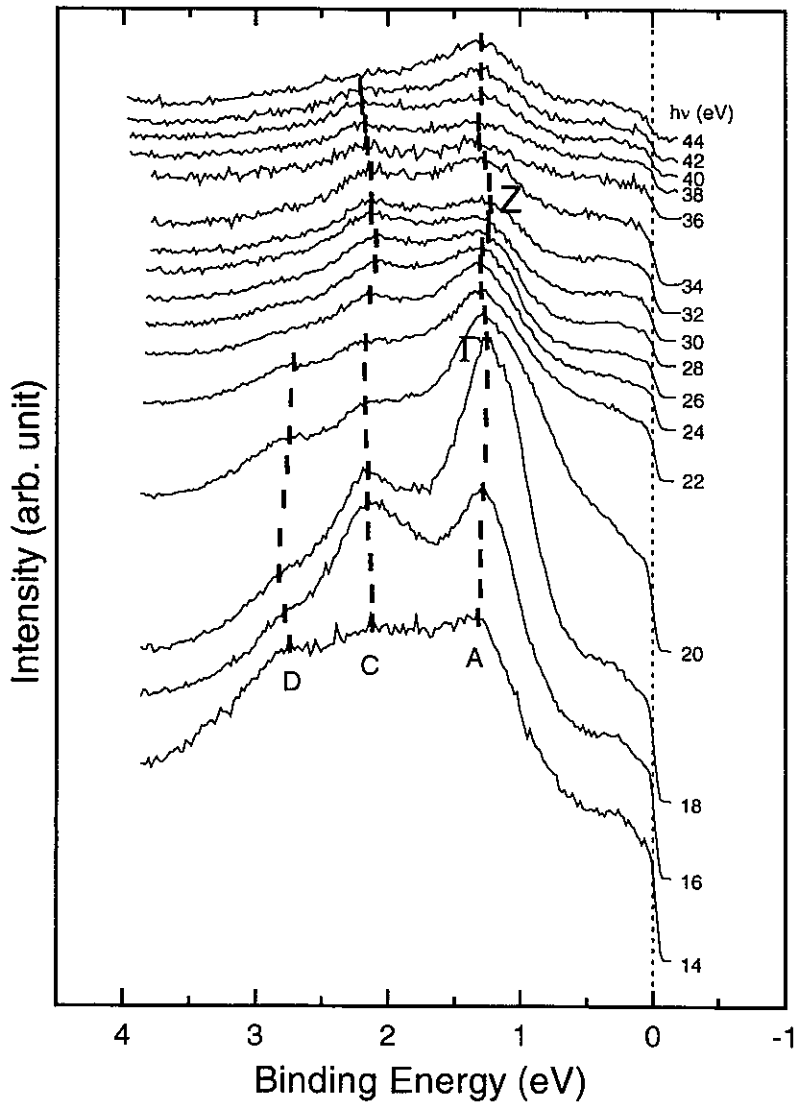

FIG. 4.16 EDCs for $GdNi_2Ge_2$ at normal emission from the (001) surface (Γ-Z direction) taken with increasing photon energy. Binding energies are referenced to the Fermi level (E_F). The vertical bars are a guide to the eye which qualitatively follow the major features of the scans.

feature A is required by crystal periodicity and can be used as a cross check in band dispersions of complicated systems [35]. These dispersions in Fig. 4.15 and Fig. 4.16 are strong enough that we were able to map them through k space and look for symmetry points. The high symmetry points, Γ and Z are indicated to the right and left of feature A in Fig. 4.15 and Fig. 4.16. For example, at $h\nu$ ~33 eV and $h\nu$ ~ 49 eV the center of BZ, Γ and the symmetry point on the BZ boundary, Z, respectively, are reached in $EuNi_2Ge_2$.

For the analysis of the experimental data, binding energy (E_B) and photon energy ($h\nu$) for the peaks are converted into an energy band dispersion $E(k)$ in a straightforward manner from the correspondence between the wave vector and the experimental photon energies using conservation of energy and momentum. An experimental E_B vs. $k_\perp$ relation is presented in Fig. 4.17 for $EuNi_2Ge_2$ and Fig. 4.18 for $GdNi_2Ge_2$ with $EuNi_2Ge_2$ for comparison. Fig. 4.17 clearly shows the Z points for both materials. For $GdNi_2Ge_2$ it is about 0.3 eV higher in binding energy than that of $EuNi_2Ge_2$. The transition from the crystal to vacuum is described as a potential step function, whose height corresponds to the work function of the actual material. Inside the crystal the electronic potential is approximated according to the muffin-tin model, i.e. spherically symmetric potentials around each atom and a constant potential in between [106]. The inner potential V_0 defines the loss of kinetic energy related to a potential barrier whose total height is V_0. $E_F - V_0$ is approximately the filled valence bandwidth. Since $k_\parallel$ is zero in normal emission, the k_z, the momentum perpendicular to the surface (001), is evaluated assuming the free electron-like final state model via the following equation:

$$k_\perp = k_z = (2m/\hbar^2)^{1/2}[h\nu - E_B - \Phi + V_0]^{1/2} \tag{4.10}$$

$$= 0.512(\text{Å}^{-1})\,[(h\nu - E_B - \Phi + V_0)/\text{eV}]^{1/2}. \tag{4.11}$$

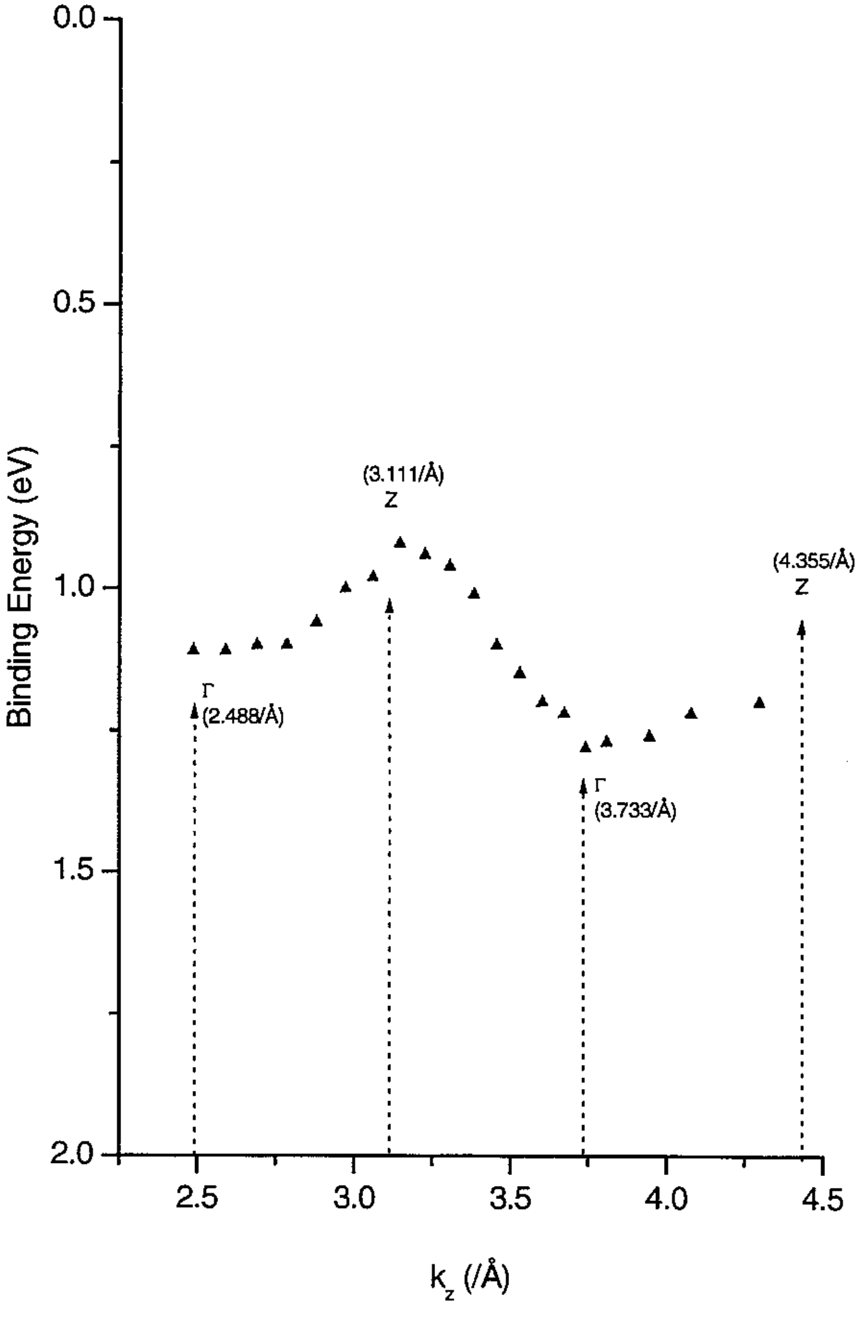

FIG. 4.17 Measured peak positions of feature A of $EuNi_2Ge_2$ as a function of k_z. The data in this figure are used to determine the symmetry points along [001]. The high-symmetry points Γ and Z are indicated, using the Brillouin zone lattice constant $k_c = 10.10$ Å^{-1}.

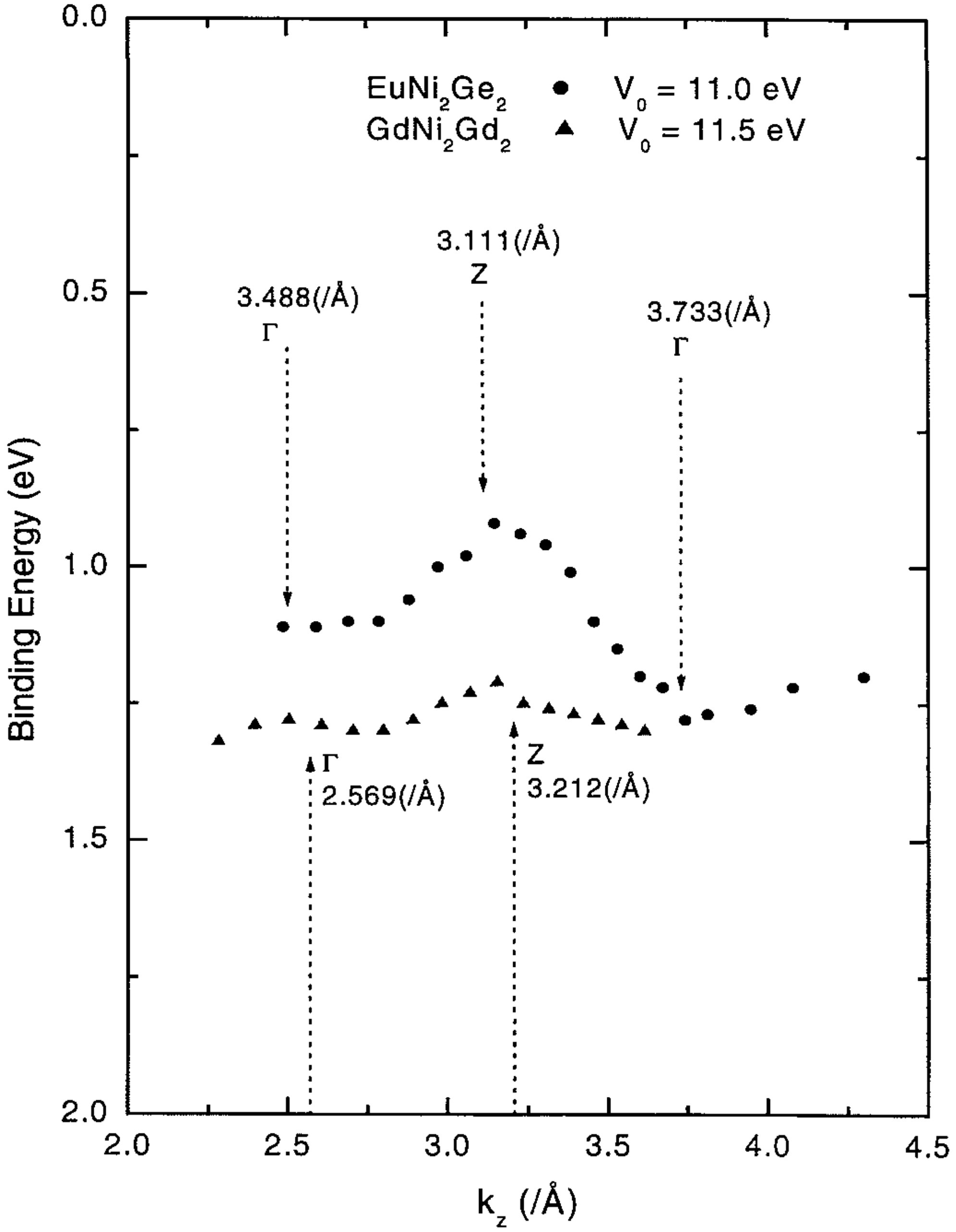

FIG. 4.18 Plots of measured peak positions of feature A for $GdNi_2Ge_2$ as a function of k_z. The high-symmetry points, Γ and Z are indicated, using the Brillouin zone lattice constant $k_c = 9.78$ Å^{-1}. It is also shown with $EuNi_2Ge_2$, Fig. 4.17 for comparison.

This approach is useful when the photon energy is above 30 eV, so that a free-electron final state is a reasonable approximation. The work function Φ was set to Φ = 4.3 eV and the inner potential V_0 is to be determined. In fact, the actual work function barrier seen by a photoelectron is the work function of the electron analyzer since the sample is in electrical contact with the energy analyzer but we assumed that it is very close to that of the sample itself. Going beyond the Z point at the zone boundary, the peak reverses its dispersion and traces its way back to the Γ point in the next Brillouin zone. This symmetric behavior of the dispersion around Γ and Z is required by the crystal periodicity and can be used to determine what the value of inner potential V_0 is. The inner potential can be estimated by adjusting V_0 to make $k_\perp$ fit the dispersion of repeating band feature A. The values of the inner potential for $EuNi_2Ge_2$ and $GdNi_2Ge_2$ were estimated to be 11.0 eV ± 0.2 eV and 11.5 eV ± 0.2 eV by using a direct-transition model and assuming a free-electron band structure, and they are excellent agreement with the bottoms of the free-electron-like bands (10.95 eV and 11.48 eV respectively) in the band structures in Ref [85].

We compare the experimentally measured band dispersions with the theoretical band structure calculations along the Γ-Z performed by Islam [85] in Fig. 4.19. The full curves are the band structure calculation results. Superimposed are the experimentally observed peak positions - experimental band structure - relative to E_F taken from Fig. 4.15.

Looking at the band structure calculations, we can see that there are a large number of bands in this area. As expected, most of them are relatively flat. A few bands were not observed because certain transitions can be forbidden by symmetry selection rules which exclude some of the transitions and specify that only a few of the available final states can

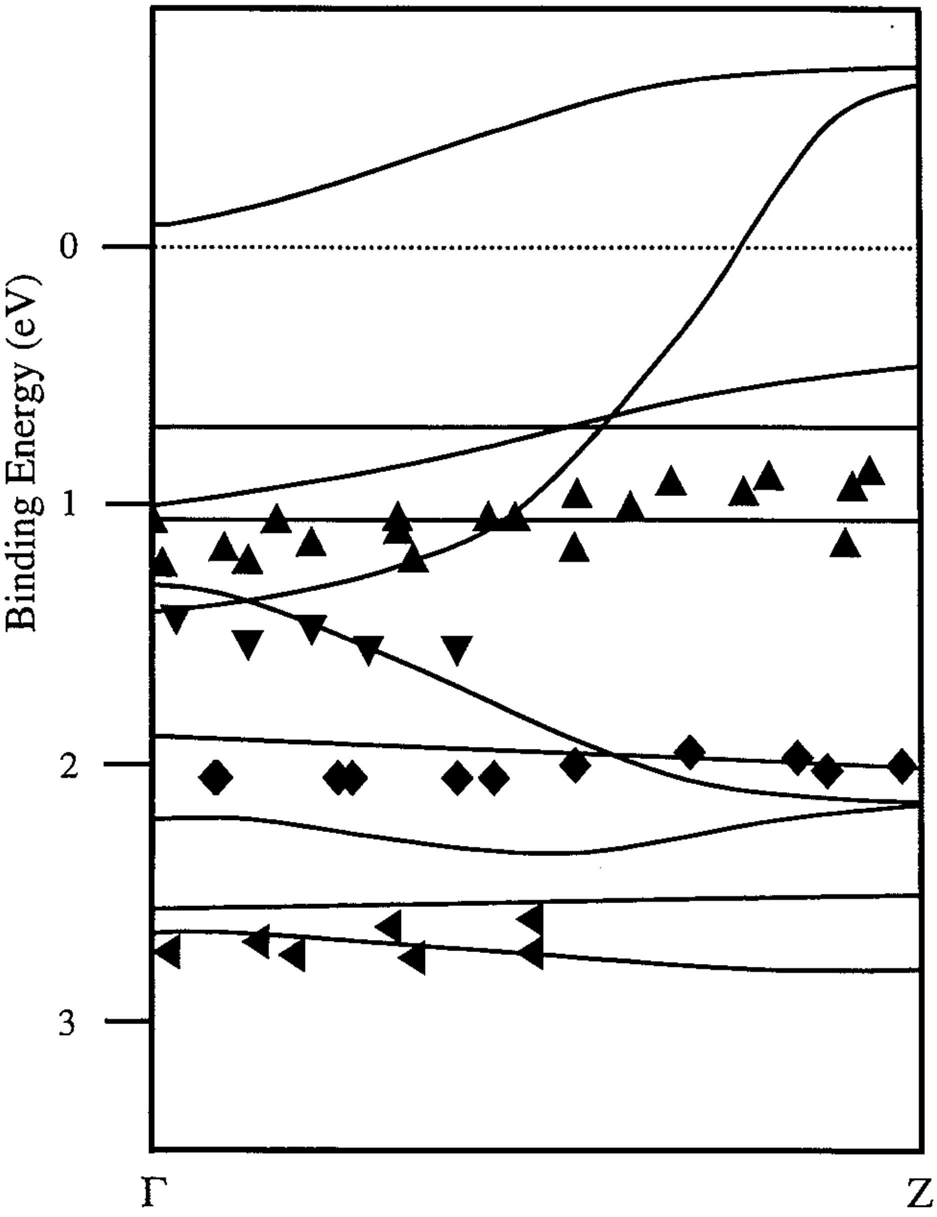

FIG. 4.19 The measured band dispersion of $EuNi_2Ge_2$ along the Γ-Z [001] direction in comparison with the band structure calculations [85](full curves). Symbols show the observed direct-transition features: A (triangle), B (inverted triangle), C (diamond), and D (leftward triangle).

contribute to the photocurrent for this experimental geometry. The band dispersions appear to be consistent with the theoretical calculations, but compared with the band structure calculation there is a rigid downward shift of the experimentally determined band structure. According to Ref [85], Islam calculated the generalized electric susceptibility $\chi_0(q)$ by shifting the Fermi energy (E_F) upward by 10 mRyd (to $E'_F = E_F + 0.136$ eV) for $EuNi_2Ge_2$ and 7 mRyd (to $E''_F = E_F + 0.095$ eV) for $GdNi_2Ge_2$ in order to adjust his nesting vectors. He pointed out that such a shift is not unreasonable for band calculations using the ASA, when multiple bands with different orbital characters cross E_F.

Figure 4.20 demonstrates experimental photoemission data and results of theoretical band structure calculations where E_F is shifted up by 10 mRyd (~0.136 eV). In this case the experimental band structure of $EuNi_2Ge_2$ fits apparently much better with the theoretical band calculation. Therefore it seems true that it often is found necessary to shift the position of E_F within the accuracy of the electron energies, by ~ 1% of the filled bandwidth to align the experimental band structure with those of LMTO-ASA calculations which corresponding to approximately 0.14 eV, 0.20 eV, and 0.07 eV for transition metal *s*, *p*, and *d* bands, respectively [13]. But for $GdNi_2Ge_2$, experimental photoemission data show a little better agreement with the original band structure rather than one with E_F shifted upward by 7 mRyd (~0.095 eV) as shown in Figs. 4.21-4.22.

Theoretically, the addition of exactly 'one' electron (1e/formula unit) was obtained from the DOS of $EuNi_2Ge_2$ based on the rigid-band approximation. This has the effect of lifting the Fermi energy (E_F) of $EuNi_2Ge_2$ by ~ 0.3 eV [11]. Our results for $GdNi_2Ge_2$ show that all of the observed band features have higher binding energies by 0.2 eV - 0.3 eV compared to

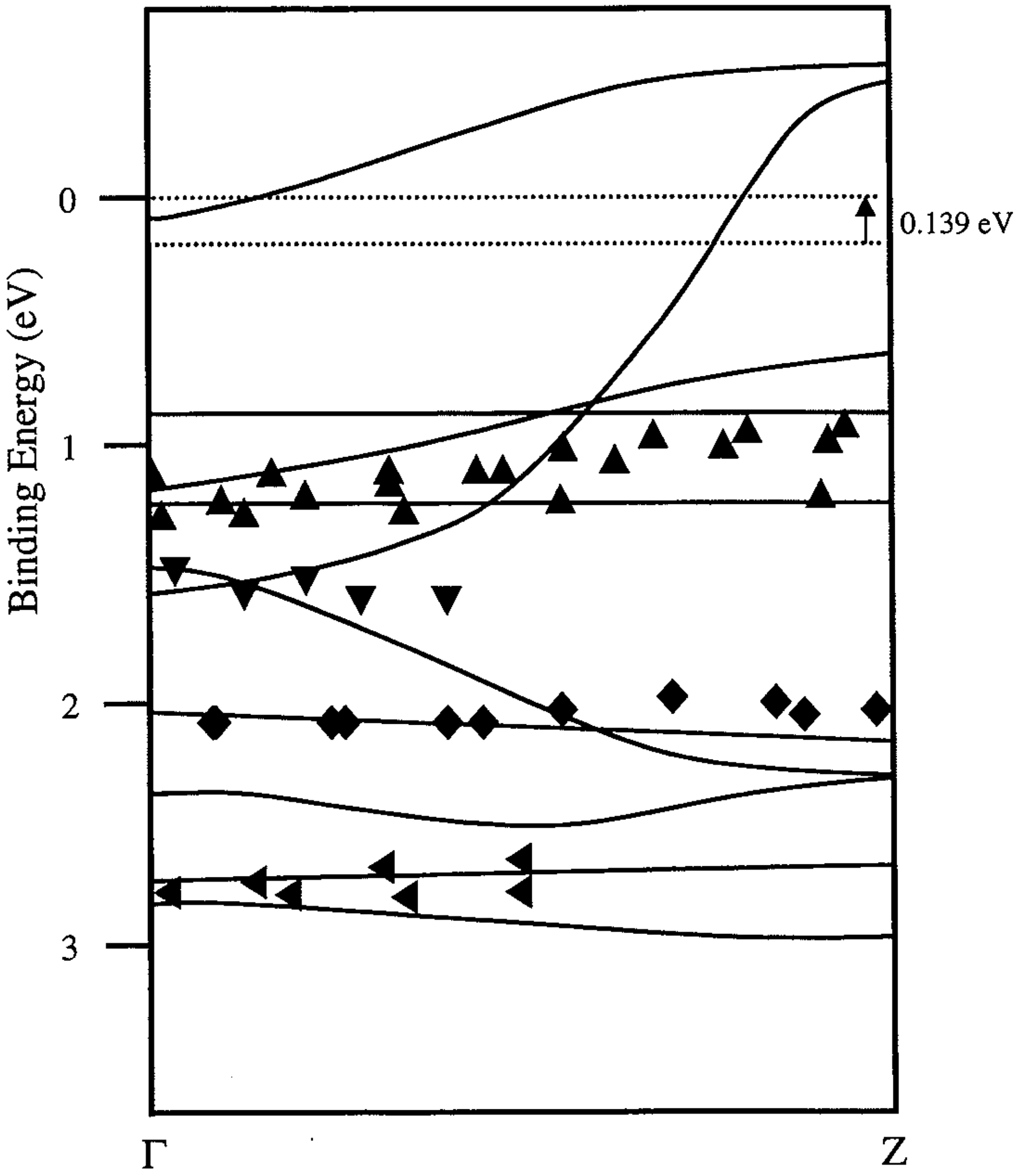

FIG. 4.20 Experimental photoemission data and results of band structure calculations of $EuNi_2Ge_2$ where Fermi energy is shifted up by 10 mRyd (~0.136 eV) [85].

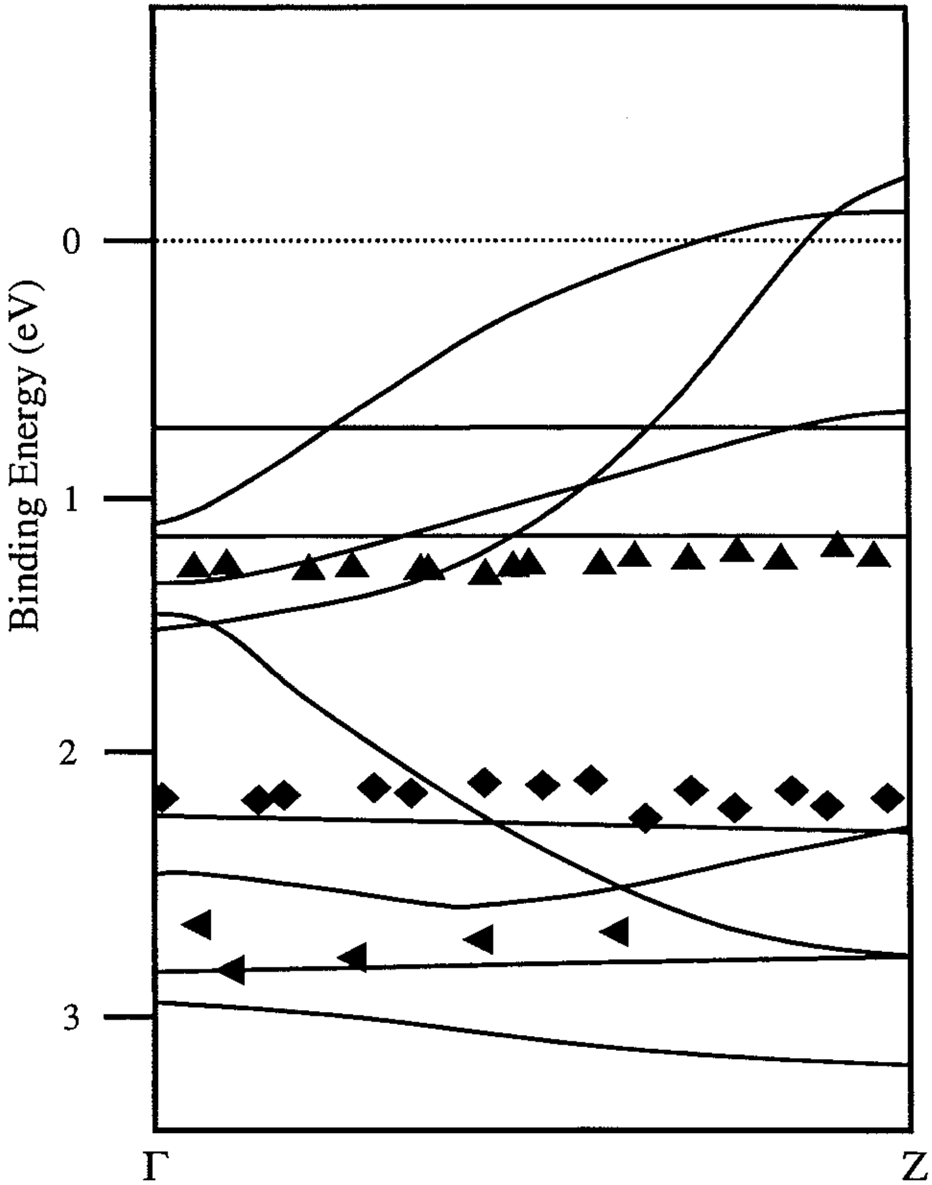

FIG. 4.21 The measured band dispersion of $GdNi_2Ge_2$ plot along the Γ-Z [001] direction in comparison with the band structure calculations [85](full curves). Symbols show the observed direct-transition features: A (triangle), C (diamond triangle), and D (leftward triangle).

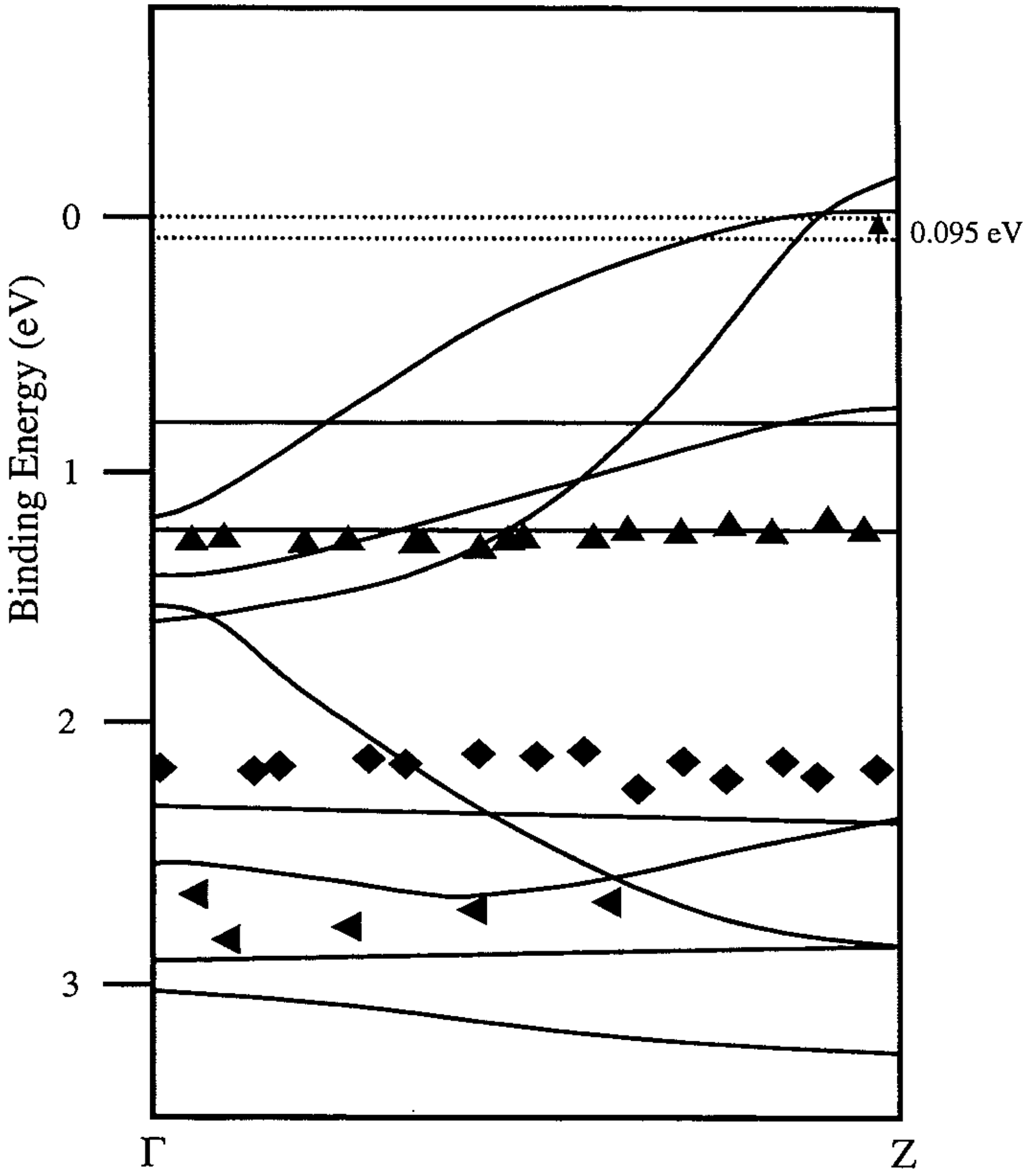

FIG. 4.22 Experimental photoemission data and results of band structure calculations of $GdNi_2Ge_2$ where Fermi energy is shifted up by 7mRyd (~0.095 eV) [85].

those of $EuNi_2Ge_2$. Therefore the observed binding energy shift can be interpreted quantitatively by a rigid-band shift of E_F based on the so-called-rigid-band model as a first approximation, which was first employed in CuNi alloys by Mott [107], although a rigid-band description has been shown to be unsuccessful for some electronic states of alloys from photoemission investigations [108, 109]. Our present results are also consistent with the interpretation by Islam *et al.*[11] in which the E_F shift simply corresponds to an increase of one electron (1e/formula unit) per rare-earth atom upon going from $EuNi_2Ge_2$ to $GdNi_2Ge_2$. This is due to the fact that the band structure and total DOS in $EuNi_2Ge_2$ and $GdNi_2G_2$ are not the same, but very similar, which suggests that a rigid-band model is adequate as a first approximation in the electronic structure. In fact, the lattice parameters of $EuNi_2Ge_2$ are 3% larger than those of $GdNi_2Ge_2$ due to the larger ionic radius of divalent Eu, but it is assumed that it does not affect rigid-band filling much. Ignoring the difference of lattice parameters in both materials was previously supported by Islam [11], who repeated generalized susceptibility $\chi_0(\mathbf{q})$ calculations by swapping the lattice constants between two compounds and found no significant changes.

In the electronic band calculation, the Eu 4*f* and Gd 4*f* electrons were treated as part of the atomic cores and it is assumed that their paramagnetic bands will be strongly similar to those of $EuNi_2Ge_2$ and $GdNi_2Ge_2$. Therefore, the bct BZ is used in the analysis of the photoemission spectra rather than those corresponding to the perfect AF state. From our results it is also justified that the Eu-4*f* and Gd-4*f* electrons can be treated as core electrons in the band calculations.

Angle-resolved photoemission of $EuNi_2Ge_2$

In this study, we will observe the Fermi surface (FS) geometry in the ΓXPZ plane of the Brillouin zone (BZ) by performing angle-resolved photoemission experiments on a single crystal of $EuNi_2Ge_2$. Figure 4.23 shows several sets of angle-resolved EDCs from $EuNi_2Ge_2$ taken with photon energies of (a) 19 eV and (b) 20 eV from an (001) surface while changing the angle in the [110] direction (in the ΓXPZ plane). The photoelectron-emission angles relative to the surface normal θ are marked next to each curve. All features show, upon decreasing the collection angle, a peak that sharpens upon approaching E_F, then drops as the initial states cross E_F. As the dispersing feature passes through E_F, an abrupt drop-off in spectral intensity occurs since photoemission only measures occupied electronic states. To determine a point on the FS, we look for the combination of a dispersing spectral feature that signals an energy band moving toward E_F, followed by an abrupt intensity falloff as the spectral feature passes through E_F [110].

It can be seen that all bands disperse toward E_F on going from higher to lower angles as indicated in Fig 4.23-(a) and -(b). For example, Fig. 4.23-(a) shows that a prominent feature appears with high intensity at about 0.3 eV binding energy (BE) when $\theta = 30°$ and possibly signifies an E_F crossing at about $\theta = 24°$. The spectral intensity abruptly falls off as this band crosses E_F. We can also see from Fig. 4.23-(b) that the E_F crossing is 22° for $h\nu = 20$ eV. Each gives a point in a BZ lying on a FS. Vertical bars following the path in the features are included to help guide the eye. The figures show at which angle the scans cross the BZ boundary and symmetry lines. The angle of the Γ-X symmetry line is 20° for $h\nu = 19$ eV

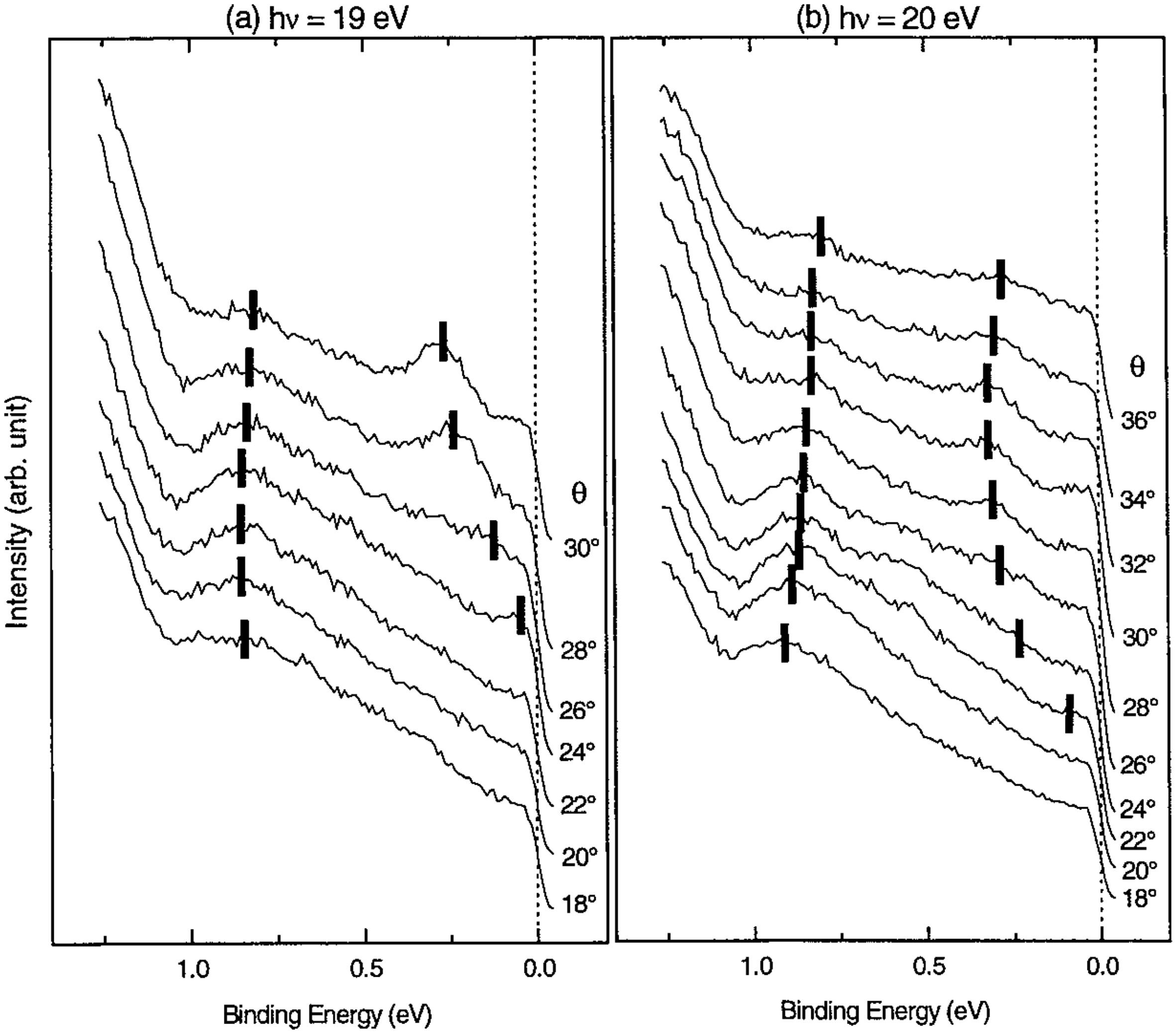

FIG. 4.23 Several sets of angle-resolved EDCs from $EuNi_2Ge_2$ taken with photon energy of (a) 19 eV, (b) 20 eV from a (001) surface at k points in the ΓXPZ plane. (θ is emission angles from the sample normal). The vertical bars are a guide to the eye which qualitatively follow the major features of the scans.

in Fig. 4.23-(a). The angle of the BZ boundary is approximately 32° for $h\nu = 20$ eV. From these symmetric behaviors of the dispersion around symmetric lines, the inner potential of 11.0 eV was also crosschecked. From Fig. 4.24-(a) we can observe a ΓX symmetry line crossing at an angle of 36° and a BZ boundary crossing at an angle of 28° in the higher binding energy feature. We can also see from Fig. 4.24-(b) that the E_F crossing is 20 ° for $h\nu = 24$ eV.

Figure 4.25-(a) shows the angle of the BZ boundary is approximately 14° for $h\nu = 29$ eV from the symmetry behavior around 14°. Examining Fig. 4.25-(a) and -(b) one can observe that the E_F crossings are 18° for $h\nu = 29$ eV and 18° for $h\nu = 31$ eV.

Figure 4.26 shows EDCs taken with photon energies of (a) 15 eV and (b) 17 eV from a (001) surface while changing angle in the [110] direction (in the ΓXPZ plane). The peak positions are indicated by vertical bars. Fig. 4.26-(a) and (b) indicate that the E_F crossings are 26° for $h\nu = 15$ eV, and 24 ° for $h\nu = 17$ eV

A series of energy distributions are recorded for photon energies and electron collection angles as in Figs. 4.23-4.26. For the case of $EuNi_2Ge_2$ an inner potential of 11.0 eV gave a good fit of the free-electron parabola with the experimental normal emission data in Fig. 4.15 and Fig. 4.17 and work function Φ was set to 4.3 eV. A point on the FS is defined as a value of k at which a peak disperses across E_F. The E_F crossings for $EuNi_2Ge_2$ in Figs. 4.23-4.26 are strong enough that we were able to map them through k space and use symmetry to locate the BZ boundaries in the [001] and [110] directions.

Figure 4.27 shows the location of the Fermi surface (FS) crossing at different points mapped onto the ΓXPZ plane of $EuNi_2Ge_2$ using the extended zone scheme. The rest of the

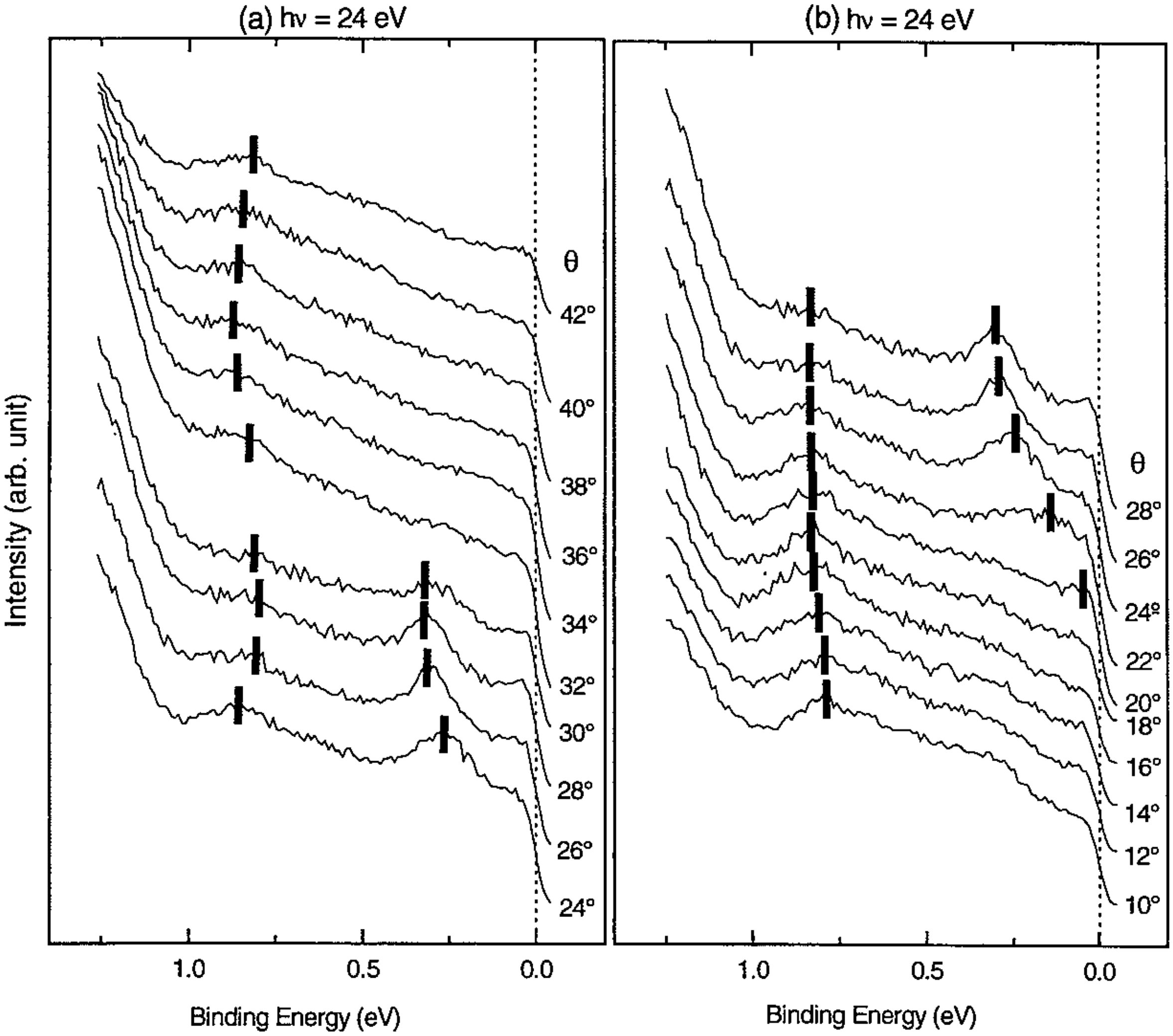

FIG. 4.24 EDCs from $EuNi_2Ge_2$ taken with photon energy of 24 eV from a (001) surface The photoemission data have been taken at k points in the ΓXPZ plane (θ is emission angles from the sample normal).

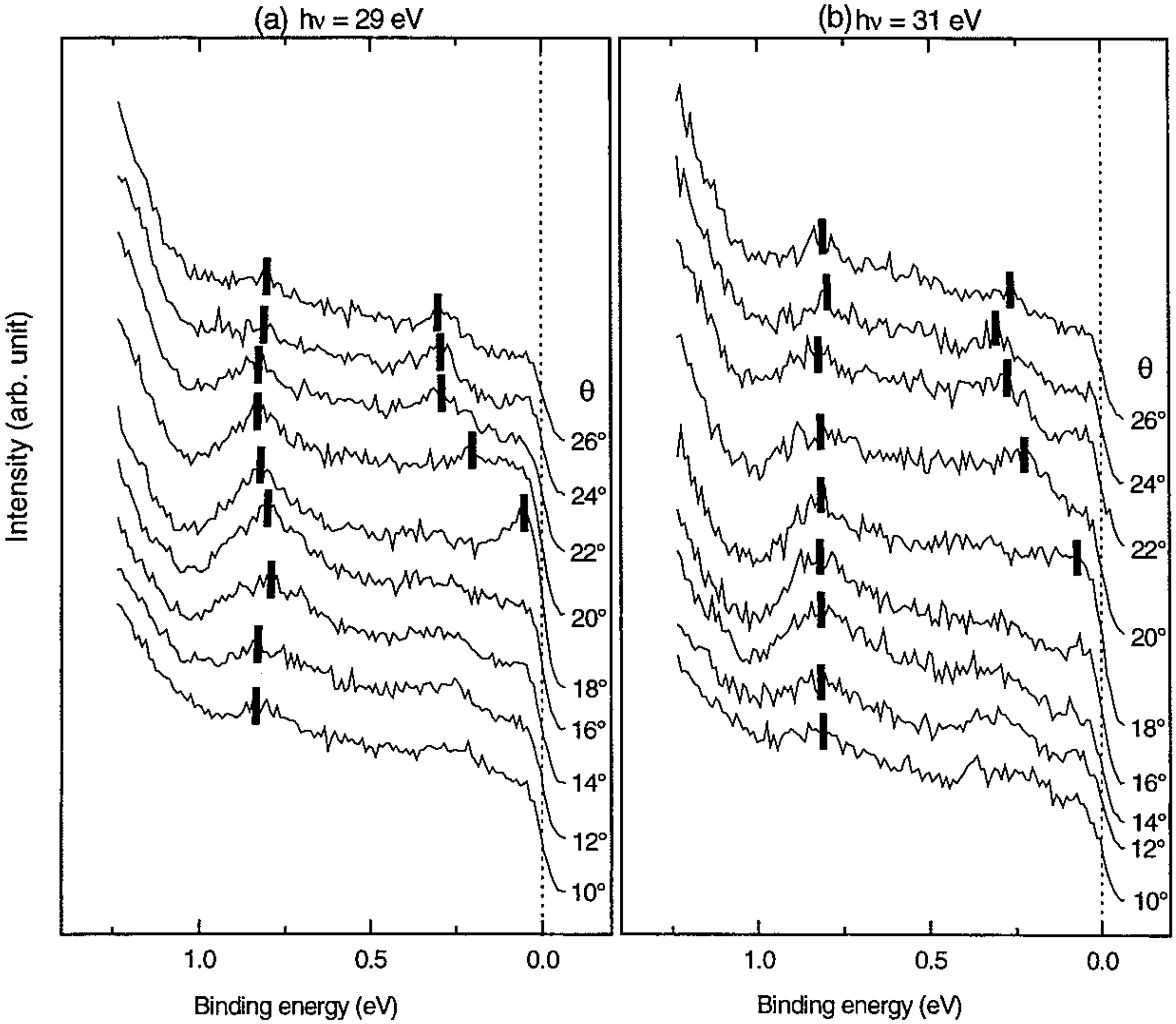

FIG. 4.25 EDCs of $EuNi_2Ge_2$ taken with photon energies of (a) 29 eV and (b) 31 eV from a (001) surface while changing the angle in the [110] direction (in the ΓXPZ plane). The peak positions are indicated by vertical bars.

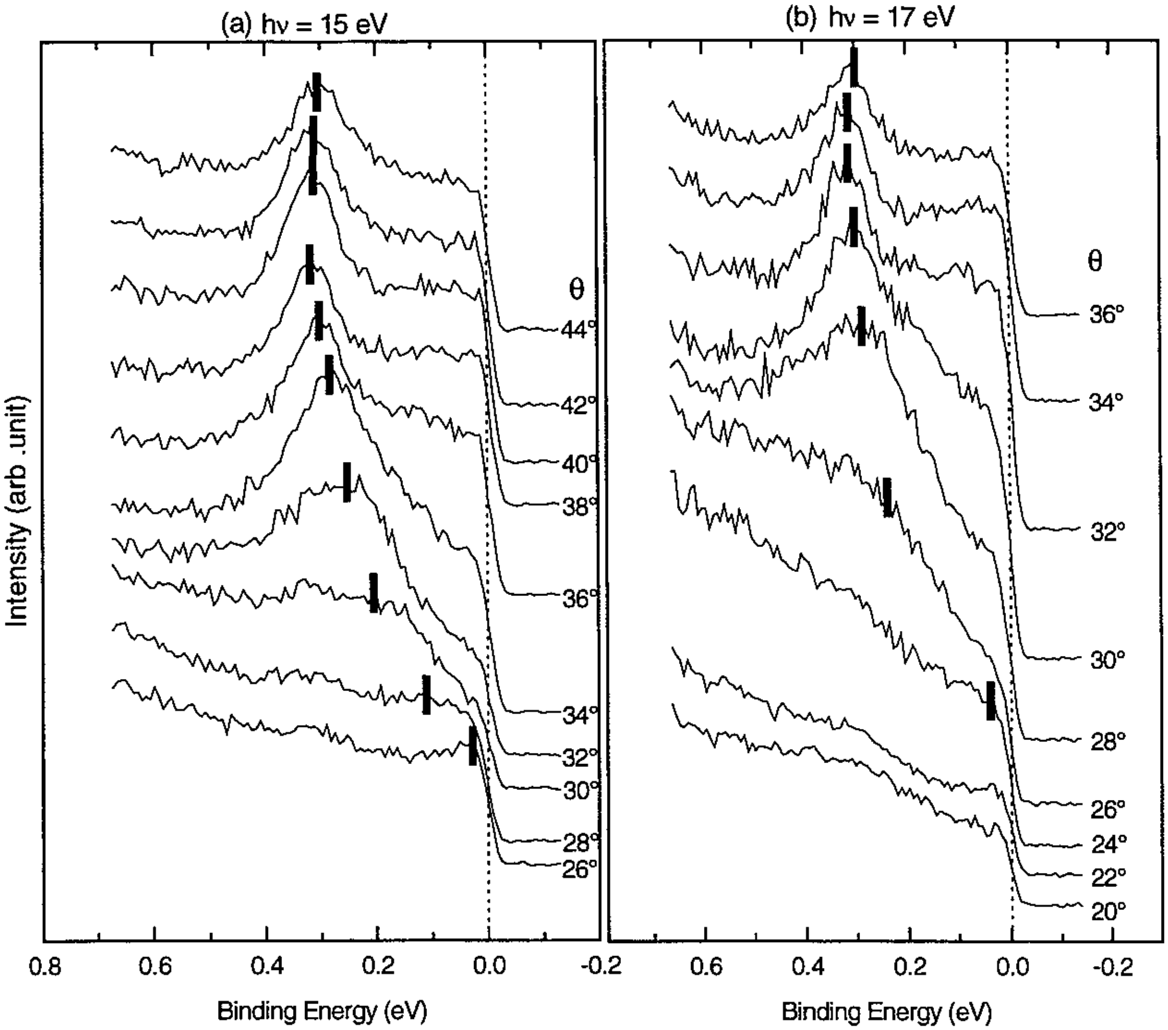

FIG. 4.26 EDCs of $EuNi_2Ge_2$ taken with photon enrgies of (a) 15 eV and (b) 17 eV from a (001) surface while changing angle in the [110] direction (in the ΓXPZ plane). The peak positions are indicated by vertical bars.

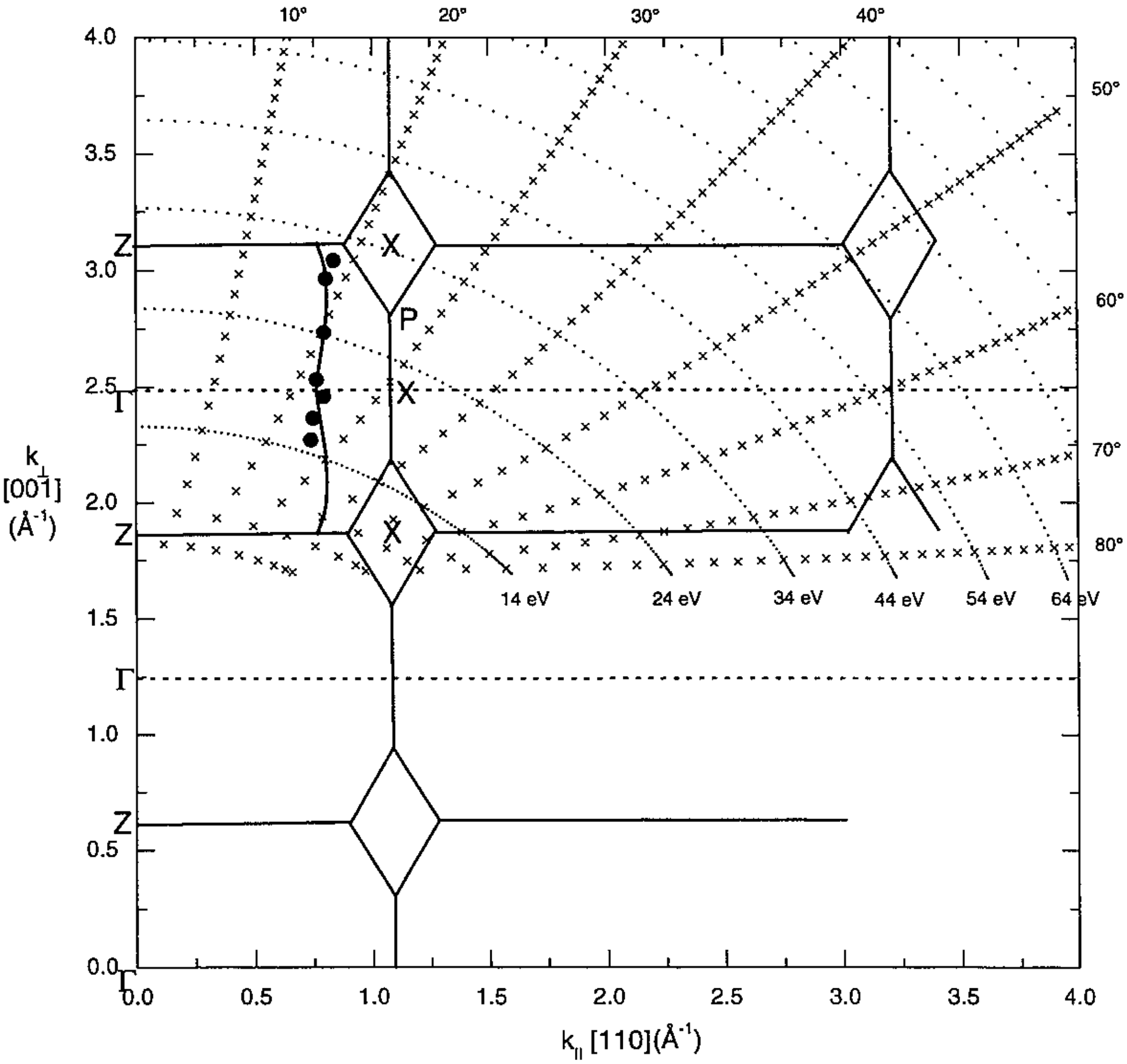

FIG. 4.27 Fermi surface mapped in the ΓXPZ plane of $EuNi_2Ge_2$ using an extended zone scheme. Black filled circles indicate the experimental data. Solid line indicates the theoretical Fermi surface of $EuNi_2Ge_2$ by Ref [85].

BZ was assumed to be symmetrical due to tetragonal symmetry of the crystal structure. The filled circles represent E_F crossing points determined from dispersions in Figs. 4.23-4.26. They are part of the hole surface around Γ in the BZ, indicating that the occupied electronic state is in the right-hand part of the ΓXPZ plane of $EuNi_2Ge_2$. We see then, that the FS forms an open orbit along the c axis. The curved line is based on the band calculation from Ref [85]. The band structure of $EuNi_2Ge_2$ shown along selected high symmetry lines is shown in Fig. 4.28. In fact, two bands cross along ΓX but only the band crossing nearest to X is observed. If we compare this experimental section of the FS with the theoretical FS, we see a close correspondence of the theoretical and experimental FS. We could also check the inner potential $V_0 \sim 11.0$ eV, looking for variations in binding energy and intensities which locate the symmetry lines and zone boundaries.

Angle-resolved photoemission of $GdNi_2Ge_2$

Previous ARPES measurements of $GdNi_2Ge_2$ have been performed by Brammeier [111]. He has differing results with the band structure calculations from Islam [85], further requiring this present experimental study. Brammeier's experimental Fermi surface (FS) points in the ΓXPZ plane were offset by half a Brillouin zone (BZ), compared with the theoretical one. The origin of discrepancy is now known – a misaligned crystal leading to an incorrect direction in *k* space. The first purpose of present additional ARPES measurements of $GdNi_2Ge_2$ is to correct the previous wrong one by finding what the FS of $GdNi_2Ge_2$ looks

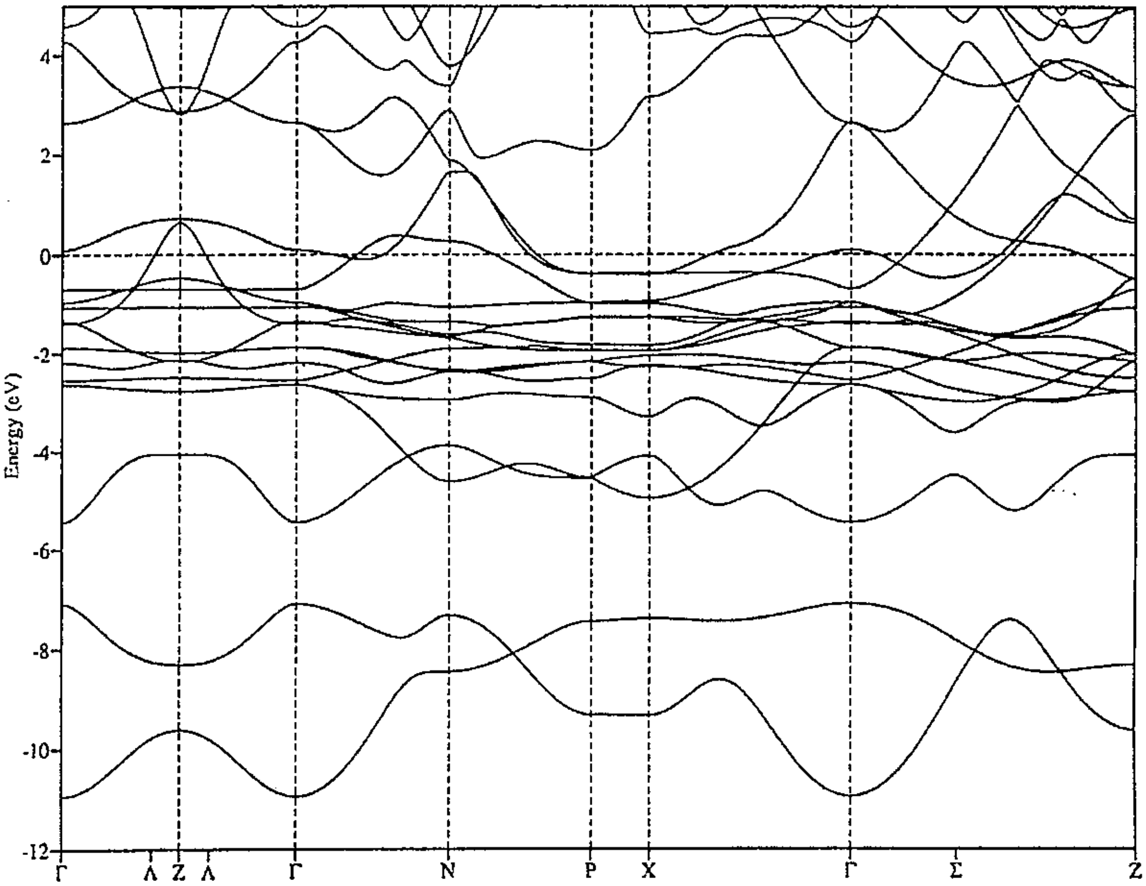

FIG. 4.28 Band structure of $EuNi_2Ge_2$ shown along selected high symmetry lines (see Fig. 2.4 for details). The band structure is the result of a tight-binding linear-muffin-tin-orbital calculation using the atomic-sphere approximation (after [85]).

like. Second, we are going to confirm any band-filling effect by looking for the FS of $GdNi_2Ge_2$ and see how it is different from that of $EuNi_2Ge_2$. Similarly, angle-resolved EDCs from $GdNi_2Ge_2$ taken with each photon energy from an (001) surface at k points in the ΓXPZ plane are shown in Figs. 4.29 – 4.31, which show that prominent features appear with high intensity at about 0.3 eV BE. But dispersing features near E_F are weaker than those of $EuNi_2Ge_2$, which causes difficulty in resolving any dispersive features. But we need to note that when a dispersing band feature passes through E_F, the step heights at E_F drop by around 20 % in $EuNi_2Ge_2$, and 8% in the case of $GdNi_2Ge_2$. For $GdNi_2Ge_2$ it is assumed that the reduction in the step height of E_F may be attributed to the fact that a dispersing feature passed through E_F [112], since as a whole the intensity variation between spectra was not large around the end of each spectrum on the high binding side. Similar, but less prominent reductions of step height at E_F occur in $EuNi_2Ge_2$. We plotted step height at E_F vs. angle for $EuNi_2Ge_2$ in Fig. 4.32-(a). Analyzing the resulting plots we were able to find the E_F crossings, that were at the same angles as those determined from the dispersing features. Thus, considering the drop in the step height at E_F when a dispersive feature crosses E_F, we were able to find E_F crossings in the spectra of $GdNi_2Ge_2$ where we cannot see clearly dispersing peaks. The plot of step height at E_F vs. angle for $GdNi_2Ge_2$ is shown in Fig. 4.32-(b). But in the spectra taken with a photon energy of 30 eV the maximum step height of E_F could not be determined unambiguously, although a lower-limit (angle) for the E_F crossing for that is shown in Fig. 32-(b), since more of spectra with higher angles are needed. From Fig. 4.32-(b) we know that the E_F crossings are 10° for $h\nu = 20$ eV, 12° for $h\nu = 22$ eV, 16° for $h\nu = 24$ eV, 16° for $h\nu = 26$ eV, and 18° for $h\nu = 30$ eV. The locations of the Fermi-energy crossing at different points mapped onto the ΓXPZ plane of $GdNi_2Ge_2$ using

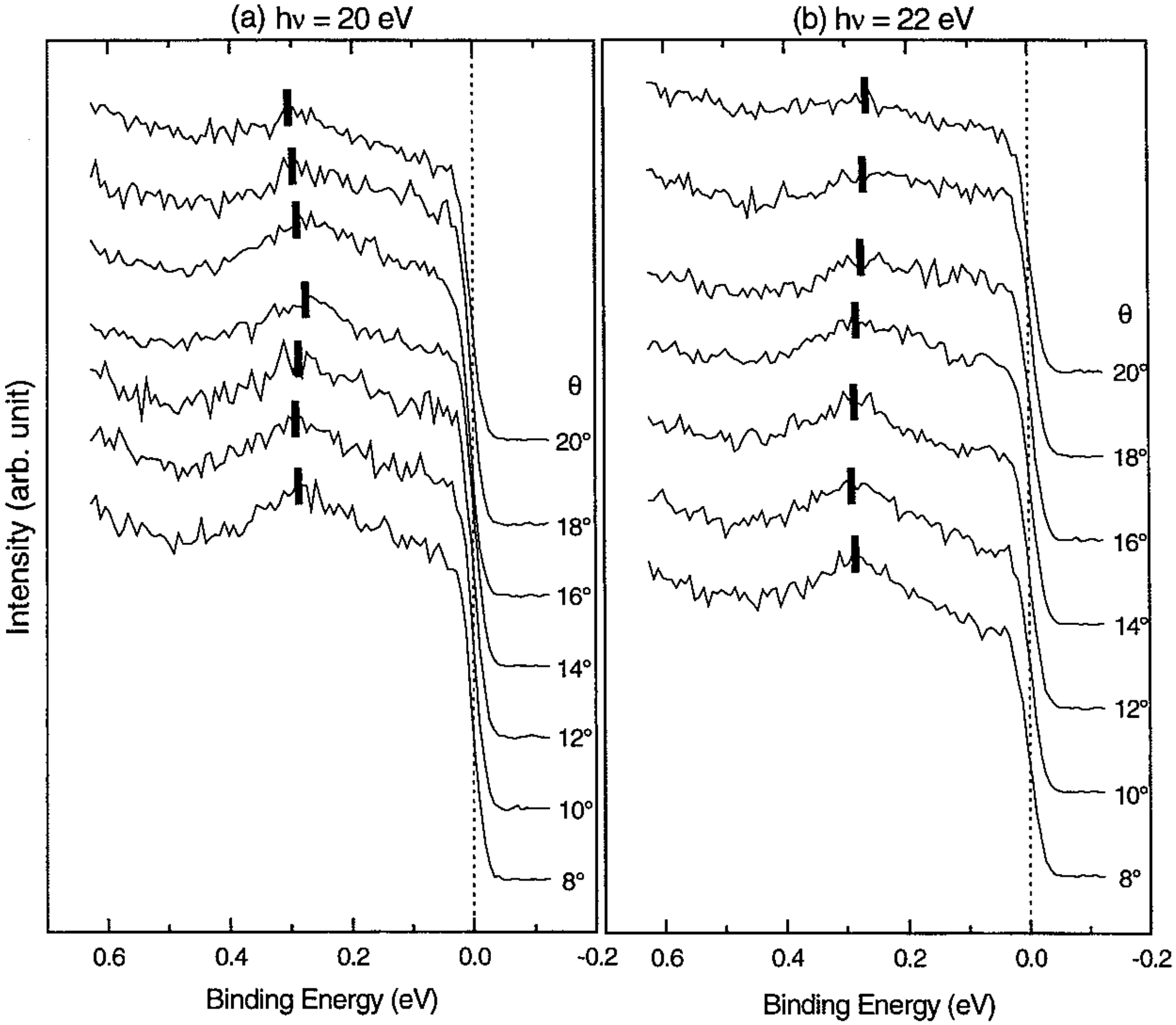

FIG. 4.29 The angle-resolved EDCs from $GdNi_2Ge_2$ taken with photon energies of (a) 20 eV, (b) 22 eV from a (001) surface at *k* points in the ΓXPZ plane. (θ is emission angles from the sample normal). The vertical bars are a guide to the eye which qualitatively follow the major features of the scans.

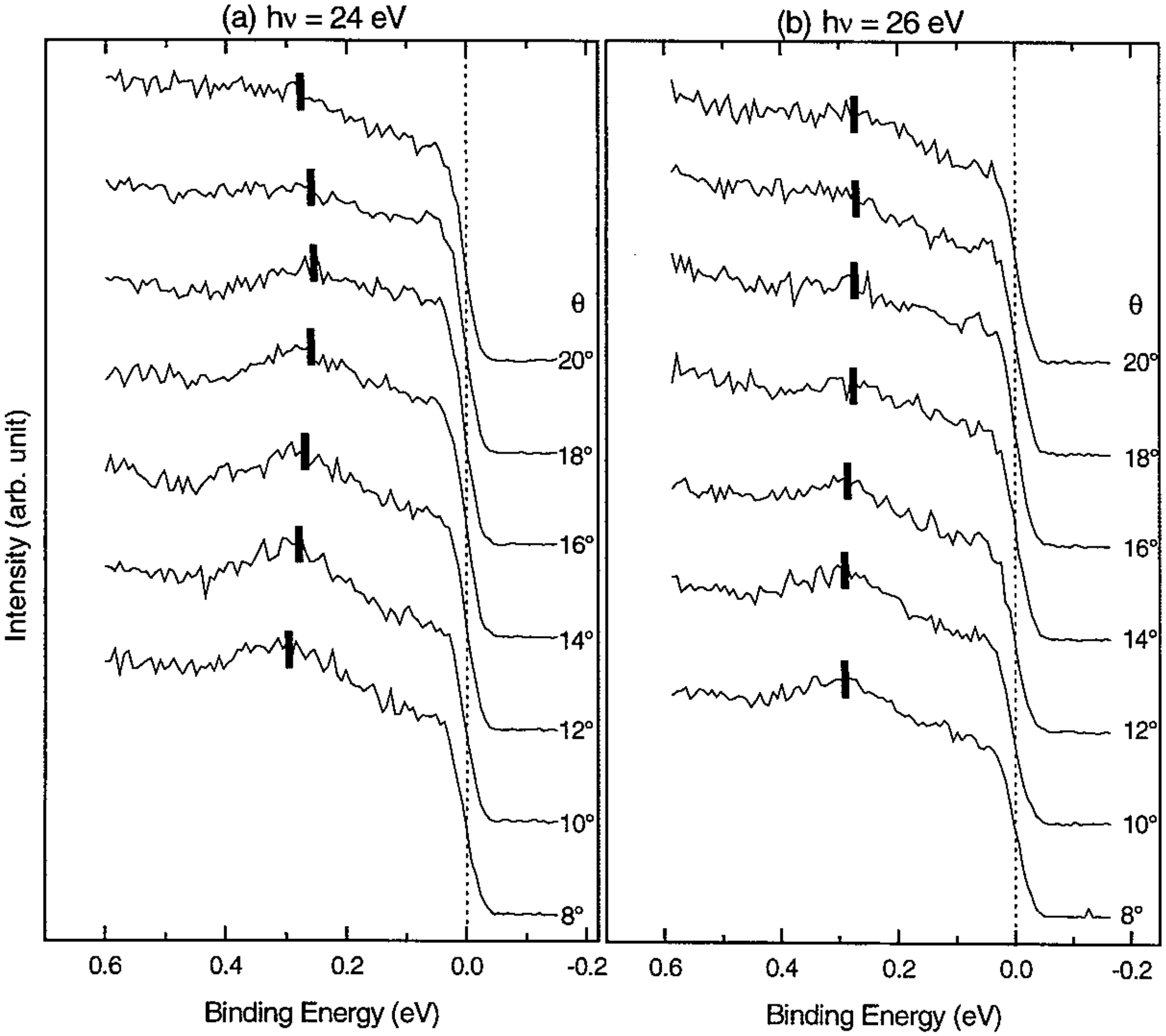

FIG. 4.30 EDCs of $GdNi_2Ge_2$ taken with photon energies of (a) 24 eV and (b) 26 eV from a (001) surface while changing the angle in the [110] direction (in the ΓXPZ plane). The peak positions are indicated by vertical bars.

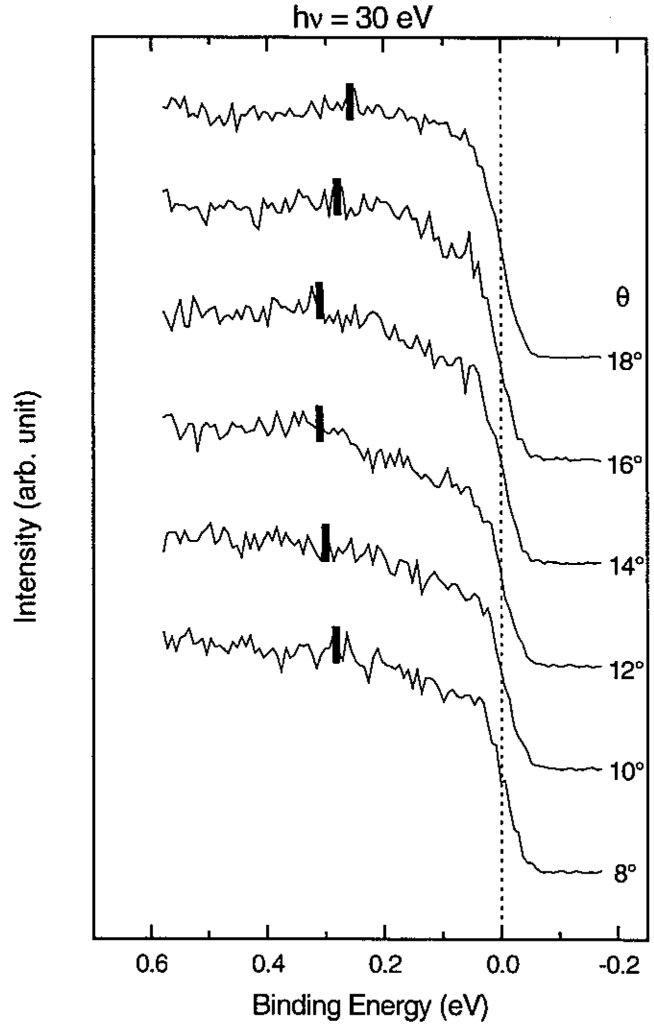

FIG. 4.31 EDCs from $GdNi_2Ge_2$ taken with photon energy of 30 eV from a (001) surface at *k* points in the ΓXPZ plane. (θ is emission angles from the sample normal.

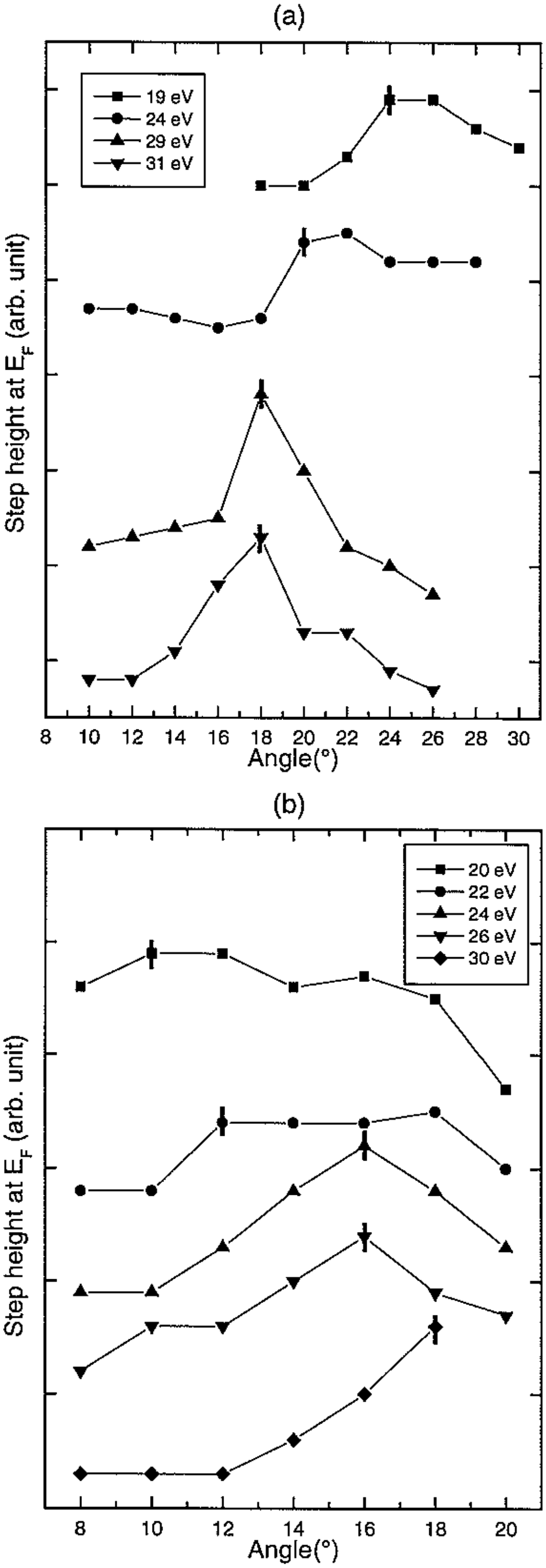

FIG. 4.32 Step height at E_F vs. angle for (a) $EuNi_2Ge_2$ and (b) $GdNi_2Ge_2$. The vertical bars indicate E_F crossings for each photon energy.

the extended zone scheme are shown in Fig. 4.33. It shows that the right-hand part of the ΓXPZ plane of $GdNi_2Ge_2$ is the occupied electronic state. Compared to the FS of $EuNi_2Ge_2$, that of $GdNi_2Ge_2$ has a bulge around the Γ point. That is due to the fact that the Gd ion in $GdNi_2Ge_2$ has a valence of 3+ with an extra conduction electron (1e/formula unit), confirming again the effects of rigid-band filling on electronic structures together with the previous data of the energy band mappings. Thus a simple rigid-band model offers a way to estimate the amount of E_F variation, corresponding to increase of exactly 'one' electron in $EuNi_2Ge_2$, upon going from $EuNi_2Ge_2$ to $GdNi_2Ge_2$. The band structure of $GdNi_2Ge_2$ shown along selected high symmetry lines is shown in Fig. 4.34.

Figure 4.35 shows a high-energy resolution (ΔE = 38 meV) angle-resolved photoemission (ARPES) spectrum of $EuNi_2Ge_2$ measured at 20 K at a photon energy of 19 eV and angle of 24° normal to the (001) surface which shows a E_F crossing to find any experimental evidence for the existence of a spin density wave (SDW), as in a prototype itinerant antiferromagnet (AF) Cr. A HRPES (High Resolution Photoemission Spectroscopy) spectrum of a Pt foil measured under the same conditions is shown for a reference of the Fermi function. Overhauser [113] was one of the first to attempt a theoretical development for the AF SDW ground state in Cr. Later Lomer [114] first pointed out that large, nearly parallel, constant-E_F surfaces, such as the electron surface at Γ and the hole surface at H in the BZ, which are separated by nesting vector **Q**, are responsible for the existence of the SDW below T_N. It is reasonable to assume that some SDW gaps remove a portion of the paramagnetic FS, and thus transfer some of the states to below and above E_F. Therefore in transforming from the paramagnetic to the AF, new energy band gaps will occur around E_F.

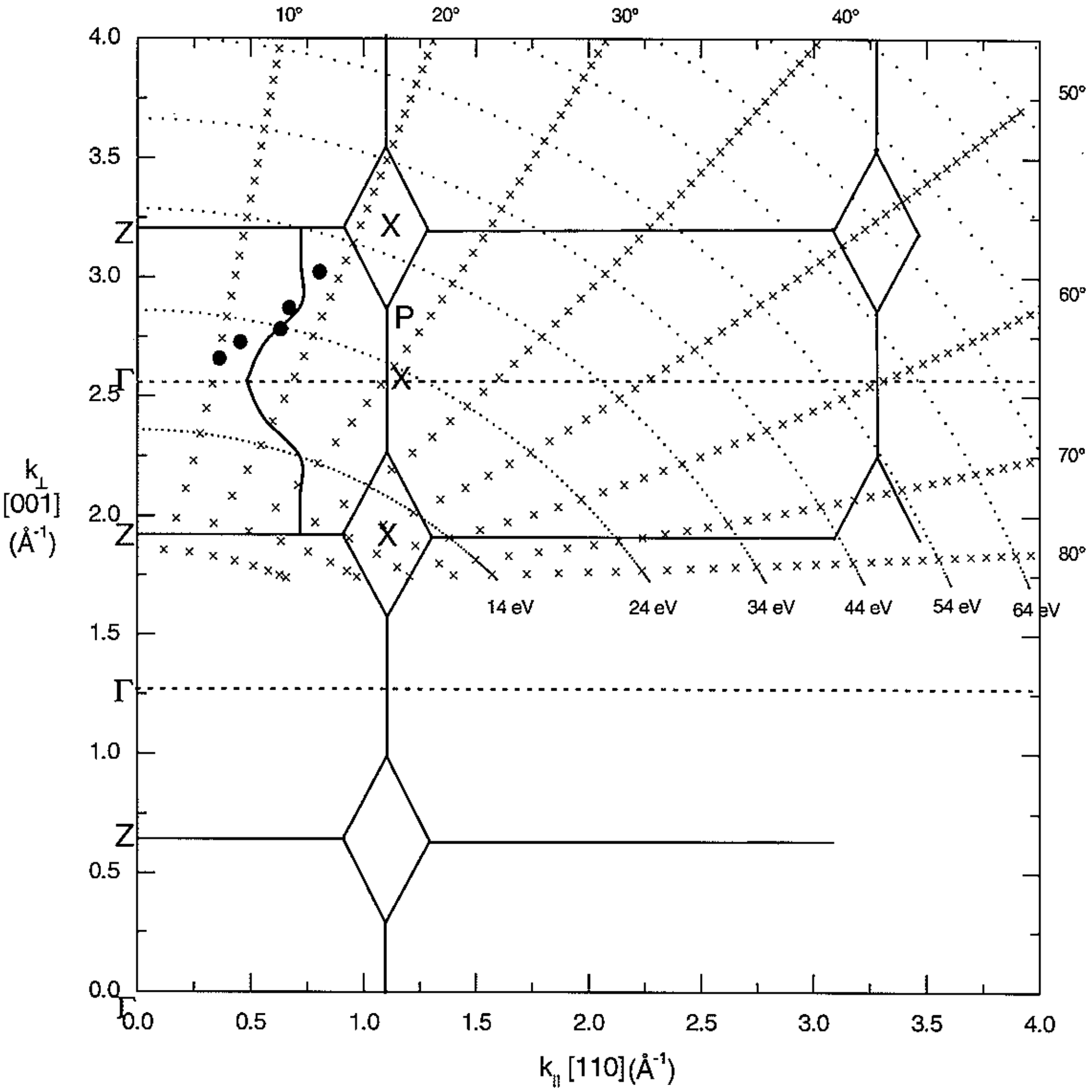

FIG. 4.33 Fermi surface mapped in the ΓXPZ plane of $GdNi_2Ge_2$ using an extended zone scheme. Black filled circles indicate the experimental data, whose size correspond to the angular resolution, about 6% of the distance from Γ to X in the BZ. The solid line indicates the theoretical Fermi surface of $GdNi_2Ge_2$ by Ref [85].

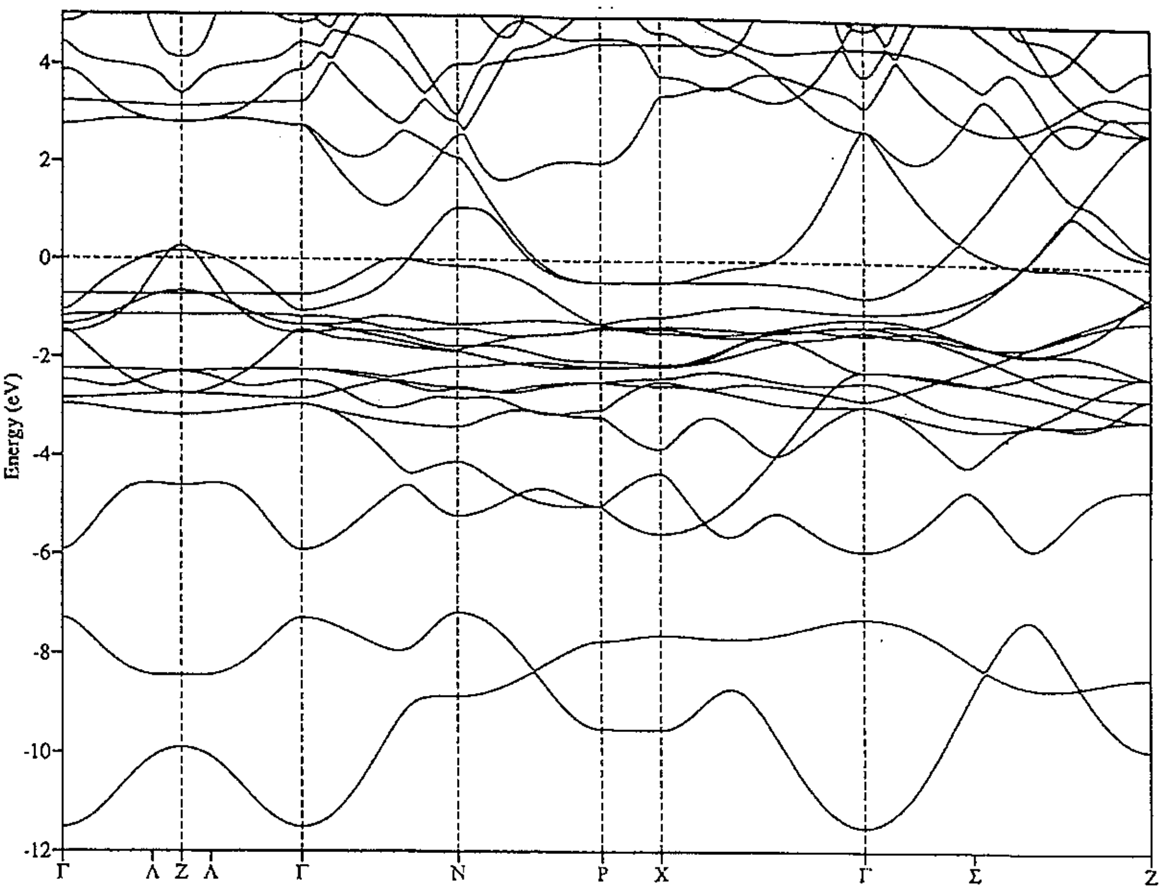

FIG. 4.34 Band structure of $GdNi_2Ge_2$ shown along selected high symmetry lines (see inset in Fig. 23 for details). The band structure is the result of a tight-binding linear-muffin-tin-orbital calculation using the atomic-sphere approximation after [85].

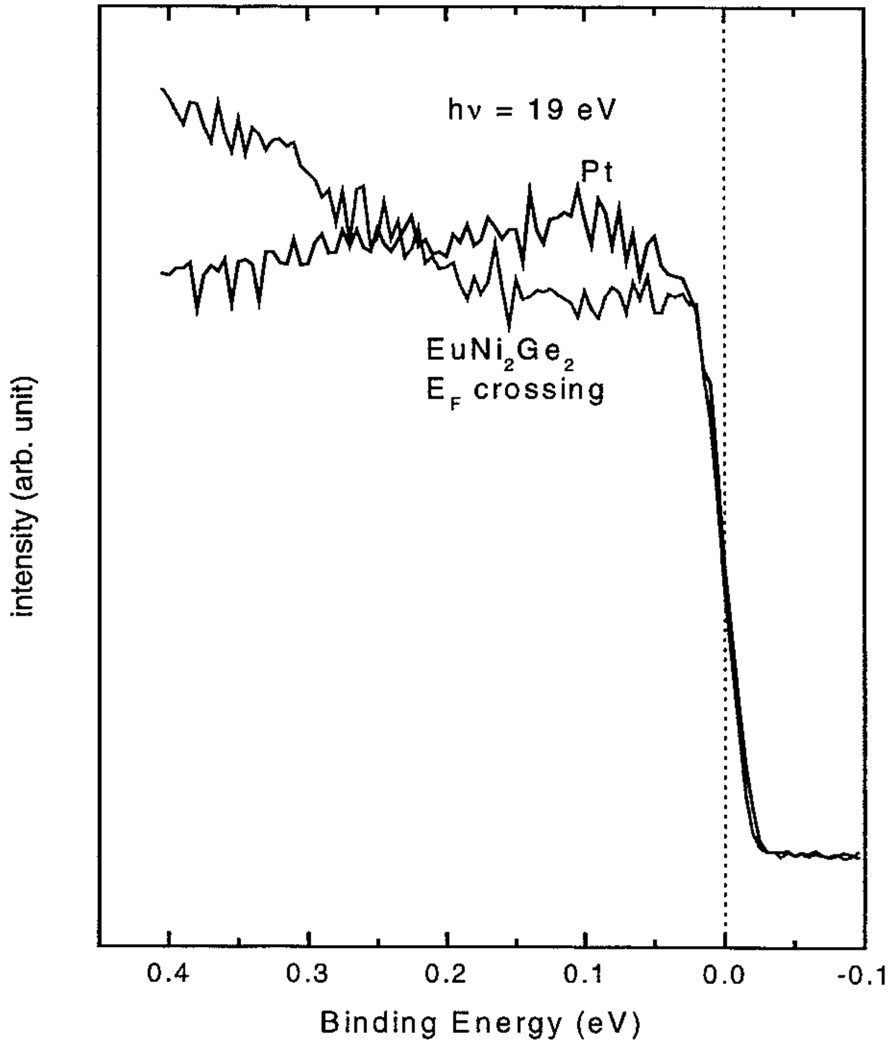

FIG. 4.35 A high-energy resolution (ΔE = 38 meV) ARPES spectrum of EuNi$_2$Ge$_2$ measured at 20 K at a photon energy of 19 eV and angle of 24° which shows a E_F crossing compared with a Pt foil spectrum.

The appearance of the new energy gaps, which are a result of the magnetic periodicity, is similar to that of the zone-boundary gaps due to the lattice periodicity. We now describe an attempt to find evidence of the SDW. We expect evidence to present itself in the form of a decrease of intensity at the Fermi edge when the crystal temperature passes below $T_N = 30.8$ K and transitions from paramagnetic to AF. This would be the effect of the band splitting described due to the SDW. But note that the leading edge of the spectrum of $EuNi_2Ge_2$ already lined up with Pt foil at this temperature. Thus, we were unable to find any experimental evidence of a SDW. One reason for this could be that the gap is too subtle to pick up with our present resolution, since mean-field theory predicts a very small gap of 9.4 meV ($\Delta = 3.53kT_N$) with T_N of 30.8 K. Another one may be that there is no SDW gap at this specific k point in this material. If this is one point on the nesting part of the FS, a gap is expected but if it's elsewhere on the FS, no gap is expected. The SDW for $GdNi_2Ge_2$ was also not observed in Ref [111]. One future experiment is to repeat the measurement on a higher resolution beamline for evidence of a SDW in $EuNi_2Ge_2$ and $GdNi_2Ge_2$. Another is ARPES on $Gd_xEu_{1-x}Ni_2Ge_2$ pseudoternary alloys to study gradual band-filling effects in detail. Changing the stoichiometry of these pseudoternary alloys would permit observation of changes in the Fermi surfaces and the evolution of the electronic band structure, as it were, with increasing Gd concentration.

CHAPTER 5. CONCLUSIONS

The electronic structures of $EuNi_2Ge_2$ and $GdNi_2Ge_2$ have been investigated using photoemission spectroscopy. The majority of the photoemission intensity near E_F was due to the mostly Ni 3*d* states in both materials. CIS spectra were recorded at selected initial-state binding energies across the excitation energy range of the Ni 3*p* threshold in $EuNi_2Ge_2$. It is apparent that there is strong Ni *d* character throughout the valence band from CIS spectra. Resonance measurements of the Eu $4d \rightarrow 4f$ excitations in $EuNi_2Ge_2$ reveal that Eu 4*f* states are localized around 2 eV below E_F. When crossing the Eu $4d \rightarrow 4f$ core-absorption threshold, resonance of the Eu 5*p* and Eu 5*s* states was also seen. It is observed that Gd 4*f* peak in $GdNi_2Ge_2$ is more tightly bound by 6.4 eV than the Eu 4*f* peak in $EuNi_2Ge_2$.

We have seen a resonant enhancement of the Ni 3*d* satellite at about 7.4 eV BE, indicating Ni 3*d* character around E_F in $EuNi_2Ge_2$. The Ni 3*d* partial spectral weights (PSW) from the Ni $3p \rightarrow 3d$ RPES measurements show that they are very close to the calculated Ni 3*d* density of states for both materials. We have measured Constant-Final-State (CFS) and Constant-Initial-State (CIS) spectra in an attempt to check the valence of Eu ion in $EuNi_2Ge_2$ and it is verified as 2+. The measured CFS spectra of $GdNi_2Ge_2$ was almost same as those of $EuNi_2Ge_2$ and Gd metal, indicating that Gd ions in $GdNi_2Ge_2$ are trivalent with the same $4f^7$ configuration as the Eu ion in $EuNi_2Ge_2$.

We presented the experimental energy bands mapped from the normal-emission spectra of $EuNi_2Ge_2$ and $GdNi_2Ge_2$ (001) surfaces using synchrotron radiation with increasing photon energies from 14 eV to 54 eV. In the case of $GdNi_2Ge_2$, the photon energy range used is from 14 eV to 44 eV. We found good symmetry in the normal direction [001] making it possible to compare complete band structures. Four and three major photoemission features disperse along the normal [001] Brillouin zone (BZ) direction in $EuNi_2Ge_2$ and $GdNi_2Ge_2$ respectively, in good agreement with the band calculations. The dispersions seen lead to a determination of the inner potentials V_0 to be 11.0 eV ± 0.2 eV for $EuNi_2Ge_2$ and 11.5 eV ± 0.2 eV for $GdNi_2Ge_2$ by adjusting Γ and Z symmetry points with the experimental photoemission in the normal direction. Our results for $GdNi_2Ge_2$ show that all of the observed band features are shifted downward by 0.2 eV-0.3 eV compared to those of $EuNi_2Ge_2$. The E_F shift simply corresponds to an increase of one electron (1e/formula unit) in $GdNi_2Ge_2$ upon going from $EuNi_2Ge_2$ to $GdNi_2Ge_2$.

We have studied ARPES with high energy resolution to investigate the band structures of single-crystal $EuNi_2Ge_2$ and $GdNi_2Ge_2$ samples and compare the experimental results to the theoretical ones of the band structure calculations. The dispersion of photoemission peaks in the valence band was found in the ΓXPZ plane of the BZ. The inner potential of 11.0 eV for $EuNi_2Ge_2$ was also crosschecked when the symmetric behavior of the dispersion around symmetric lines were studied. The Fermi surfaces (FSs) were mapped by ARPES in the ΓXPZ planes of the BZs for both materials. They were in good agreement with those from band structure calculations. No evidence of a SDW was found for $EuNi_2Ge_2$. It could be that the gap is too subtle to pick up with our present resolution, or there may be no SDW in this sample. Future experiments on higher resolution beamlines may be enlightening for the evidence of a SDW in $EuNi_2Ge_2$ and $GdNi_2Ge_2$.

$EuNi_2Ge_2$ is isostructural to $GdNi_2Ge_2$, but its conduction band has one less electron. Compared to the FS of $EuNi_2Ge_2$ in the ΓXPZ plane of the BZ, $GdNi_2Ge_2$ has a more bulging shape around the Γ point, indicating that the FS is located at a higher energy than that of $EuNi_2Ge_2$. That is due to the fact that the Gd ion in $GdNi_2Ge_2$ has a valence of 3+ with one more conduction electron than the Eu ion in $EuNi_2Ge_2$, confirming the effects of band filling on electric and magnetic structures. Vice versa, it can also be said that the FS will shrink toward the X point in the ΓXPZ planes when electrons are removed from $GdNi_2Ge_2$. Therefore those compounds which give the same Hund's rule ground state ($^8S_{7/2}$) were an ideal system for the study of effects of band filling on electric and magnetic structures. Future experiments with changing the stoichiometry of $Gd_xEu_{1-x}Ni_2Ge_2$ pseudoternary alloys would permit observation of gradual changes in the FSs, and the E_F may shift to higher energies with increasing Gd concentration.

REFERENCES

[1] H. Pinto, M. Melamud, M. Kuznietz, and H. Shaked: Phys. Rev. B **31**, 508 (1985).

[2] A. Szytuła and J. Leciejewicz, in: K. A. Gschneidner, Jr. and L. Eyring, ed.: *Handbook on the Physics and Chemistry of Rare Earths* (North-Holland, Amsterdam, 1989), Vol. 12, Chap. 83.

[3] A. Szytuła and J. Leciejewicz, *Handbook of Crystal Structures and Magnetic Properties of Rare Earth Intermetallics* (CRC Press, Boca Raton, 1994), pp. 114-192.

[4] S. L. Bud'ko, Z. Islam, T. A. Wiener, I. R. Fisher, A. H. Lacerda, and P. C. Canfield: J. Magn. Magn. Mater. **205**, 53 (1999).

[5] R. J. Elliott, in: G. T. Rado and H. Suhl, ed.: *Magnetism* (Academic Press, New York, 1965), Vol. IIA, Chap. 7.

[6] S. H. Liu, in: K. A. Gschneidner, Jr. and L. Eyring, ed.: *Handbook on the Physics and Chemistry of Rare Earths* (North-Holland, Amsterdam, 1978), Vol. 1: Metals, Chap. 3.

[7] G. Wortmann, I. Nowik, B. Perscheid, G. Kaindl, and I. Felner: Phys. Rev. B **43**, 5261 (1991).

[8] H.-J. Hesse, R. Lübbers, M. Winzenick, H. W. Neuling, and G. Wortmann: J. Alloys and Compounds **246**, 220 (1997).

[9] H. Wada, M. F. Hundley, R. Movshovich, and J. D. Thompson: Phys. Rev. B **59**, 1141 (1999).

[10] I. Felner and I. Nowik: J. Phys. Chem. Solids. **39**, 767 (1978).

[11] Z. Islam, C. Detlefs, C. Song, A. I. Goldman, V. Antropov, B. N. Harmon, S. L. Bud'ko,

T. Wiener, P. C. Canfield, D. Wermeille, and K. D. Finkelstein: Phys. Rev Lett. **83**, 2817 (1999).

[12] O. K. Andersen: Phys. Rev. B **12**, 3060 (1975).

[13] O. K. Andersen, O. Jepsen, and D. Glötzel, in: F. Bassani, F. Fumi, and M. P. Tosi, ed.: *Highlights of Condensed-MatterTheory* (North-Holland, Amsterdam, 1985), pp. 59-176.

[14] H. L. Skriver: *The LMTO Method: Muffin-Tin Orbitals and Electronic Structure* (Springer-Verlag, Berlin, 1984).

[15] U. V. Barth and L. Hedin: J. Phys. C : Solid State **5**, 1629 (1972).

[16] G. Grüner: *Density Waves in Solids* (Addison Wesley, New York, 1994).

[17] A. Einstein: Ann. Physik **17**, 132 (1905).

[18] T. Koopmans, Physica **1**, 104 (1934).

[19] T. A. Carlson: *Photoelectron and Auger Spectroscopy* (Plenum Press, New York, 1978), pp. 68-87.

[20] C. N. Berglund and W. E. Spicer: Phys. Rev. A **136**, 1030 and 1044 (1964).

[21] S. Hüfner: *Photoelectron Spectroscopy* (Springer, New York, 1996).

[22] D. W. Lynch and C. G. Olson: *Photoemission Studies of High-Temperature Superconductors* (Cambridge University Press, Cambridge, 1999).

[23] E. W. Plummer and W. Eberhardt: Adv. Chem. Phys. **49**, 533 (1982).

[24] W. E. Spicer, in: B. O. Seraphin, ed: *Optical Properties of Solids: New Developments* (North-Holland, New York, 1976) pp. 633-639.

[25] M. P. Seah and W. A. Dench: Surf. Interface Anal. **1**, 2 (1979).

[26] M. Cardona and L. Ley, in: M. Cardona and L. Ley, ed.: *Photoemission in Solids I*

(Springer-Verlag, Berlin, 1978), pp. 84-85.

[27] G. J. Lapeyre, J. Anderson, P. L. Gobby, and J. A. Knapp: Phys. Rev. Lett **33**, 1290 (1974).

[28] D. W. Lynch and C. G. Olson: *Photoemission Studies of High-Temperature Superconductors* (Cambridge University Press, New York, 1999), pp. 64-66.

[29] G. W. Gobeli, F. G. Allen, and E. O. Kane: Phys. Rev. Lett. **12**, 94 (1964).

[30] E. O. Kane: Phys. Rev. Lett. **12**, 97 (1964).

[31] U. Gerhardt and E. Dietz: Phys. Rev. Lett. **26**, 1477 (1971).

[32] W. Eberhardt and E. W. Plummer: Phys. Rev. B **21**, 3245 (1980).

[33] G. D. Mahan: Phys. Rev. Lett. **24**, 1068 (1970).

[34] J. Stöhr, P. S. Wehner, R. S. Williams, G. Apai, and D. A. Shirley: Phys. Rev. B **17**, 587 (1978).

[35] F. J. Himpsel: Adv. Phys. **32**, 1 (1983).

[36] D. Ehm, F. Reinert, G. Nicolay, S. Schmidt, S. Hüfner, R. Claessen, V. Eyert, C. Geibel: Phys. Rev. B **64**, 235104 (2001).

[37] H. J. Levinson, G. Greuter, and E. W. Plummer: Phys. Rev. B **27**, 727 (1983).

[38] S. Hüfner: *Photoelectron Spectroscopy* (Springer, New York, 1996), pp. 348-351.

[39] V. L. Moruzzi, J. F. Janak, and A. R. Williams: *Calculated Electronic Properties of Metals* (Pergamon Press Inc., New York, 1978).

[40] L. Ley and M. Cardona, ed.: *Photoemission in Solids I and II* (Springer-Verlag, Berlin, 1978).

[41] J. W. Allen, in: R. Z. Bachrach, ed.: *Synchrotron Radiation Research: Advances in*

Surface and Interface Science (Plenum Press, New York, 1992), Vol. 1: Techniques, Chap. 6.

[42] U. Fano: Phys. Rev. **124**, 1866 (1961).

[43] C. Kunz, in: B. Feuerbacher, B. Fitton, and R. F. Willis, ed.: *Photoemission and the Electronic Properties of Surfaces* (John Wiley & Sons, Chichester, 1978) Chap. 17.

[44] C. Kunz, ed.: *Synchrotron Radiation: Techniques and Applications* (Springer-Verlag, Berlin, 1979), Chap. 1-Chap. 3.

[45] H. Winick and S. Doniach, ed.: *Synchrotron Radiation Research* (Plenum Press, New York, 1980), Chap. 1-Chap. 3.

[46] E.-E. Koch, ed.: *Handbook on Synchrotron Radiation* (North-Holland Publishing Company, Amsterdam, 1983), Vol. 1A, Chap. 1-4.

[47] G. Margaritondo: *Introduction to Synchrotron Radiation* (Oxford, New York, 1988), Chap. 2.

[48] R. Z. Bachrach, ed.: *Synchrotron Radiation Research: Advances in Surface and Interface Science* (Plenum Press, New York, 1992), Vol. 2: Issues and Technology, Chap. 8-Chap. 9.

[49] D. W. Lynch and C. G. Olson: *Photoemission Studies of High-Temperature Superconductors* (Cambridge University Press, Cambridge, 1999), Chap. 4.

[50] C. G. Olson: Nucl. Instrum. Methods A **266**, 205 (1988).

[51] VSW HA50 Hemispherical Analyzer Instruction Manual (VSW Scientific Instruments Ltd., Manchester, England, 1989).

[52] D. W. Lynch and C. G. Olson: *Photoemission Studies of High-Temperature*

Superconductors (Cambridge University Press, Cambridge, 1999), page 138.

[53] R. Liu: Ph.D. thesis, Iowa State University (1990), pp. 22-24.

[54] W. Rieger and E. Parthé: Monatshefte für Chemie **100**, 444 (1969).

[55] P. C. Canfield and Z. Fisk: Phil. Mag. B **56**, 1117 (1992).

[56] J. J. Yeh and I. Lindau: At. Data. Nucl. Data Tables **32**, 1 (1985).

[57] C. Guillot, Y. Ballu, J. Paigné, J. Lecante, K. P. Jain, P. Thiry, R. Pinchaux, Y. Pétroff, and L. M. Falicov: Phys. Rev. Lett. **39**, 1632 (1977).

[58] S. Hüfner and G. K. Wertheim: Phys. Lett. **51A**, 299 (1975).

[59] S. Hüfner: *Photoelectron Spectroscopy* (Springer, New York, 1996), pp. 90-96.

[60] A. Kotani and Y. Toyozawa: J. Phys. Soc. Jpn. **35**, 1073 and 1082 (1973).

[61] A. Kotani and Y. Toyozawa: J. Phys. Soc. Jpn. **37**, 912 (1974).

[62] D. R. Penn: Phys. Rev. Lett. **42**, 921 (1979).

[63] D. W. Lynch and C. G. Olson: *Photoemission Studies of High-Temperature Superconductors* (Cambridge University Press, Cambridge, 1999), pp. 182-184.

[64] M. Campagna and R. Rosei, ed.: *Photoemission and Absorption Spectroscopy of Solids and Interfaces with Synchrotron Radiation* (North-Holland, Amsterdam, 1990), page 13.

[65] M. J. Freiser, S. Methfessel, and F. Holtzberg: J. Appl. Phys. **39,** 900 (1968).

[66] B. Feuerbacher, B. Fitton, and R. F. Willis, ed.: *Photoemission and Electronic Properties of Surfaces* (John Wiley & Sons, Chichester, 1978), page 442.

[67] F. Gerken, J. Barth, and C. Kunz, in: B. Crasemann, ed.: *Proceedings of the International Conference on X-Ray and Atomic Inner-shell Physics* (AIP, New York, 1982), pp. 602-614.

[68] P. O. Hedén, H. Löfgren, and S. B. M. Hagström: Phys. Stat. Sol. B **49**, 721 (1972).

[69] L. Ley and M. Cardona, ed: *Photoemission in Solids II* (Springer-Verlag, Berlin, 1979), pp. 217-260.

[70] J. F. Herbst and J. W. Wilkins: Phys. Rev. Lett. **43**, 1760 (1979).

[71] S. B. M. Hagström in: D. J. Fabian and L. M. Watson ed.: *Band Structure Spectroscopy of Metals and Alloys* (Academic Press, London, 1973), pp. 73-89.

[72] M. Richter, M. Meyer, M. Pahler, T. Prescher, E. v. Raven, B. Sonntag, and H.-E. Wetzel: Phys. Rev. A **40**, 7007 (1989).

[73] U. Becker, H. G. Kerkhoff, D. W. Lindle, P. H. Kobrin, T. A. Ferrett, P. A. Heimann, C. M. Truesdale, and D. A. Shirley: Phys. Rev. A **34**, 2858 (1986).

[74] E.-J. Cho, S.-J. Oh, S. Suga, T. Suzuki, and T. Kasuya: J. Electron Spect. and Related Phen. **77**, 173 (1996).

[75] R. Z. Bachrach, ed.: *Synchrotron Radiation Research: Advances in Surface and Interface Science* (Plenum Press, New York, 1992),Vol. 1: Techniques, page 275.

[76] S. Liu, in: K. A. Gschneidner, Jr. and L. Eyring, ed.: *Handbook on the Physics and Chemistry of Rare Earths* (North-Holland Publishing Company, Amsterdam, 1978), Vol. 1: Metals, page 296.

[77] W. J. Lademan, A. K. See, L. E. Klebanoff, and Gerrit van der Laan: Phys. Rev. B **54**, 17191 (1996).

[78] S. Doniach and M. Sunjic: J. Phys. C **3**, 285 (1970).

[79] F. Gerken, A. S. Flodström, J. Barth, L. I. Johansson, and C. Kunz: Physica Scripta **32**, 43 (1985).

[80] P. H. Citrin, G. K Wertheim, and Y. Baer: Phys. Rev. Lett. **41**, 1425 (1978).

[81] M. Aldén, H. L. Skriver , I. A. Abrikosov and B. Johansson: Phys. Rev. B **51**, 1981 (1995).

[82] R. Kammerer, J. Barth, F. Gerken, A. Flodström, and L. I. Johansson: Solid State Commun. **41**, 435 (1982).

[83] C. Laubschat, G. Kaindl, W.–D. Schneider, B. Reihl, and N. Martensson: Phys. Rev. B **33**, 6675 (1986).

[84] A. J. Freeman, in: R. J. Elliott, ed.: *Magnetic Properties of Rare Earth Metals* (Plenum Press, London, 1972), Chap. 6.

[85] Z. Islam: Ph.D. thesis, Iowa State University (1999).

[86] S. Haffner, C. G. Olson, and D. W. Lynch: Phys. Rev. B **60**, 16346 (1999).

[87] W. Gudat and C. Kunz: Phys. Rev. Lett. **29**, 169 (1972).

[88] D. Wieliczka, J. H. Weaver, D. W. Lynch, and C. G. Olson: Phys. Rev. B **26**, 7056 (1982).

[89] C. G. Olson and D.W. Lynch: J. Opt. Soc. Am. **72**, 88 (1982).

[90] L. Ley and M. Cardona, ed.: *Photoemission in Solids II* (Springer-Verlag, Berlin, 1978) page 226.

[91] J. Rohler: J. Magn. Magn. Mater. **47-48**, 175 (1985).

[92] J. L. Dehmer, A. F. Starace, U. Fano, J. Sugar, and J. W. Cooper: Phys. Rev. Lett. **26**, 1521 (1971).

[93] J. L. Dehmer and A. F. Starace: Phys. Rev. B **5**, 1792 (1972).

[94] H. Ogasawara, A. Kotani, K. Okada, and B. T. Thole: Phys. Rev. B **43**, 854 (1991).

[95] G. Kalkowski, C. Laubschat, W. D. Brewer, E. V. Sampathkumaran, M. Domke, G. Kaindl: Phys. Rev. B **32**, 2717 (1985).

[96] D. W. Lynch and R. D. Cowan: Phys. Rev. B **36**, 9228 (1987).

[97] A. Zangwill: J. Phys. C: Solid State Phys. **20**, L627 (1987).

[98] V. A. Fomichev, T. M. Zimkina, S. A. Gribovskii, and I. I. Zhukova: Soviet Phys.: Solid State **9**, 1163 (1967).

[99] O.-P. Sairanen and S. Aksela: J. Phys.: Condens. Matter **4,** 3337 (1992).

[100] J. Sugar: Phys. Rev. B **5**, 1785 (1972).

[101] I. Nowik, I. Felner, and E. R. Bauminger: Phys. Rev. B **55**, 3033 (1997).

[102] E.-J. Cho and S.-J. Oh: Phys. Rev. B **59**, 15613 (1999).

[103] W. D. Schneider, C. Laubschat, G. Kalkowski, J. Haase, and A. Puschmann: Phys. Rev. B **28**, 2017 (1983).

[104] A. Szytuła and J. Leciejewicz: *Handbook of Crystal Structure and Magnetic Properties of Rare Earth Intermetallics* (CRC Press, Boca Raton, 1994), pp. 151-154.

[105] E. R. Bauminger, D. Froindlich, I. Nowik, S. Ofer, I. Felner, and I. Mayer: Phys. Rev. Lett. **30**, 1053 (1973).

[106] L. I. Johansson and C. G. Larsson, in: S. D. Kevan, ed.: *Angle-resolved Photoemission* (Elsevier, Amsterdam, 1992), Chap. 6.

[107] N. F. Mott: Phil. Mag. **22**, 287 (1936).

[108] W. E. Spicer, in: D. J. Fabian and L. M. Watson, ed.: *Band Structure Spectroscopy of Metals and Alloys* (Academic Press, London, 1973), pp. 7-53.

[109] S. Hüfner, in: L. Ley and M. Cardona, ed.: *Photoemission in Solid II* (Springer-Verlag,

Berlin, 1979), pp 206-216.

[110] R. Liu, B. W. Veal, A. P. Paulikas, J. W. Downey, P. J. Kostic, S. Fleshler, U. Welp, C. G. Olson, X. Wu, A. J. Arko, and J. J. Joyce: Phys. Rev. B **46**, 11056 (1992).

[111] D. Brammeier: Ph.D. thesis, Iowa State University (2001).

[112] L. Kipp, K. Roßnagel, C. Solterbeck, T. Strasser, W. Schattke, and M. Skibowski, Phys. Rev. Lett. **83**, 5551 (1999) and references therein.

[113] A. W. Overhauser, Phys. Rev. **128**, 1437 (1962).

[114] W. M. Lomer, Proc. Phys. Soc. London **80**, 489 (1962).

ACKNOWLEDGEMENTS

I sincerely wish to thank my major Professor David. W. Lynch, for his invaluable guidance, advice, and support on this work throughout the years of my graduate study at Iowa State University. I am so grateful to Dr. Clifford G. Olson for the generous assistance and for many helpful discussions and answers, especially for experimental aspects of this work during my research at Synchrotron Radiation Center, WI. I'd admit that they take important part in my life.

I also would like to thank Dr. Paul Canfield for the preparation of the $EuNi_2Ge_2$ and $GdNi_2Ge_2$ crystals. I am grateful to Dr. Zahirul Islam for helpful discussions, and Jong-Woo Kim for taking Laue pattern of the crystals. I wish to thank my co-major Professor Joseph Shinar, and POS committee-member Professors, David C. Johnston, R. William McCallum, and John G. Lajoie for reviewing the thesis.

I would like to thank my wife, Kyunghwa Kim for her constant support, encouragement, and love.

I want to thank my children, Heeyoung Park and Hannah Park for my precious treasure.

Special thanks go to the truly living God, Jesus Christ for his unconditional grace and infinite love for us, and for giving me strength and courage whenever they are needed.

This work was performed at Ames Laboratory under Contract No. W-7405-Eng-82 with the U.S. Department of Energy. The United States government has assigned the DOE Report number IS-T 1936 to this thesis.